In presenting the dissertation as a partial fulfillment of the requirements for an advanced degree from the Georgia Institute of Technology, I agree that the Library of the Institute shall make it available for inspection and circulation in accordance with its regulations governing materials of this type. I agree that permission to copy from, or to publish from, this dissertation may be granted by the professor under whose direction it was written, or, in his absence, by the Dean of the Graduate Division when such copying or publication is solely for scholarly purposes and does not involve potential financial gain. It is understood that any copying from, or publication of, this dissertation which involves potential financial gain will not be allowed without written permission.

7/25/68

TWO-PHASE COMBUSTION

A THESIS

Presented to

The Faculty of the Graduate Division

by

Mack Donald Bowen

In Partial Fulfillment

of the Requirements for the Degree

Doctor of Philosophy

In the School of Mechanical Engineering

Georgia Institute of Technology

April, 1970

TWO-PHASE COMBUSTION

Approved:

Chairman

Date approved by Chairman: 5/25/70

ACKNOWLEDGMENTS

The author is grateful to the many people who have encouraged and assisted him in this endeavor, especially to his wife, Betty, for her patience, understanding and support and to his children, Susan, Kelby and Mark, who have helped in so many different ways.

Sincere appreciation is expressed to Dr. Charles W. Gorton, the author's thesis advisor, for his guidance and encouragement throughout the entire work. Appreciation is also extended to Dr. Henderson C. Ward and Dr. Walter O. Carlson for their helpful comments in reviewing the work. A special note of thanks is due the Nuclear Research Center personnel for their help in conducting the neutron activation analyses.

The support and assistance of the Research Center, Lockheed-Georgia Company is gratefully acknowledged.

TABLE OF CONTENTS

Experimental Apparatus
   Experimental Chamber
Instrumentation
   Thermocouple Probe
   Pulsed Thermocouple Probe
   Powder Feeder
   Hydrogen Flowmeter
   Water Cooled Probe
   Chromatography and Neutron Activation
     Analysis Equipment

Jet Mixing
Pre-Ignition Particle Heating
Aluminum Particle Combustion

Velocity Measurements
Temperature Measurements
Chemical Species Measurements
Particle Distribution Measurements

TABLE OF CONTENTS (Continued)

LIST OF TABLES

LIST OF ILLUSTRATIONS

LIST OF ILLUSTRATIONS (Continued)

LIST OF ILLUSTRATIONS (Continued)

LIST OF ILLUSTRATIONS (Continued)

SUMMARY

The primary objective of this work was to investigate experi-
mentally and theoretically the problem of the turbulent mixing of
chemically reacting jets and the combustion of entrained solid par-
ticles. The theoretical work represents an extension of Libby's
theoretical treatment of the problem. A free parameter, n, was used
as an exponent of the stream function which resulted in families of
solutions. The solutions obtained were profiles which were stretched
or compressed depending on the value of the free parameter, n, selected.

Experimental data were obtained on temperature, velocity, and
chemical species with concentric jets of hydrogen and air. Concentra-
tion data were used to obtain a theoretical solution which corresponded
to Libby's theory. Based on this solution comparisons of theoretical
and experimental temperature, concentration, and velocity profiles were
made. Chemical equilibrium throughout the flow was assumed in the
theoretical analysis.

A novel gas temperature measurement technique which apparently
has not been used before was developed in this investigation. The tech-
nique was used to measure the maximum temperature in the hydrogen-air
flame and the results compared with measurements obtained with a pulsed
thermocouple. For the case of a laminar boundary layer on the probe the
technique permits gas temperatures to be determined in a manner such
that the measurements are independent of the probe's emissivity and
Reynolds number, and gas mixture properties so long as they do not change

around the probe tip.

A general combustion model for the burning of a single aluminum particle was presented. The model was based on an assumption concerning the mechanism by which Al_2O_3 is formed in the combustion process. Using this model the complete flame structure of a burning aluminum particle was calculated assuming chemical equilibrium in the region surrounding the droplet. A criterion for the location of the region in which Al_2O_3 forms was developed.

Experimental studies were conducted on the distribution of aluminum particles entrained in the hydrogen jet. Visual observations, high speed photography and particle sampling were used to study the flame with burning particles. A technique using neutron activation analysis was developed in this study for measuring the particle mass flux distribution and the particle density distributions in the flame. The technique avoids the difficulties associated with burned or partially burned particles. Experimental data was obtained on particle mass flux distributions, particle flux distributions and particle density distributions in the flow.

NOMENCLATURE

Symbol

<u>English Letters</u>

A	surface area, ft^2
C_i	mass fraction of species i
$\bar{C}_i$	element mass fraction of element i
C_p	specific heat, Btu/lbm-°R
d	probe tip diameter, ft
D_{ij}	binary diffusion coefficient, ft^2/sec
F	radiation shape factor
ΔF	free energy function, Btu/lbm
ΔF_f^o	free energy of formation at reference state, Btu/lbm
h	chemical enthalpy of gas mixture, Btu/lbm
h_i	chemical enthalpy of species i, Btu/lbm
$\bar{h}$	average heat transfer coefficient for a sphere, Btu/ft^2-sec-°R
$\bar{H}$	nondimensional enthalpy
k	thermal conductivity of gas mixture, Btu/ft-sec-°R
K_p	equilibrium constant
Le	Lewis number
m_i	mass of species i, lbm
$\overset{o}{m}$	mass flux, lbm/ft^2-sec
m_i	particle mass flux impinging on i^{th} segment of collector strip, lbm/ft^2-sec
M_{Al_i}	aluminum mass per unit area on the ith segment of the collector strip, lbm/ft^2
M_{T_i}	particle mass flux at $r = r_i$ through an area of $\pi(r_i^2 - r_{i-1}^2)$, lbm/sec

English Letters

M_T	total particle mass flux, $lbm/ft^2\text{-sec}$
M	molecular weight
n_s	mass flux at the particle surface, $lbm/ft^2\text{-sec}$
n	free parameter exponent of the stream function
$\vec{n}_i$	mass flux of species i, $lbm/ft^2\text{-sec}$
$\vec{n}$	bulk flow, $lbm/ft^2\text{-sec}$
n_{i_r}	mass flow of species i in the r direction, $lbm/ft^2\text{-sec}$
n_i	moles of species i
n_r	mass flux in the radial direction, $lbm/ft^2\text{-sec}$
N_{T_i}	particle flux at $r = r_i$ through an area $\pi(r_i^2 - r_{i-1}^2)$, particles/sec
N_T	total particle flux, particles/sec
Nu	Nusselt number
Pr	Prandtl number
P_i	absolute partial pressure of species i, lbf/ft^2
ΔP	dynamic pressure, inches of H_2O
q_s	energy conducted into particle, $Btu/ft^2\text{-sec}$
q	radiation heat flux, $Btu/ft^2\text{-sec}$
r	radial position coordinate, ft
r_s	particle radius, ft
$r_{i,k}$	mass ratio of element i in species k
r_o	radius of hydrogen jet, ft
Re	Reynolds number
R	gas constant, $Btu/lbm\text{-}^oR$
Sc	Schmidt number

English Letters

t	time, sec
T	temperature, $^\circ R$
u	gas velocity in axial direction, ft/sec
$\bar{U}$	nondimensional velocity
v	velocity in radial direction, ft/sec
x	distance along surface from the stagnation point on a sphere, ft
z	axial position coordinate, ft

Greek Letters

$\bar{\alpha}$	radiation parameter defined by equation (3-13), page
$\bar{\beta}$	nondimensional parameter defined by equation (4-7), page
α	average particle mass, lbm
$\bar{\epsilon}$	eddy transport property
η	ratio of the local heat transfer coefficients at two positions on a sphere
θ	angle at the center of a sphere between a line drawn to the stagnation point and a line drawn to any other point on the sphere, radians
μ	viscosity of gas mixture, lbm/ft-sec
ρ	density of gas mixture, lbm/ft^3
ρ_i	density of aluminum in the flow, lbm/ft^3
σ	Stephen-Boltzman constant, Btu/ft^2-sec-$^\circ R^4$
ψ	stream function defined by equation (4-8), page 37
ζ	transformation variable defined by equation (4-17), page 40
$\dot{\omega}_i$	rate of production of species i, lbm/ft^3-sec

Subscripts   Unless defined otherwise the subscripts used have
              the meanings as indicated below

e   air jet free stream

g   gas

i   refers to species i

j   refers to hydrogen jet

k   refers to element k

o   refers to stagnation point

s   refers to particle surface

t   refers to the turbulent properties

w   refers to the wall

∞ refers to conditions in the free stream

CHAPTER I

INTRODUCTION

The interest in metal combustion in recent years has been due primarily to rocket propellant studies which indicated higher performance fuels could be obtained with metal additives. These fuels ranged from metal slurries for air breathing or rocket engines to solid propellants with large quantities of metal additives.

One of the latest vehicle innovations is the air augmented rocket in which a propellant with metal additives burns in a fuel rich condition. The exhaust from the rocket is further burned with an air-stream in a shroud at the rear of the rocket. In this manner a signifi-cant increase in impulse may be obtained. The burning of a fuel slurry with metal additives in a high velocity ramjet is another typical appli-cation which involves metal combustion along with another fuel.

Many of the systems which use propellants of this type are in the experimental stage of development. The work reported here is rela-ted to the general class of problems associated with these devices. The study, however, was directed toward a more basic problem and con-sequently, is not directly related to a particular device.

The combustion problem considered here involves a gaseous, or liquid, fuel with entrained solid combustibles mixing and burning in an air stream. Generally, this problem may be discussed in two parts, turbulent mixing and metal combustion.

A large volume of literature is available on turbulent mixing, particularly for incompressible flows. For the compressible, chemically

reacting case, however, only a limited amount of data are available. Much of the previous work concerned the turbulent mixing of non-reacting, dissimilar gases with the intent of applying the results to the chemically reacting flows. Due to the difficulties in performing measurements in flows of this type very few experiments have been performed in which direct measurements of concentrations, temperatures, and velocities were made.

For these reasons a considerable part of the present investigation was directed at obtaining data on the compressible, turbulent mixing of chemically reacting streams. These efforts involved a theoretical treatment of the problem which was primarily directed at obtaining a simplified mathematical technique useful in correlating the experimental data. The bulk of the work on this problem, however, was experimental. For this study a small hydrogen jet located at the center of a large air jet was selected.

The concentric jet geometry was also used with metal particles entrained in the hydrogen flow. Small aluminum particles which have shown great promise as a fuel additive were chosen as a suitable solid combustible for this investigation. High speed pictures of the jet burning with aluminum powder showed that the particles did not ignite until they crossed the reaction envelope. Later, measurements on concentrations further showed that the particles burn essentially in an air environment except for those which remain in the center of the flow and cross the reaction envelope at the flame tip region. Figure 1, page 3, shows the flame with metal particles igniting and burning beyond the reaction envelope. For these reasons the particle combustion study was
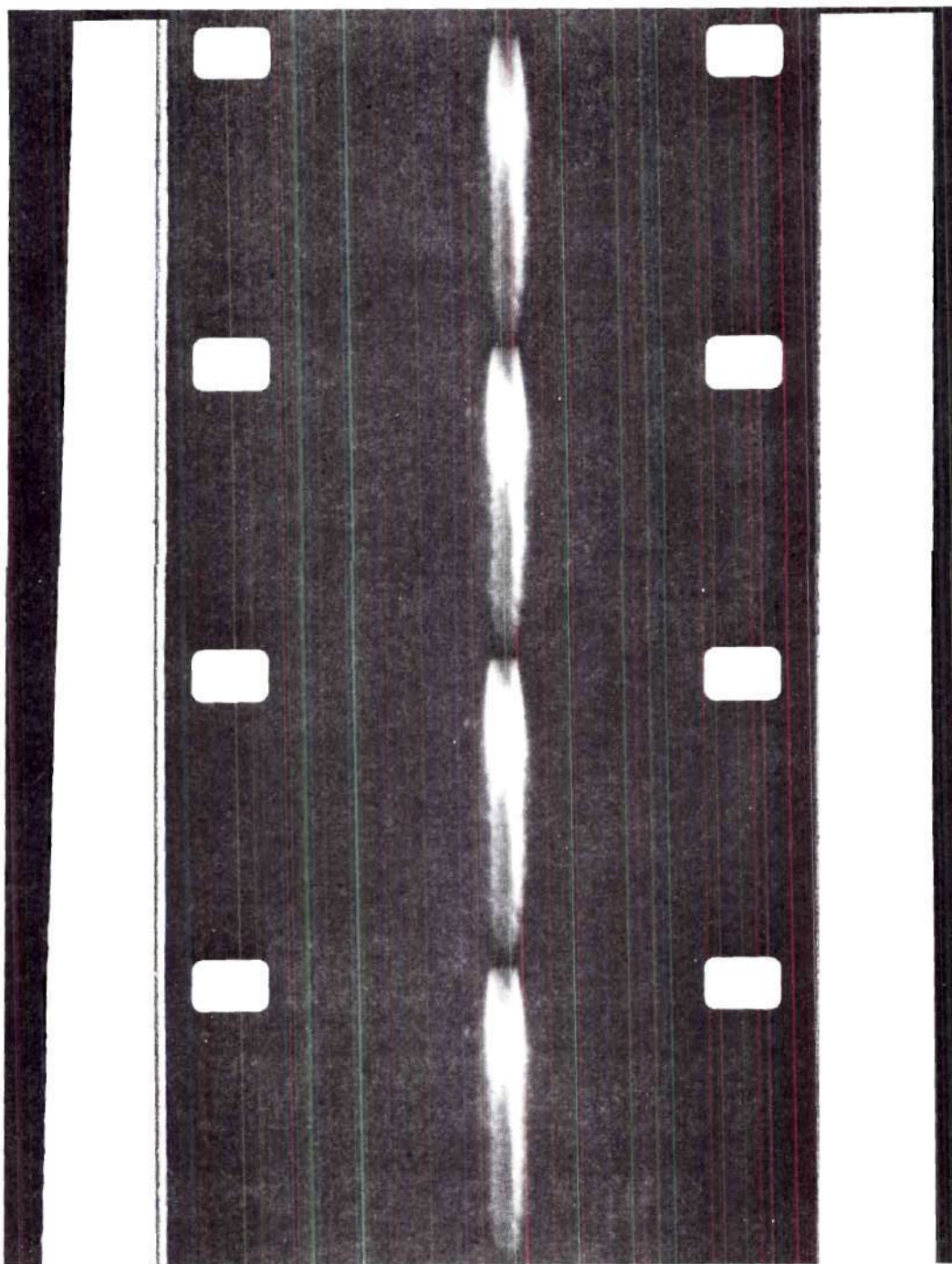
Figure 1. Flame with Entrained Particles.

directed at burning in an air environment rather than one corresponding
to the reaction envelope and its interior. The second part of the
particle study concerned the measurement of the aluminum mass distribu-
tion in the mixing region. This was accomplished by a direct sampling
technique.

Several experimental measurement techniques which apparently have
not been used before were developed during this investigation. The first
was a heat flux ratio technique for determining the temperature of a flow-
ing gas at temperatures where a radiation correction would normally be
required. This technique permitted the gas temperature to be deter-
mined with a thermocouple probe in such a fashion that the measurement
was independent of the probe's emissivity and Reynolds number, and gas
mixture properties. Although the technique was not extensively evalu-
ated in this work it appears to be useful with flows of this type.

The second technique involved determination of particle flow
rates and particle densities in the flame. The method avoids the prob-
lem of whether the particles were unburned, partially burned, or com-
pletely burned.

The results of an investigation of the turbulent mixing of two,
concentric, chemically reacting jets are presented in the following
chapters. Measurements were made of the velocity, temperature and
chemical species distributions for a central, hydrogen jet issuing into
a large, concentric air jet at a lower velocity. These data were com-
pared with a theoretical treatment of the problem.

A theoretical combustion model for aluminum burning was devel-
oped and the flame structure surrounding a droplet calculated assuming

chemical equilibrium to exist in this region. The criterion for the formation of condensed Al_2O_3 was presented. The experimental study was extended to the same type of flow described above but with entrained, aluminum particles in the hydrogen gas. The flame was studied by means of visual observations, high speed photography and particle-flux and particle density distribution measurements.

CHAPTER II

LITERATURE REVIEW

Jet Mixing

One of the earliest solutions to the problem of turbulent jet mixing was by Tollmien (1).[*] His treatment used Prandtl's mixing length theory for an incompressible jet discharging into a medium at rest. Abramovich (2), Pai (3) and Forstall and Shapiro (4) have surveyed the extensive literature in this field and have presented a discussion covering several hundred references as well as the results of their own investigations. Forstall and Shapiro (4) reviewed the earlier work up to about 1948.

Tollmien's original work was extended by Kuethe (5) to a two-dimensional jet discharging into a moving medium and by Squire and Trouncer (6) to the case of a circular jet issuing into a uniform stream with an assumed cosine velocity profile. Hinze (7) appears to have been the first to point out the mathematical inconsistencies for the case of identical initial velocities of the two jets.

Abramovich's (2) survey includes a systematic analysis of selected data on compressible jets. He has shown that the velocity profile in a compressible jet may be normalized in the same manner as in the incompressible case. Pai (8,9) has presented much of the earlier

---

[*]Numbers in parentheses refer to the references on page 182.

work on compressible jets. He assumed constant eddy diffusivity across
the mixing region and discussed turbulent mixing of a two-dimensional
jet and an axially symmetric jet. His results included laminar and
turbulent mixing of two different compressible gases.

Schlichting (10) presented a procedure for solving the turbulent
boundary layer equations assuming the eddy diffusivity constant in the
radial direction and the pressure constant. The solution was in terms
of an experimental scale factor which depends on the spreading of the
mixing region. Some experimental data in terms of a scale factor on
jet mixing has been reported by Pai (3).

Hawthorne, Weddell and Hottel (11) experimentally investigated
mixing and combustion in turbulent gas jets. The experimental work
involved injection of gaseous fuel into stagnant air. A simple rela-
tion for the length of free turbulent flame jet was given.

Most of the more recent literature on turbulent mixing of
reactive gases has been related to work on advanced ramjet engines.
Alpinieri (12) reported results of an experimental study of coaxial
jets of hydrogen and air and carbon dioxide and air with measurements
at high subsonic Mach numbers and with equal velocities and equal mass
flows in the jets. It was concluded that no tendency toward segrega-
tion of the stream exists whenever the velocities or the mass flows of
the streams are equal. Also, the measurements showed that mass diffuses
more readily than momentum and that the eddy viscosity varies only with
axial position.

Ferri (13) has reviewed a series of experimental and theoretical
studies on the mixing of non-reacting jets and the supersonic combustion

of hydrogen and air. Results are given for finite rate kinetics in inviscid flows and for the turbulent mixing of chemically reacting gases.

Libby (14) presented an analytical solution to the turbulent mixing of an axially symmetric fuel jet with a coaxial stream of air. The theory assumes the turbulent Prandtl and Lewis numbers unity so that the energy equation reduces to the same form as the momentum and diffusion equations. Also, the assumption is made that no pressure gradient exists and that the eddy properties are constant or vary only with axial position in the flow. A von Mises type transform was employed to transform the boundary layer equations. A relationship between Prandtl's eddy viscosity for incompressible flow and the compressible case was introduced, which resulted in a transformed equation and boundary conditions for which an analytical solution was available. This solution corresponds to the circular probability function which has been tabulated by Masters (15).

Donaldson and Gray (16) extended the use of Warren's momentum integral method for predicting the turbulent mixing and decay of axially symmetric, compressible free jets, to the case of mixing dissimilar gases. Comparison of data from a series of experiments led to the formulation of a relationship between a local mixing rate parameter and the local Mach number at each axial position in the jet where the velocity had decayed to one-half its centerline value.

Kleinstein (17,18) studied both laminar and turbulent jets using a method similar to Libby's theory for the latter. The laminar analysis was compared with the earlier finite difference solution of Pai (3).

The turbulent solution relied on an experimentally determined constant rather than on Libby's treatment of eddy viscosity. Good agreement was noted at low velocities but at high velocities considerable deviation of experimental data and the analysis was noted. Zakkay, Krause and Woo (19) developed equations for the turbulent properties which could be solved with known profiles of concentration, velocity, density and stagnation enthalpy. Experimental data was obtained with dissimilar gas jets which showed the jet decay to be unaffected by the molecular weight of the gases or by the development of a boundary layer on the inner jet nozzle. The compressible jet decay was inversely proportional to the square of the ratio of the distance from the nozzle exit and the potential core length.

Zakkay and Krause (20, 21) observed a significant variation of the eddy viscosity in the radial direction for coaxial, turbulent jets when the injected gas was lighter or heavier than the outer stream. Experimental studies on coaxial jets with and without chemical reaction showed that in contrast to the mixing process which is not affected by the boundary layer on the inner jet nozzle, a large effect was observed on the flame shapes.

Gray, Williams and Fradkin (22) studied the mixing of a central argon stream, highly heated by an arcjet, with a coaxial flow of cold helium. Data was obtained on free and ducted jets by Schlieren photography and with a calorimetric sampling probe. The dominant mixing process was the inflow of the helium.

Forde (23) performed experimental measurements on the turbulent mixing of supersonic streams of carbon dioxide and air. His data was

correlated by a spreading rate parameter determined from measured velocity profiles. He concluded that subsonic mixing theories could be applied to his experimental conditions with good agreement.

Chervinsky and Manheimer-Timnat (24) obtained data on velocity and temperature profiles with liquified petroleum flames in air. An analysis similar to Libby's was compared with the experimental results. It was concluded that for these flames the turbulent eddy viscosity was constant, depending on the flame temperature, while the turbulent Prandtl number varies throughout the flow.

Entrained Particle Flow

Rosenweig (25) experimentally investigated turbulent jet mixing using smoke particles suspended in a free jet of air. A light scattering technique was used to measure the concentration of smoke in the flow. The Schmidt number for gases is close to one and ranges from 10^2 to 10^4 for liquid systems. For the smoke-air system at 1 atmosphere and $77^\circ F$ the Schmidt number was approximately 6×10^3, or closer to that of a liquid than a gas. The average diameter of the smoke particles was one micron. The results showed the diffusion of heat and mass to be similar, and faster than that of momentum.

Rigid particle suspensions in turbulent shear flows have been studied experimentally due to the importance of such flows in industrial chemical processing (26,27). These experiments were conducted on spherical, almost neutrally buoyant particles in pipe flow. The friction factor was observed to increase with increasing particle concentration and decreasing particle size. The velocity profiles for the

small particles exhibited higher centerline velocities and sharper profiles than for the coarse particles.

Marble (28) discussed the relations governing the flow of a gas with entrained solid particles without chemical reactions. Three cases were considered, boundary layer flow, uniform flow and a Prandtl-Meyer expansion.

Soo (29) formulated gas dynamic equations involving solid particles including momentum and heat transfer between the solid and gaseous phases. The results applied to a one-dimensional expansion of gas-solid particle systems and to relaxation phenomena behind shock and rarefaction waves propagating through a particle laden gas.

Rudinger (30) studied the effects of particle volume in gas-solid systems and obtained a solution for a particle mass fraction of 0.3. The particle volume effects on the flow were neglected for this case.

Yu and Klein (31) studied the diffusion of small particles through a non-uniform atmosphere. The theoretical treatment was based on two different models of an apparent diffusion coefficient, both of which vary with pressure.

Kriebe (32) analytically studied the internal structure of a normal shock wave in a perfect gas heavily laden with particles. Numerical solutions were obtained on a digital computer for a particle-size distribution. The results predicted large shock wave thicknesses of the order of several inches at moderate pressures.

Hoglund (33) reviewed the problem of two-phase nozzle expansion relating to the use of metallic fuel additives in a rocket fuel. The

review covered several analytical studies and discussed particle size distribution, particle drag, heat transfer between phases, transport properties and boundary layer effects.

Gilbert, Davis and Altman (34) presented a theoretical treatment of the motion of a solid particle in a flowing gas. The flow was one-dimensional with a constant velocity gradient. Stokes' flow was assumed and the equation of motion integrated. It was pointed out that even small particles may lag the gas flow by a considerable amount. An empirical correlation was listed as a function of Reynolds number for use with large particles for which Stokes' flow is not valid. This technique may be applied to a non-linearly accelerated flow by simply dividing the flow into regions where the velocity gradient may be treated as constant.

Sargent and Anderson (35) studied the problems directly relating to an air-augmented solid propellant rocket. The effects of particle lag on the performance of the rocket were analytically treated under the simplifying assumptions of Stokes' flow, unit turbulent Prandtl number, uniform particle distribution, no particle-particle interactions and no pressure gradient. The ignition and combustion of metal particles in a turbulent mixing region was also discussed.

Particle Combustion

Much of the early work on particle combustion was directed at the process of burning pulverized coal in an air stream. Nusselt (36) was the first to point out that the burning times of particles could be increased due to the combustion of other particles in the same neighborhood and that the burning time of a single particle was proportional

to the diameter of the particle squared. His results were modified by Essenhigh and applied to burning in an idealized dust flame (37) and to the burning of coal particles in a furnace (38). Orning (39) made experimental measurements on the particle size effect on burning times for different types of coal dust. The results, however, are more suited for comparing types of coal due to the manner in which the measurements were performed.

The early work on metal particle combustion was primarily related to prevention of dust explosions and the production of intensive light emission. Gross and Conway (40) and Glassman (41) presented a survey of much of the earlier work on metal combustion.

In recent years the work in the area of metal combustion has greatly intensified due primarily to the use of metal additives in fuels, but the present knowledge of the process is far below that of combustion of conventional fuels.

Markstein (42) in a very informative review paper has discussed the distinctive aspects of metal combustion. He points out that a penalty results for the large exothermic heats of formation of metal oxides in the form of very stable, condensed-phase substances and that many peculiarities of metal combustion arise from these condensed-phase products.

Bartlett, et al. (43) studied aluminum combustion kinetics by using high speed photography. A combustion model was described which assumed a shell of liquid alumina around an aluminum droplet with metal vapor separating the metal and oxide. The burning rate was controlled by the diffusion of oxygen through the liquid alumina.

Coffin and Brokaw (44) presented a general system for computing burning rates of particles and droplets. The technique employed a model which assumed chemical equilibrium to exist throughout and permitted calculation of the concentrations and temperatures across the reacting region. Results were given for carbon, boron, magnesium and isooctane.

Friedman and Macek (45) performed an experimental study of the ignition and combustion of individual aluminum particles in hot, ambient gases. Oxygen concentration and particle size were varied and the phenomena studied with flame photography and by microscopic examination of collected particles. It was observed that ignition occurred only at temperatures above approximately 3500°F. The ignition was insensitive to oxygen concentrations. The combustion, after ignition, was described as extremely complex and a qualitative discussion of the process was given.

Macek (46) presented the results of a comparative examination of the ignition and combustion characteristics of small, single particles of aluminum and beryllium. It was reported that ignition of both metals was strongly influenced by physical properties of the respective stable oxides. Self-sustained combustion of both metals was thought to be by the vapor-phase mechanism, controlled by oxygen diffusion from the ambient gases.

Kuehl (47) reported the results of theoretical and experimental studies on ignition and combustion of metals. His experimental data showed that ignition temperature depended on the metal species, the pressure and the oxidizer concentration and species. Of particular importance was the observation that both aluminum and beryllium could

be ignited far below the melting point of their respective oxides.

Courtney (48) has reviewed both theoretical and experimental concepts in condensation occurring during heterogeneous combustion. The theoretical discussion emphasized condensation kinetics, thermal radiation and heat release. It was noted that present work was exploratory and definitive experimental or theoretical work had not been done.

Brzustowski (49) has described the combustion of single droplets of aluminum and magnesium by an extension of the vapor phase, diffusion flame theory. The theory was modified to consider radiation and metal evaporation. Experimental studies were conducted to determine the region of validity of the vapor-phase diffusion flame model.

CHAPTER III

INSTRUMENTATION AND EXPERIMENTAL APPARATUS

Experimental Apparatus

Experimental Chamber

A chamber was built to conduct the experimental runs in this
investigation. The chamber was fabricated from a large steel duct and
mounted on a steel frame. A schematic drawing of the chamber is shown
in Figure 2, page 17. The chamber and supporting frame are 5.5 feet
high. The chamber has a diameter of 17 inches. It has four sealed
observation ports, two on each side, and an access door at the front.
A two-inch wide, vertical slot is located at the rear of the test cham-
ber for instrumentation. The slot was sealed by means of a large,
flexible bag made from heavy cloth coated with Teflon. The open end
of the bag was attached completely around the edge of the vertical
slot. An instrumentation probe was passed through a small hole in the
other end of the bag and sealed with tape. The bag was loose enough to
permit the probe to be moved horizontally across the chamber and ver-
tically the length of the slot while maintaining a sealed chamber.

A tracking mechanism is shown mounted on the rear of the cham-
ber in Figure 2. A picture of this device is shown in Figure 7, page 29.
The probe may be moved vertically or horizontally by rotating the knobs
on the tracking mechanism. The entire mechanism was firmly attached
to the chamber adjacent to the vertical slot.
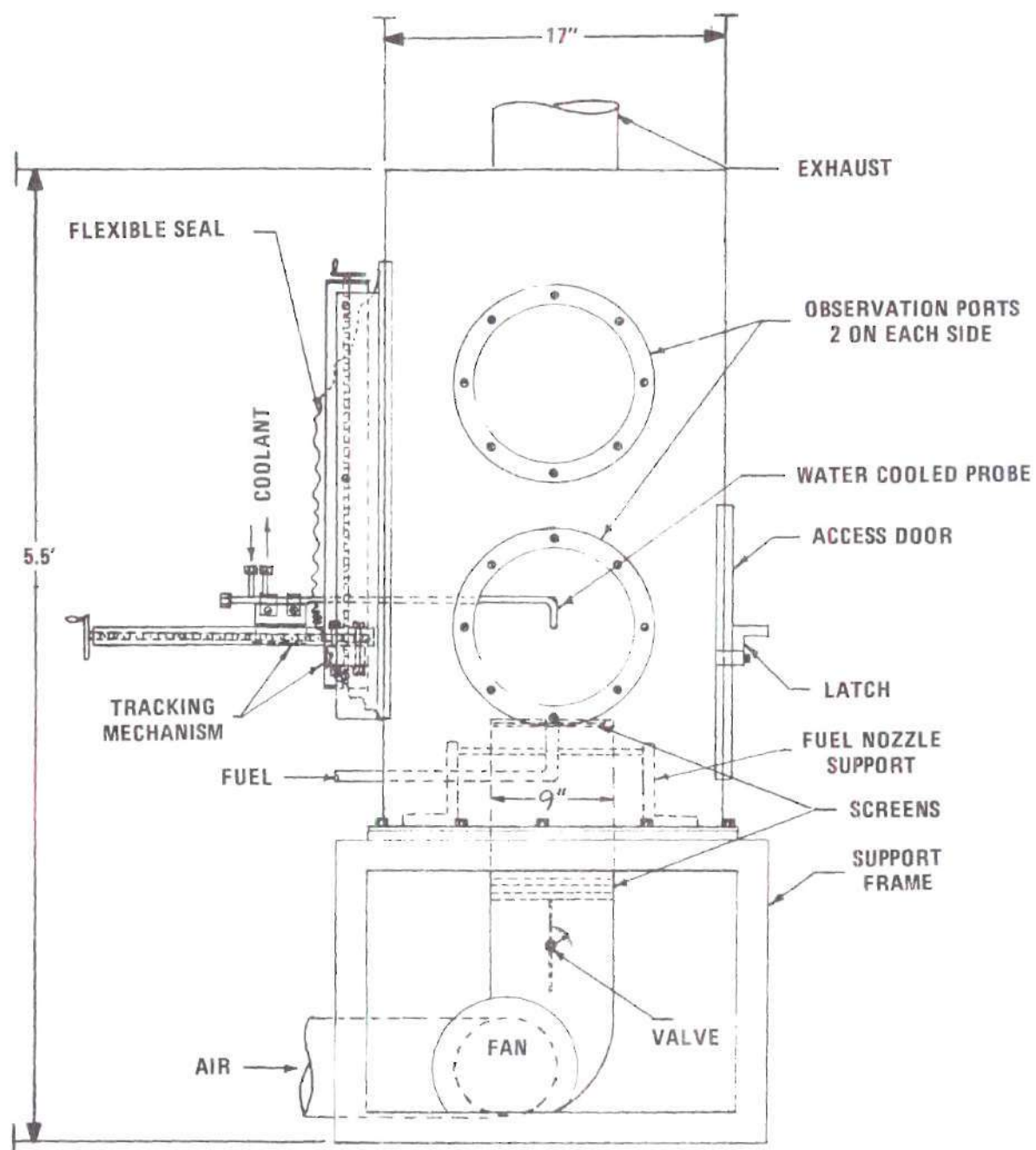
Figure 2. Experimental Chamber

Air was supplied to the bottom of the chamber by means of a nine-inch diameter duct passing up through the chamber floor. A motor driven fan was attached to the duct at the base of the support frame. Immediately above the fan a damper valve was installed to control the air flow. Several screens were placed above the valve to aid in smoothing the flow. A screen was also placed over the end of the air duct at the fuel inlet.

The fuel nozzle was mounted vertically in the center of the air duct and supported by two, 1/8-inch wide, steel braces across the duct below the screen and attached to the chamber floor. The nozzle consisted of a straight, 3-inch long, thin wall, stainless steel tube 1/8-inch in diameter. The end of the tube was passed through a hole in the screen at the exit of the air duct. The nozzle exit was located level with the screen.

Instrumentation

Thermocouple Probe

A portion of the temperature profile measurements was obtained by means of a small diameter, metal sheathed, thermocouple probe. The probe was 1/16-inch in diameter with magnesium oxide insulation. The thermocouple was a chromel-alumel thermocouple, welded to the inside of the metal sheath at the probe tip. The probe had a hemispherical tip attached to a cylindrical body as illustrated in Figure 3, page 19. This probe was used with a novel technique to measure gas temperatures. This technique is explained in the following sections.

Steady State, Heat Flux Ratio Technique. Prior to this investigation

THERMOCOUPLE WIRES

METAL SHEATH

HEMISPHERICAL TIP

MgO INSULATION

POSITION 1

FLOW DIRECTION

d

POSITION 2

FLOW DIRECTION
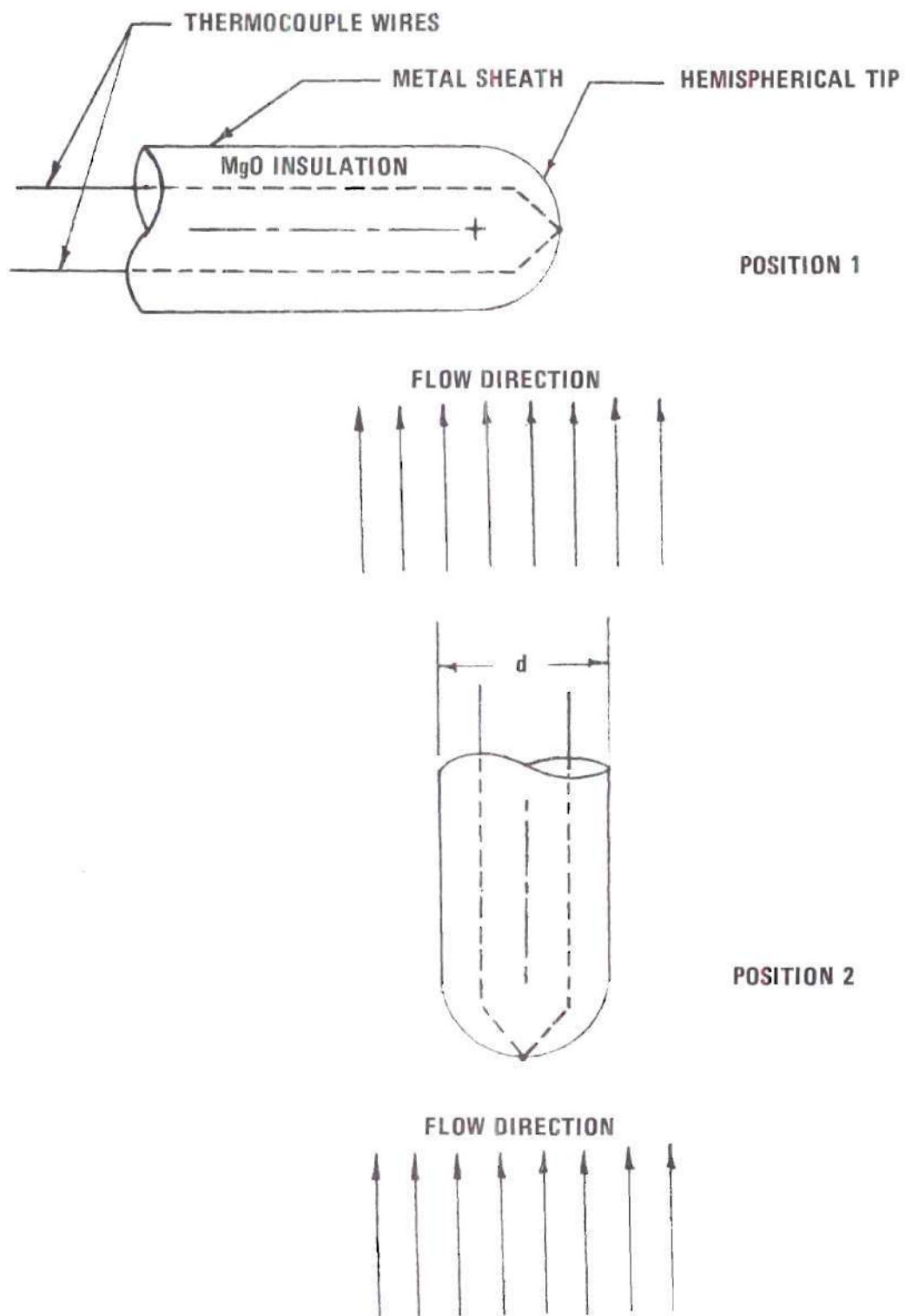
Figure 3. Thermocouple Probe Orientation

this method apparently has not been used to measure high temperatures in flowing gases. This technique was developed during this study. It is based on the fact that the local Nusselt number for a sphere at the stagnation point is a constant multiple of the Nusselt number for a different position on the sphere (for a laminar boundary layer).

The Nusselt number for the stagnation point on a sphere for laminar boundary layer flow can be written (50, 51)

$$Nu_0 = 0.570 \ Pr^{0.4} \sqrt{2 \frac{d}{u_\infty} [\frac{du}{dx}]_0} \sqrt{Re_d} \qquad (3-1)$$

where

x = distance along surface measured from the stagnation point

d = diameter of the sphere

u_∞ = gas stream approach velocity

u = free stream velocity outside boundary layer

$[\frac{du}{dx}]_0$ = free stream velocity gradient at the stagnation point

If incompressible potential flow outside the boundary layer of the sphere is assumed, the following may be used (50, 51)

$$u = Cx = 3 \frac{u_\infty}{d} x \qquad (3-2)$$

so that

$$[\frac{du}{dx}]_0 = \frac{3u_\infty}{d} \qquad (3-3)$$

and thus equation (3-1) becomes

$$Nu_0 = 0.570 \ Pr^{0.4} \sqrt{6 \ Re_d} \qquad (3\text{-}4)$$

At a position θ radians away from the stagnation point the Nusselt number can be expressed as (52)

$$Nu_\theta = 0.763 \ Pr^{0.4} \sqrt{Re_x} \qquad (3\text{-}5)$$

In this case the surface distance x is related to diameter of the sphere by

$$x = d \ \frac{\theta}{2} \qquad (3\text{-}6)$$

The equation for Nu_θ can thus be written

$$Nu_\theta = 0.763 \ Pr^{0.4} \sqrt{\frac{\theta}{2}} \sqrt{Re_d} \qquad (3\text{-}7)$$

Dividing equation (3-7) by equation (3-4) yields

$$\frac{Nu_\theta}{Nu_0} = 0.382 \sqrt{\theta} \qquad (3\text{-}8)$$

This ratio is a constant for a fixed position on the sphere for laminar boundary layer flow. The significance of this lies in the implication that the ratio of the heat transfer coefficients for the two positions on a sphere is independent of Reynolds number and of gas mixture properties so long as they do not change around the sphere.

The following approach was used to develop an expression for the gas temperature in terms of measured quantities for the hemispherical tipped thermocouple probe used in this investigation. Measurements were

obtained with the probe oriented in two different positions as shown in Figure 3. Conduction in the probe and energy by radiation from the combustion products are neglected in this approach. The radiative flux from the probe in position 1 may be approximated by

$$q = \sigma \bar{\varepsilon} F[T_1^4 - T_w^4] \qquad (3\text{-}9)$$

where

σ = Stephan-Boltzman constant

$\bar{\varepsilon}$ = probe emissivity

F = shape factor

T_1 = temperature of thermocouple, $^{\circ}R$

T_w = chamber wall temperature, $^{\circ}R$

This energy is supplied to the probe by convection from the combustion gases. Thus, a heat balance for position 1 can be expressed as

$$h_1[T_g - T_1] = \sigma \bar{\varepsilon} F[T_1^4 - T_w^4] \qquad (3\text{-}10)$$

Similarly for position 2 a heat balance can be expressed as

$$h_2[T_g - T_2] = \sigma \bar{\varepsilon} F[T_2^4 - T_w^4] \qquad (3\text{-}11)$$

assuming that the shape factor is the same as before. If equation (3-10) is divided by equation (3-11) and solved for T_g the result is

$$T_g = \frac{T_2 - \bar{a} \eta T_1}{1 - \bar{a} \eta} \qquad (3\text{-}12)$$

where

$$\bar{a} = \frac{T_2^4 - T_w^4}{T_1^4 - T_w^4} \qquad (3\text{-}13)$$

$\eta = \dfrac{h_1}{h_2}$ = a known constant for laminar boundary layer flow

Pulsed Thermocouple Probe

A schematic drawing of the pulsed thermocouple probe is shown in Figure 4, page 24. This device allows the determination of gas temperatures considerably above the melting point of the thermocouple being used (53). The thermocouple was cooled by a nitrogen jet and the coolant flow was intermittently stopped, exposing the thermocouple directly to the high temperature gas. The transient response of the thermocouple while the coolant flow was stopped was recorded with a Tektronix, type 555, dual beam oscilloscope which is shown in Figure 8, page 31. The gas temperature was determined from the transient response of the thermocouple using heat-transfer data and properties of the thermocouple wire.

The purpose of these measurements was to determine the temperature in the reacting region of the flow with a method different from the hemispherical tip, thermocouple probe used earlier. The pulsed thermocouple was made by butt-welding 28 gauge chromel and alumel wires. The junction and the wire contour was located and shaped so that the temperature gradients in the wire near the thermocouple junction should be minimized when the probe was placed at the reaction zone.

Powder Feeder

The aluminum particles were introduced into the hydrogen flow by
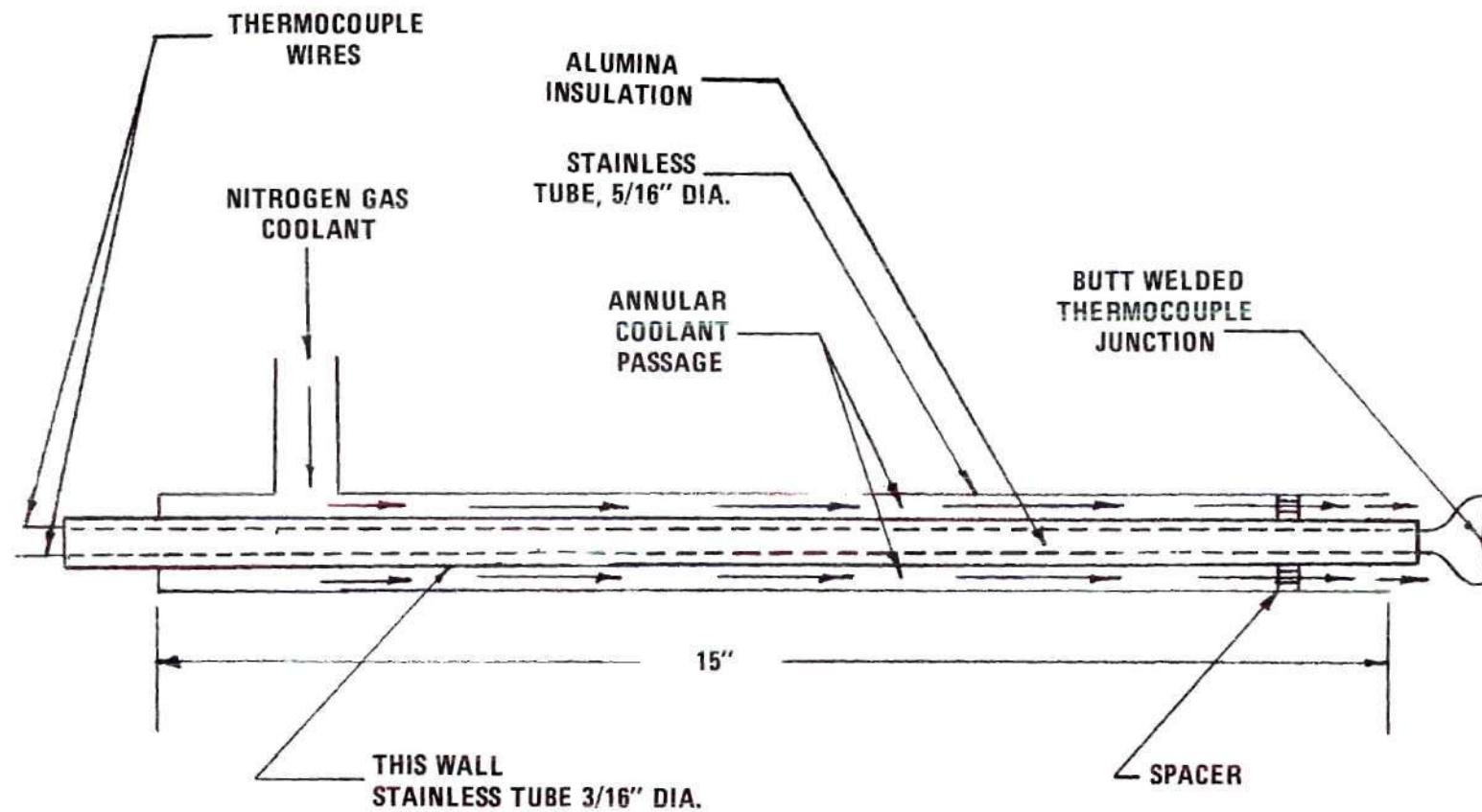
Figure 4. Pulsed Thermocouple Probe

means of a powder feeder. The device used in this study was a Metco Powder Feed Unit, type 3MP. Initially a vibratory feed device was tried in an attempt to introduce the particles, but the powder flow rate was difficult to measure accurately and difficult to adjust.

The Metco Feed Unit was not designed to use hydrogen as a carrier gas. In order to avoid introducing an inert carrier gas into the fuel flow it was decided to use the feed unit with hydrogen with certain precautions. First the entire device was pressurized and carefully checked for leaks. Second, a steady flow of nitrogen was directed underneath and around the unit while operating. Third, the device was operated immediately below a large exhaust duct located at the top of the room.

The unit was calibrated by operating the device at different feed-rate settings, collecting the particles over a measured time period and weighing the samples. The results of this calibration are shown in Figure 5, page 26.

Hydrogen Flowmeter

The fuel flow was measured by a Fisher and Porter Precision Bore Flowrater with a tapered tube number 2-L-150/13. The unit was originally calibrated by the manufacturer for air flow at standard conditions. It was recalibrated for this study against a Brooks Rotameter with a tapered tube size R-6-15-B which was calibrated by the manufacturer for hydrogen flow using a standard traceable to the National Bureau of Standards. The results of the calibration of the unit used in this investigation are given in Figure 6, page 27.

Water Cooled Probe

The water cooled probe which was used as the stagnation pressure
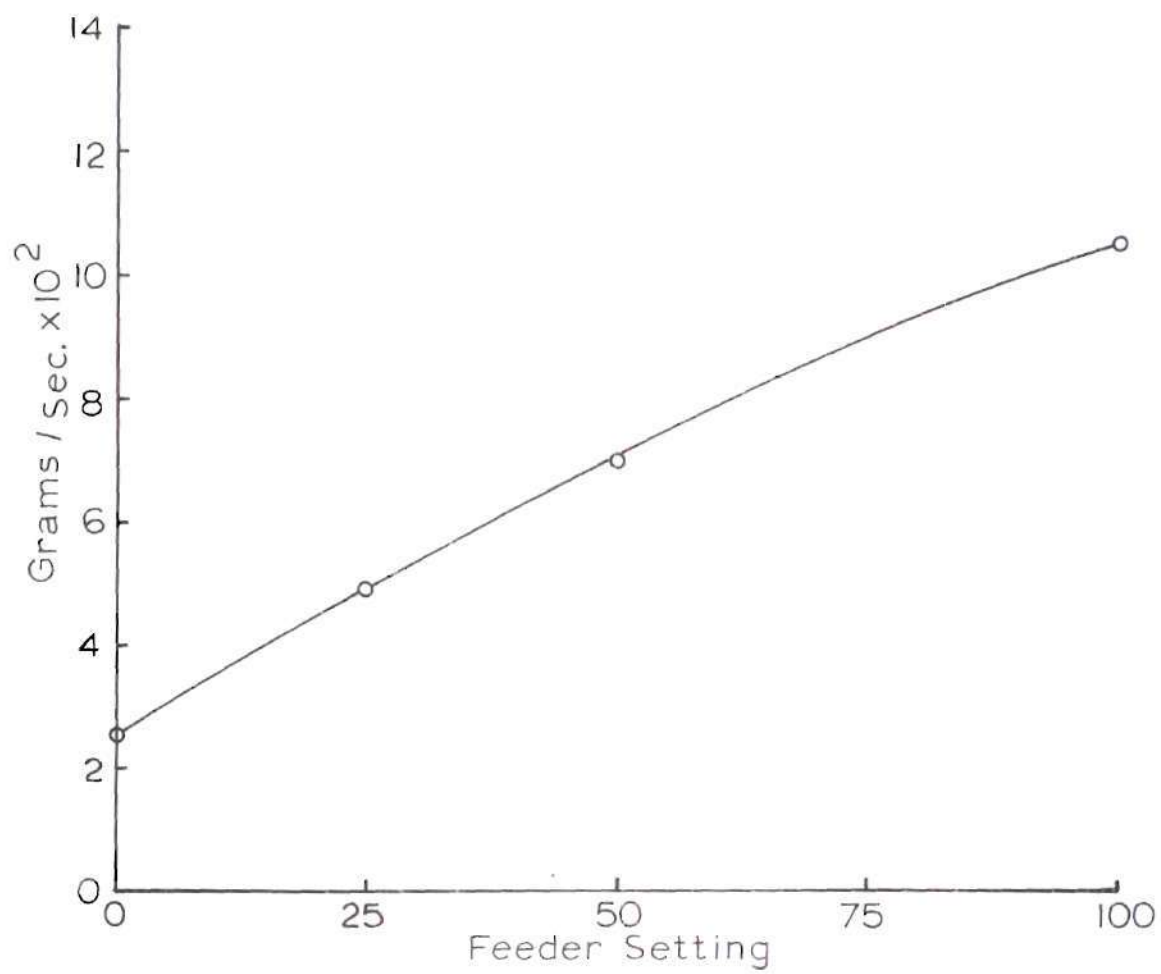
Figure 5. Powder Feeder Calibration
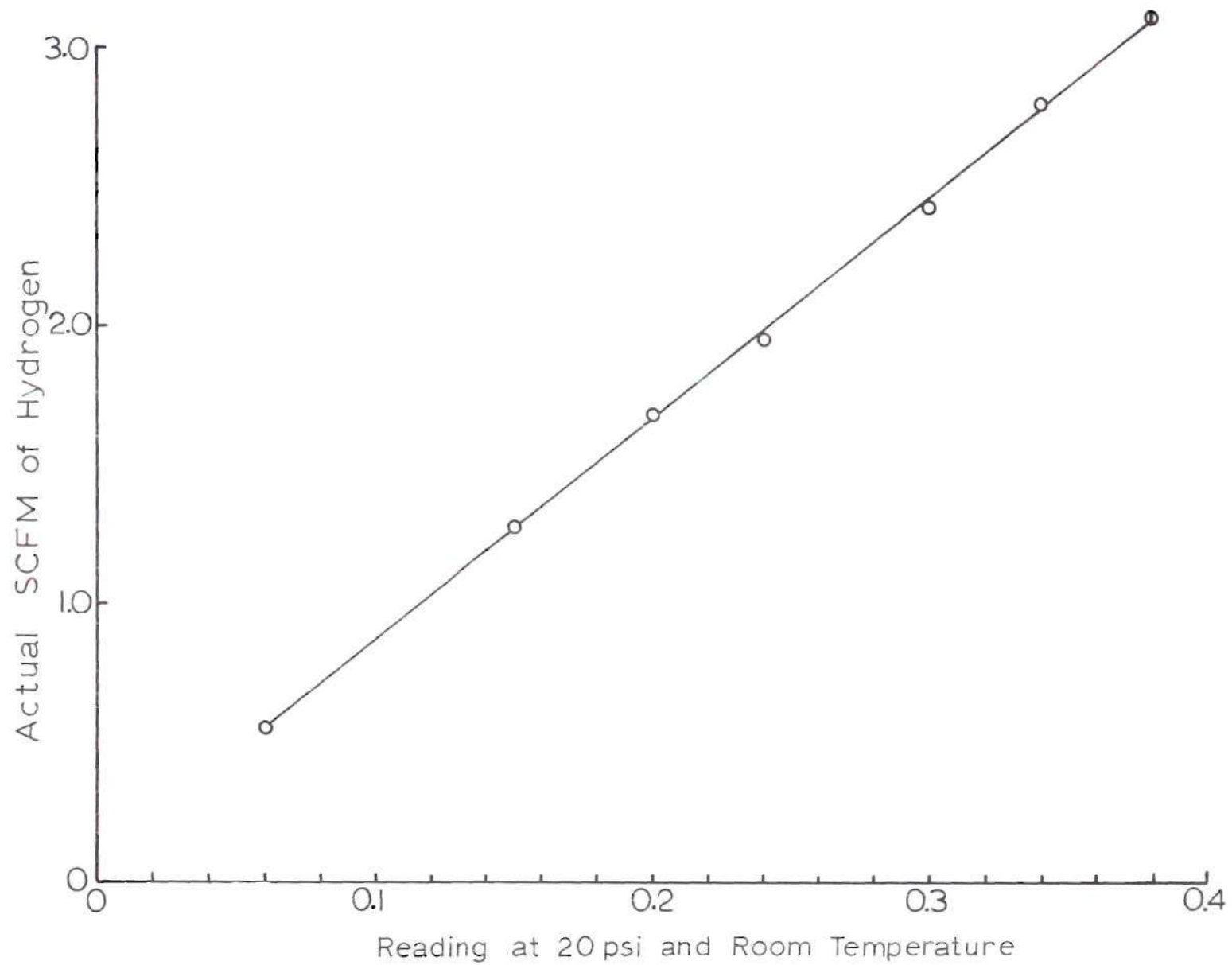
Figure 6. Flowmeter Calibration

probe and as the sampling probe is shown in Figure 7, page 29. The probe was constructed by forming small, 0.050-inch diameter, stainless steel pressure tubing, which had been bent 180 degrees, into a bundle around a single tube the same size. The bundle was carefully bent into the desired shape and silver-soldered together with the single, open tube in the center. The tip was rounded by adding additional solder and shaping with abrasive paper. The single tube was cut off flush with the tip. The six ends of the bent tubes were fastened together and divided equally as inlet flow tubes and outlet flow tubes. These are shown in Figure 7, page 29, with an aluminum support and attachment brace with the single pressure tube in the center. The outside diameter of the probe is 0.156 inches. The length measured from the end of the aluminum support is 9.5 inches and the tip extends downward 0.75 inches at a right angle to the length of the probe.

The primary difficulty encountered in fabricating this probe was bending the small diameter tubes 180 degrees without blocking the tubes. This was accomplished by inserting a soft wire into the stainless steel tubes before any shaping was done. The tubes were bent 180 degrees and then heated at the bend with a gas flame. The soft wire oxidized within the tube at the bend and broke due to the heating. The wire was pulled out in two pieces, one from each side of the bend leaving a satisfactory passage for coolant flow.

Chromatography and Neutron Activation Analysis Equipment

The chemical species measurements were obtained by use of a Beckman Instruments, Inc., Gas Chromatograph, model GC-2A. A Beckman Instruments, Inc., 10-inch recorder-integrator, model 1005 was used to
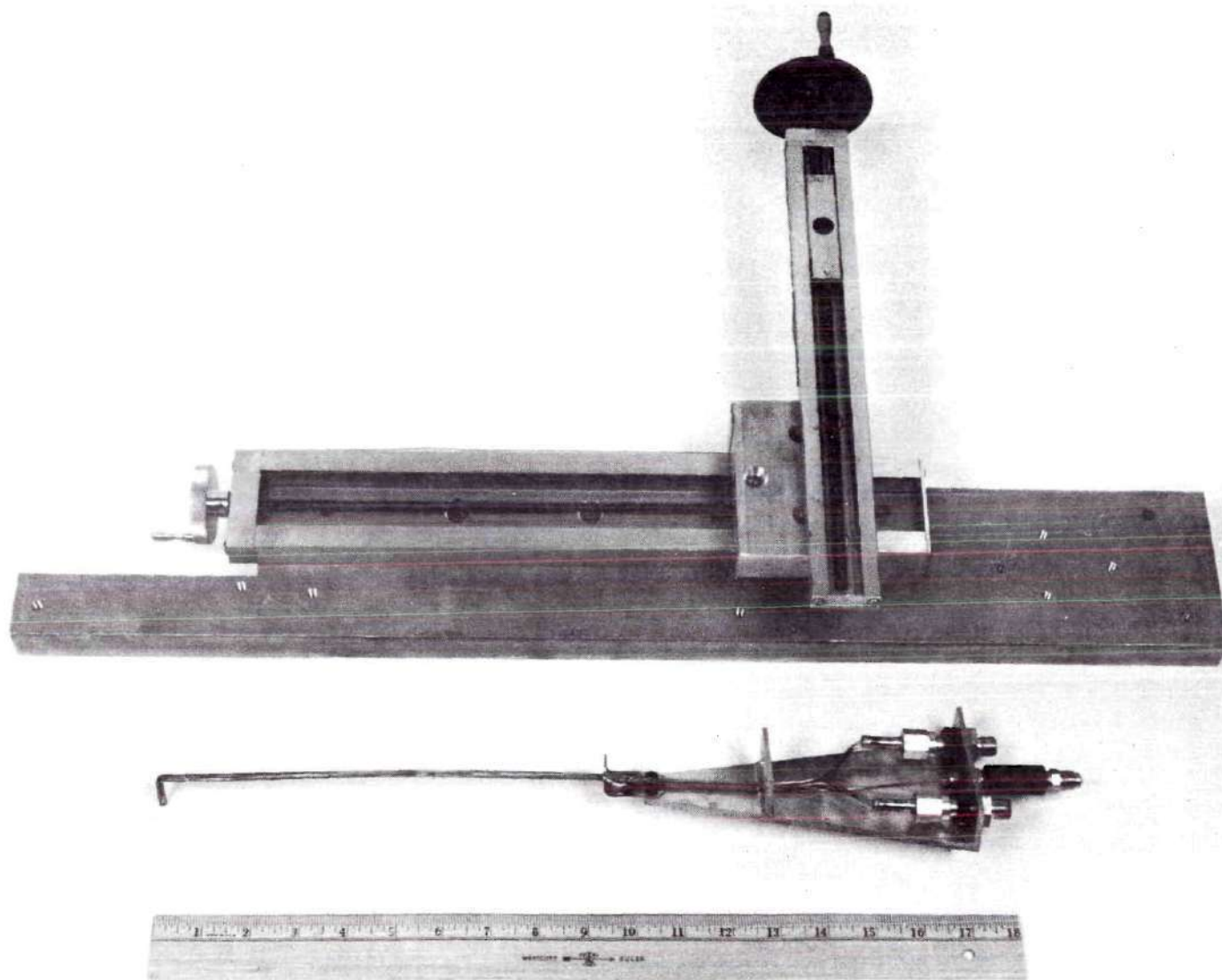
Figure 7. Water Cooled Probe and Tracking Mechanism

record the signal from the chromatograph. These instruments are shown in the top photograph of Figure 8, page 31.

In the same figure the lower two photographs show the gamme ray spectrometers used in the neutron activation analysis. This equipment is located in the Nuclear Research Center. The aluminum peak data were obtained using the Nuclear Data-2200 series, 1024 channel gamma ray spectrometer. The system used a high resolution, semiconductor, 16cc Ge (Li) detector.
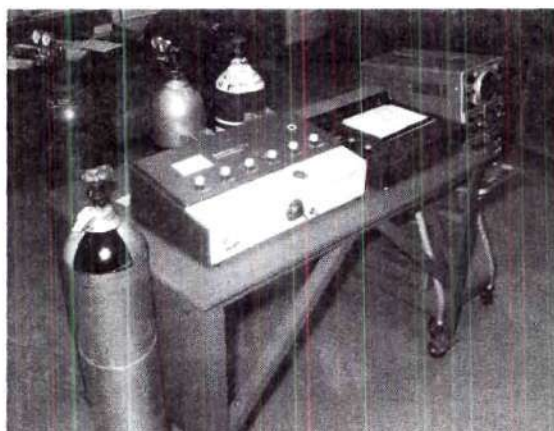
(a) GAS CHROMATOGRAPH
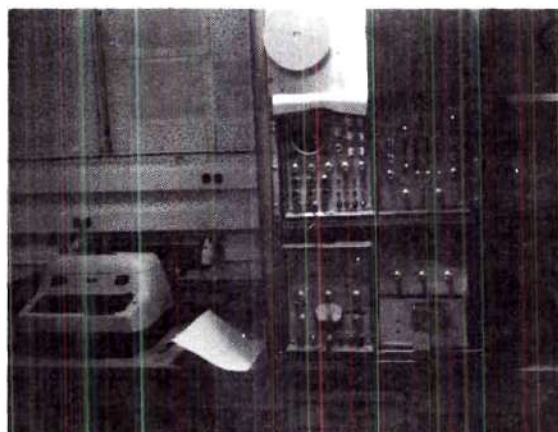
(b) GAMMA RAY SPECTROMETER
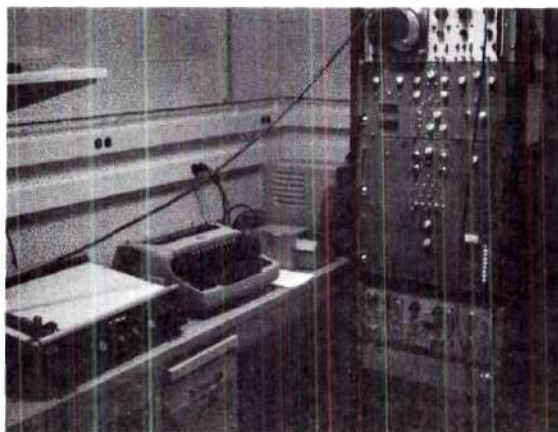
(c) GAMMA RAY SPECTROMETER

Figure 8.   (a) Gas Chromatograph (b) Gamma Ray Spectrometer
(c) Gamma Ray Spectrometer

CHAPTER IV

THEORETICAL ANALYSIS

In the first part of this chapter the analysis for two concentric, turbulent, chemically reactive jets is presented. The presentation begins with the differential equations of continuity, momentum, energy and species continuity for axially symmetric, turbulent flow. The simplifying assumptions are presented with the development of the equations. The analysis follows that of Libby (14). The stream function as used in this analysis utilizes a free parameter, n, as an exponent and results in a family of solutions.

The particle temperature as a function of time is presented in the second section of this chapter. The pre-ignition heating of a particle is assumed to be by convection as it traverses a flow field of variable temperature, concentration, and velocity.

The combustion model of a single aluminum particle, burning in air, is presented in the last part of this chapter. The model developed is based on the observations of several investigators (42, 43, 46, 49). This analytical model permits the complete flame structure under chemical equilibrium conditions to be determined. The thermodynamic restrictions relating to the complex condensation phenomena are developed for this combustion model.

Concentric Jets

The coordinate system for the flow is illustrated in Figure 9,
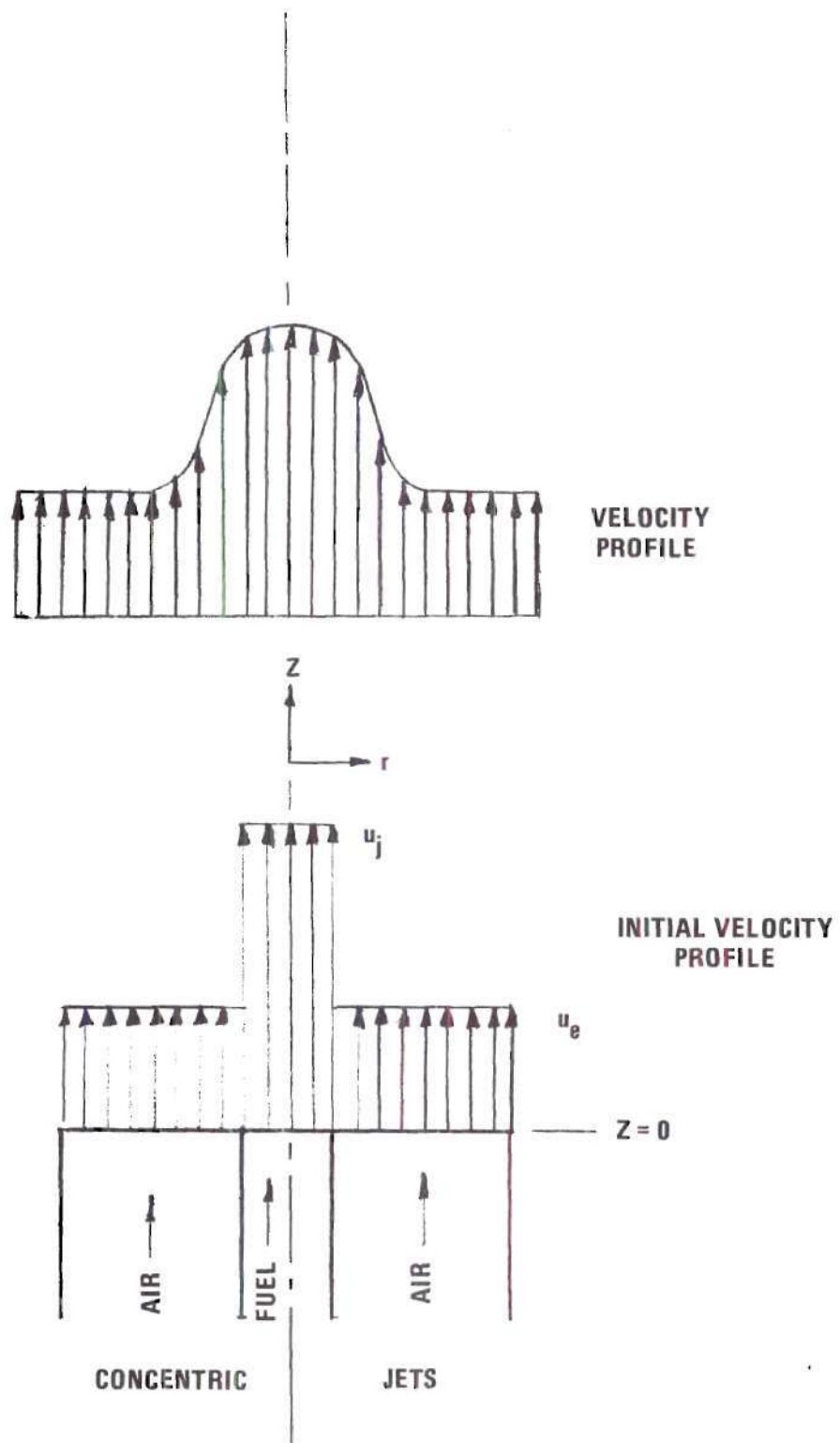
Figure 9.   Concentric Jets Coordinates

page 33. The nozzle exit is taken as z = 0 and the wall effects of the nozzle are neglected in the analysis. The free stream is assumed infinitely wide. The development of the differential equations used to describe the flow for the case of a uniform jet flowing into an infinite medium at a uniform velocity have been presented by several investigators (7, 10, 17) and are listed here for completeness. These equations for turbulent flow and the applicable boundary conditions are listed below for zero pressure gradient and no body forces. It is also assumed that the eddy transport properties are all equal. The definitions of symbols used are given in the nomenclature, page xii. These equations are:

continuity:

$$\frac{\partial}{\partial z} (\rho u) + \frac{1}{r} \frac{\partial}{\partial r} (\rho v r) = 0 \tag{4-1}$$

momentum:

$$\rho u \frac{\partial u}{\partial z} + \rho v \frac{\partial u}{\partial r} = \frac{1}{r} \frac{\partial}{\partial r} (\rho \varepsilon r \frac{\partial u}{\partial r}) \tag{4-2}$$

energy:

$$\rho u \frac{\partial h}{\partial z} + \rho v \frac{\partial h}{\partial r} = \frac{1}{r} \frac{\partial}{\partial r} [\frac{\rho \varepsilon r}{Pr_t} \frac{\partial h}{\partial r} + (1 - \frac{1}{Pr_t}) \frac{\rho \varepsilon r}{2} \frac{\partial (u^2)}{\partial r} \tag{4-3}$$

$$+ (\frac{1}{Sc_t} - 1) \rho \varepsilon r \sum_i h_i \frac{\partial C_i}{\partial r}]$$

species continuity:

$$\rho u \frac{\partial C_i}{\partial z} + \rho v \frac{\partial C_i}{\partial r} = \frac{1}{r} \frac{\partial}{\partial r} \left(\frac{\rho \varepsilon r}{Sc_t} \frac{\partial C_i}{\partial r} \right) + \dot{\omega}_i \tag{4-4}$$

The boundary conditions for the jet assuming that the outer stream is infinitely large are

$$0 \leq r \leq r_j$$
$$z = 0$$

$$u = u_j \qquad h = h_j \qquad C_i = C_{i_j}$$

$$r > r_j$$
$$z = 0$$

$$u = u_e \qquad h = h_e \qquad C_i = C_{i_e}$$

$$\text{as } r \to \infty$$

$$z > 0$$

$$u = u_e \qquad h = h_e \qquad C_i = C_{i_e}$$

If viscous dissipation is neglected and the turbulent Lewis number is equal to one, the energy equation reduces to the same form as the momentum equation. The last equation can be written in terms of element mass fractions, $\overline{C}$, which eliminates the generation rate term. In this manner the species continuity equation expressed in terms of the element mass fractions can be reduced to the same form as

the momentum equation.

For convenience, the following non-dimensional variables are defined:

$$\bar{U} = \frac{u - u_j}{u_e - u_j} \tag{4-5}$$

$$\bar{H} = \frac{h - h_j}{h_e - h_j} \tag{4-6}$$

$$\bar{\beta} = \frac{\bar{C}_k - \bar{C}_{k_j}}{\bar{C}_{k_e} - \bar{C}_{k_j}} \tag{4-7}$$

The boundary conditions for the new variables are

$$0 \leq r \leq r_j$$

$$z = 0$$

$$\bar{U} = 0 \qquad \bar{H} = 0 \qquad \bar{\beta} = 0$$

$$r > r_j$$

$$z = 0$$

$$\bar{U} = 1 \qquad \bar{H} = 1 \qquad \bar{\beta} = 1$$

$$as \quad r \to \infty$$

$$z > 0$$

$$\bar{U} = 1 \qquad \bar{H} = 1 \qquad \bar{\beta} = 1$$

Since the variables satisfy the same differential equation and have the same boundary conditions it follows that:

$$0 \le r < \infty$$

$$0 \le z < \infty$$

$$\bar{U} = \bar{H} = \bar{\beta}$$

A stream function is defined by

$$\rho u r = \rho_j u_j \frac{\partial}{\partial r} \left(\frac{\psi^n}{n} \right) \tag{4-8}$$

$$-\rho v r = \rho_j u_j \frac{\partial}{\partial z} \left(\frac{\psi^n}{n} \right) \tag{4-9}$$

where n is a free parameter.

The continuity equation is identically satisfied and the momentum equation becomes

$$\left(\frac{\partial u}{\partial z} \right)_\psi = \frac{1}{\psi^{n-1}} \frac{\partial}{\partial \psi} \left\{ \left[\frac{\rho u}{\rho_j u_j} \frac{\rho \varepsilon r^2}{\rho_j u_j} \frac{1}{\psi^{2n-2}} \right] \psi^{n-1} \left(\frac{\partial u}{\partial \psi} \right)_z \right\} \tag{4-10}$$

The bracketed term on the right containing the eddy viscosity has been treated by Libby (14) for the case of n = 2 by defining a relationship between the compressible eddy viscosity and the incompressible eddy viscosity such that the bracketed term is a constant or at most a function of z only. For the purpose of this analysis the bracketed term initially was assumed to equal one. Assuming it to equal a constant results in the same type of solution. In this case the transformed momentum equation can be written

$$\frac{\partial \bar{U}}{\partial z} = \frac{1}{\psi^{n-1}} \frac{\partial}{\partial \psi} \left(\psi^{n-1} \frac{\partial \bar{U}}{\partial \psi} \right) \tag{4-11}$$

with boundary conditions

$$0 \leq \psi \leq \psi_j$$

$$z = 0$$

$$\bar{U} = 0$$

$$\psi > \psi_j$$

$$z = 0$$

$$\bar{U} = 1$$

$$\psi \to \infty$$

$$\bar{U} = 1$$

The term ψ_j is defined as the value of ψ at $z = 0$ and r equal to r_j.

Three different solutions are available in the literature for this equation with these boundary conditions. These solutions correspond to different values of n. The equations are

For n = 1

$$\frac{\partial^2 \bar{U}}{\partial \psi^2} - \frac{\partial \bar{U}}{\partial z} = 0 \qquad (4\text{-}12)$$

For n = 2

$$\frac{\partial \bar{U}}{\partial \psi} + \frac{1}{\psi} \frac{\partial \bar{U}}{\partial \psi} = \frac{\partial \bar{U}}{\partial z} \qquad (4\text{-}13)$$

For n = 3

$$\frac{\partial^2 \bar{U}}{\partial \psi^2} + \frac{2}{\psi} \frac{\partial \bar{U}}{\partial \psi} = \frac{\partial \bar{U}}{\partial z} \qquad (4\text{-}14)$$

These equations are identical to the transient heat-conduction equations

for a plate, a cylinder and a sphere. The heat-conduction solutions
are given in reference (54) and are equivalent to values of $(1 - \bar{U})$ for
the jet mixing problem with $\dfrac{z}{\psi_j^2}$ as a parameter.

The solutions listed are for three integer values of n which
are available in the literature. However, the possible solutions are
infinite depending on the value of n selected. The result of changing
the value of n is to stretch or compress the profiles for given axial
positions. This technique offers another approach to matching experi-
mental data.

A second technique can be employed to further improve the match-
ing of theory and experimental data. This method assumes the bracketed
term in equation (4-10) to be a constant, C, resulting in

$$\frac{\partial^2 \bar{U}}{\partial \psi^2} + \frac{(n-1)}{\psi} \frac{\partial \bar{U}}{\partial \psi} = \frac{1}{C} \frac{\partial \bar{U}}{\partial z} \tag{4-15}$$

with the same boundary conditions as before. The solutions will be
profiles stretched according to the value of n as before, but in this
case the profile curves will correspond to different values of

$$\frac{Cz}{\psi_j^2}$$

This permits the family of profiles to be shifted along the axis
of the jet by a constant multiplier by selecting an appropriate value
of C.

A third technique may be used to improve the match with experimen-
tal data. If the bracketed term of equation (4-10) is assumed to be a

function of axial position only, then

$$\frac{1}{f(z)} \frac{\partial \bar{U}}{\partial z} = \frac{1}{\psi^{n-1}} \frac{\partial}{\partial \psi} (\psi^{n-1} \frac{\partial \bar{U}}{\partial \psi}) \qquad (4\text{-}16)$$

A new variable may be defined as

$$\zeta = \int_0^z f(z)dz \qquad (4\text{-}17)$$

so that equation (4-16) may be written as

$$\frac{\partial \bar{U}}{\partial \zeta} = \frac{1}{\psi^{n-1}} \frac{\partial}{\partial \psi} (\psi^{n-1} \frac{\partial \bar{U}}{\partial \psi}) \qquad (4\text{-}18)$$

In this case the solutions are the same as before except each profile corresponds to a value of the parameter

$$\frac{\zeta}{\psi_j^2}$$

The function $f(z)$ may be selected to position the profiles as desired along the centerline.

Generally, the mathematical techniques used here have been applied to flow problems by several investigators (11, 55, 56) and to the jet mixing problem by Libby (14). It appears that the use of the free parameter, n, as an exponent of the stream function which results in families of solutions, corresponding to stretched or compressed profiles, has not been presented before.

Pre-Ignition Particle Heating

A spherical, aluminum particle entrained in the hydrogen jet sees an environment that varies in both temperature and composition as the particle moves through the mixing region. The particle is heated by convection which increases rapidly as the particle approaches the flame envelope. Once across the flame envelope the particle environment changes sharply to the air-jet conditions with the exception of the flame tip region. Thus, the environment temperature of a particle may be expressed as a function of time depending on its particular trajectory and deceleration rate.

The pre-ignition heating of a particle for this case is treated by neglecting temperature gradients within the particle since the conductivity of aluminum is high, and the particles are small. It is assumed that only convective heating is significant until the particle reaches a region containing oxygen and other burning particles.

With these assumptions the rate of temperature change of a spherical particle may be written

$$\frac{dT}{dt} = \frac{\bar{h}A}{mC_p} (T_g - T) \tag{4-19}$$

where

T = instantaneous temperature

T_g = environment temperature

t = time

$\bar{h}$ = average heat transfer coefficient

A = area of the particle

m = mass of the particle

C_p = specific heat

If the environment temperature may be approximated by the function

$$T_g = a\, t\, e^{-bt} + T_{g_i} \qquad (4\text{-}20)$$

where a and b are constants depending on the particular trajectory

and T_{g_i} is the environment temperature at $t = 0$, equation (4-16) becomes

$$\frac{dT}{dt} = \frac{\bar{h}A}{mC_p}\left[a\, t\, e^{-bt} + T_{g_i} - T\right] \qquad (4\text{-}21)$$

The general solution to this equation with $(\bar{h}A/mC_p)$ constant is

$$T = C\, e^{-\frac{\bar{h}A}{mC_p}t} + \left[\frac{(\frac{\bar{h}A}{mC_p})}{(\frac{\bar{h}A}{mC_p}-b)}\, t - \frac{(\frac{\bar{h}A}{mC_p})a}{(\frac{\bar{h}A}{mC_p}-b)^2}\right]e^{-bt} + T_{g_i} \qquad (4\text{-}22)$$

The integration constant C may be calculated by assuming that at $t = 0$ the particle is at the temperature of the surrounding gas. Thus,

$$T = \left[\frac{\frac{\bar{h}A}{mC_p}a}{(\frac{\bar{h}A}{mC_p}-b)^2}\right]e^{-(\frac{\bar{h}A}{mC_p})t} \qquad (4\text{-}23)$$

$$+ \left[\left(t - \frac{1}{(\frac{\bar{h}A}{mC_p}-b)}\right)\left(\frac{\frac{\bar{h}A}{mC_p}a}{(\frac{\bar{h}A}{mC_p}-b)}\right)\right]e^{-bt} + T_{g_i}$$

Aluminum Particle Combustion

Analytical work in the area of metal combustion at elevated temperatures has been primarily qualitative or semi-quantitative in nature. This is due to the difficulties involved in developing and conducting experiments to study combustion mechanisms. Usually simplified combustion models are formulated so that approximate values of combustion temperatures and burning rates may be calculated without too much difficulty.

For this investigation it was noted that ignition did not occur until the particle passed through the flame envelope region. Examination of the species concentration data showed that within this region there was insufficient oxygen to support combustion and just outside this region the concentrations corresponded to ambient air. Since many of the particles passed through this region, ignited and burned in essentially an air environment, the analytical approach presented here is limited to this case. However, the model may be extended to the treatment of other chemical species and environments different than air by inclusion of appropriate reactions and equilibrium constants.

The approach used in treating an aluminum particle burning in air is based on the hypothesis that Al_2O_3 forms from the reaction of oxygen diffusing toward the metal surface with aluminum oxides of lower molecular weight than Al_2O_3.

It is assumed that in the vapor phase, diffusion-controlled combustion of aluminum the oxide, Al_2O_3, is formed away from the metal surface by reaction of AlO, Al_2O, or Al_2O_2 with oxygen. This process has been suggested by Markstein (42) and related to some of the

observed burning characteristics of metals. Radiation is not included in this model but could be approximated by the technique used by Brzustowski (49).

It is pointed out that at best the inclusion of gas-phase radiation could only be a crude approximation and that inclusion of surface radiation would result in a solution which is a function of the droplet diameter with the resulting loss in generality. Although it is recognized that radiation may be significant in aluminum combustion, for the purposes of this study considering the above facts it was not included in the combustion model.

The combustion model is illustrated in Figure 10, page 45. The metal is shown as cross hatched in the center, I, and is heated by the surrounding gases at high temperature in region II. Away from the metal surface a region where Al_2O_3 (liquid) forms is indicated by a broken line as region III. The liquid oxide is formed as small droplets, or smoke, and is conducted out through region IV. Within region II the following gaseous species are present in concentrations corresponding to chemical equilibrium:

$$Al$$
$$AlO$$
$$Al_2O$$
$$Al_2O_2$$
$$O$$
$$O_2$$
$$N_2$$

It is assumed that the flame structure within region II is not influenced

Al_2O_3

V

IV

O_2

II

A1

I

III
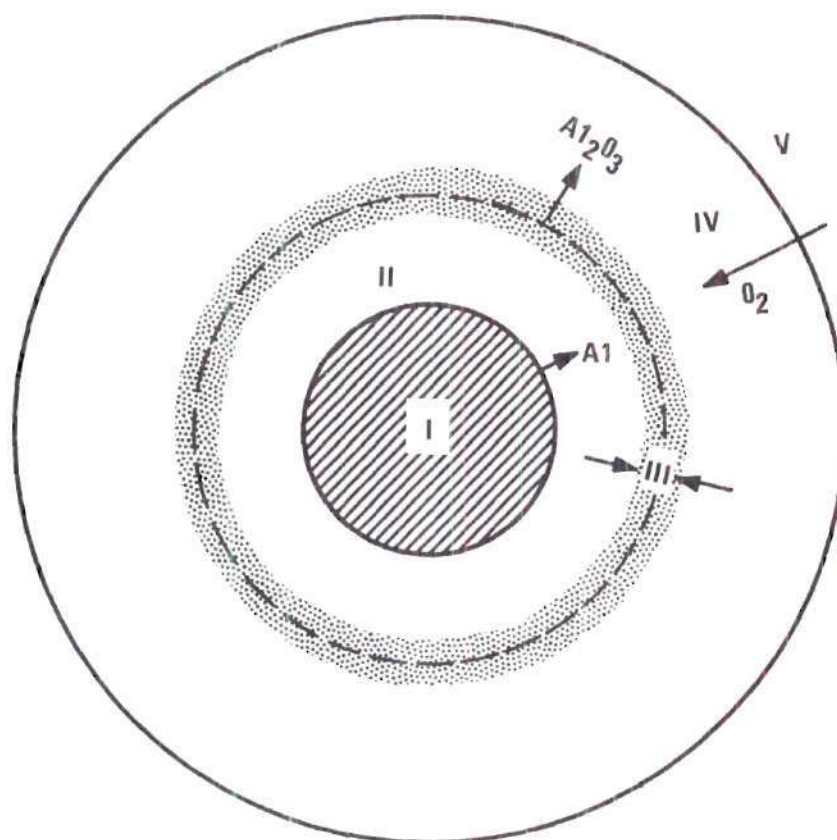
I — A1 DROPLET

II — GASEOUS REGION CONTAINING
    A1, A10, Al_2O, Al_2O_2, O, O_2, N_2.

III — REGION OF Al_2O_3 (LIQUID)
    FORMATION

IV — REGION OF Al_2O_3 DROPLET
    GROWTH AND SOLIDIFICATION

V — AMBIENT ENVIRONMENT.

Figure 10.   General Combustion Model

by the reaction of the gaseous oxides to liquid Al_2O_3. Once the con-
centration profiles and temperature profile are determined the position
where it is possible for Al_2O_3 to form may be located if chemical equili-
brium with the condensed phase is assumed.

The development of the equations for the processes described above
is presented in the following paragraphs. Generally, the equations
developed have been used by many investigators in the past but have not
been used in analyzing metal combustion (57).

Chemical equilibrium is assumed to exist throughout and the gas
mixture is assumed to be a perfect mixture of ideal gases. The alterna-
tives to assuming chemical equilibrium are frozen flow, and finite rate
chemical kinetics. Frozen flow could not be used with the combustion
model proposed here. Chemical kinetics requires the use of suitable
rate constants with established reaction mechanisms. Very little data
are available on the chemical reactions involved in aluminum combustion.
Also, the introduction of chemical kinetics into the analytical treat-
ment of the particle combustion would make the analysis prohibitively
long.

Diffusion Equation

It is assumed that the binary diffusion coefficients for all
pairs of the gaseous species are equal and Fick's Law for a binary
system with ordinary diffusion is applicable. The diffusion analysis
does not include condensed phases. Thus, for the gas mixture the mass
flux of the ith species can be written

$$\vec{n}_i = -\rho D_{ij} \nabla C_i + \vec{n} C_i \qquad (4\text{-}24)$$

To obtain an expression in terms of element mass fractions the index i may be replaced by k and multiplied by $r_{i,k}$, the mass ratio of element i present in species k, and summed over all species present to yield

$$\sum_k r_{i,k} \vec{n}_k = -\rho D_{ij} \sum_k \nabla(r_{i,k} C_k) + \sum_k (\vec{n}\, r_{i,k} C_k) \qquad (4\text{-}25)$$

Now,

$$\sum_k (\vec{n}\, r_{i,k} C_k) = \vec{n}\, \bar{C}_i = \text{element mass flux} \qquad (4\text{-}26)$$

and

$$\sum_k (r_{i,k} \vec{n}_k) = \vec{n}_i = \text{mass flux of element i} \qquad (4\text{-}27)$$

Thus

$$\vec{n}_i = -\rho D_{ij} \nabla \bar{C}_i + \vec{n}\, \bar{C}_i \qquad (4\text{-}28)$$

In terms of a net mass flux, $\dot{m}$, from sphere of radius r_s, this can be rewritten as

$$\frac{\dot{m} r_s^2}{r^2} = -\rho D_{ij} \frac{d\bar{C}_i}{dr} \left(\frac{1}{1 - \bar{C}_i} \right) \qquad (4\text{-}29)$$

Integration of this expression from the surface of the sphere to infinity yields

$$\dot{m} r_s = \rho D_{ij} \ln \left(\frac{1}{1 - \bar{C}_{i_s}} \right) \qquad (4\text{-}30)$$

for any element i whose net mass flux is not zero. For any element i whose net mass flux is zero the equation is

$$\overset{\circ}{m} r_s = \rho D_{ij} \ln\left(\frac{\bar{C}_{i_\infty}}{\bar{C}_{i_s}}\right) \tag{4-31}$$

Energy Equation

It is assumed that viscous dissipation, changes in potential and kinetic energy, and shear work are negligible. The gas mixture is assumed to be a perfect gas with no energy of mixing involved, and changes occur only in the radial direction. For a thin spherical shell of radius r and thickness Δr, applying the energy equation and taking limits as $\Delta r \to 0$ results in

$$\frac{\partial}{\partial r}\left(r^2 \frac{k}{C_p} \frac{\partial h}{\partial r}\right) = \frac{\partial}{\partial r}(r^2 n_r h) - \frac{\partial}{\partial r}\left[r^2 \sum_i h_i \frac{\partial C_i}{\partial r}(1 - \frac{1}{Le})\rho D_{ij}\right] \tag{4-32}$$

with the boundary conditions

$$r = r_s, \quad h = h_w$$

$$r \to \infty, \quad h = h_\infty$$

If the Lewis number is assumed equal to one equation (4-32) becomes

$$\frac{d}{dr}\left(r^2 \frac{k}{C_p} \frac{dh}{dr}\right) = \frac{d}{dr}(r^2 n_r h) \tag{4-33}$$

Assuming constant properties, integration yields

$$r^2 \frac{k}{C_p} \frac{dh}{dr} = r^2 n_r h + C_1 \tag{4-34}$$

where C_1 is an integration constant.

These variables may be separated and integrated again to yield

$$\frac{\mu}{Pr} \ln \left(h + \frac{C_1}{n_r r^2}\right) = -\frac{1}{r}(r^2 n_r) + C_2 \qquad (4\text{-}35)$$

where C_2 is a second integration constant.

The constants of integration as determined by the boundary conditions are

$$C_1 = (r_s^2 n_s)\left[\frac{e^{(\frac{Pr}{\mu} r_s n_s)} h_w - h_\infty}{1 - e^{(\frac{Pr}{\mu} r_s n_s)}}\right] \qquad (4\text{-}36)$$

$$C_2 = \frac{\mu}{Pr} \ln\left[h_\infty + \frac{e^{(\frac{Pr}{\mu} r_s n_s)} h_w - h_\infty}{1 - e^{(\frac{Pr}{\mu} r_s n_s)}}\right] \qquad (4\text{-}37)$$

The substitution of equations (4-36) and (4-37) into equation (4-35) and solving for the enthalpy yields

$$h = \frac{e^{\frac{Pr}{\mu} r_s n_s (1 - \frac{r n_r}{r_s n_s})}(h_w - h_\infty) - e^{\frac{Pr}{\mu} r_s n_s} h_w + h_\infty}{1 - e^{\frac{Pr}{\mu} r_s n_s}} \qquad (4\text{-}38)$$

Adiabatic Surface Condition. The following sketch illustrates an energy balance at the surface of a sphere:
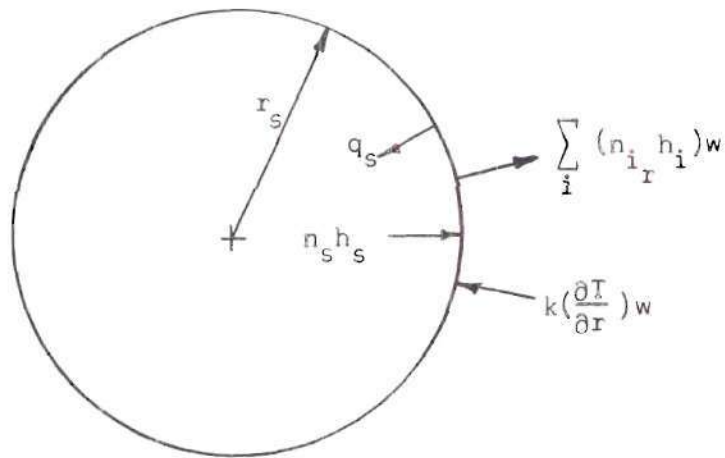
The energy balance may be written as

$$q_s + \sum_i (n_{i_r} h_i)_w = n_s h_s + k\left(\frac{\partial T}{\partial r}\right)_w \qquad (4\text{-}39)$$

The heat-conduction term may be written with gas mixture properties as

$$k\left(\frac{\partial T}{\partial r}\right)_w = \frac{k}{C_p}\left(\frac{\partial h}{\partial r}\right)_w - \frac{k}{C_p} \sum_i \left(h_i \frac{\partial C_i}{\partial r}\right) \qquad (4\text{-}40)$$

The diffusion equation multiplied by h_i, summed over all species and rearranged, may be written

$$\sum_i \left(h_i \frac{\partial C_i}{\partial r}\right) = n_s \frac{h_w}{\rho D_{ij}} - \frac{1}{\rho D_{ij}} \sum_i (n_{i_r} h_i)_w \qquad (4\text{-}41)$$

Substitution of equations (4-40) and (4-41) into equation (4-39) results in

$$q_s = n_s h_s + \frac{\mu}{Pr} \left(\frac{\partial h}{\partial r}\right)_w - \frac{n_s h_w}{Le} \tag{4-42}$$

$$+ \sum_1^r \left(n_i h_i\right)_w \left(\frac{1}{Le} - 1\right)$$

For Le = 1 this simplifies to

$$q_s = n_s h_s + \frac{\mu}{Pr} \left(\frac{\partial h}{\partial r}\right)_w - n_s h_w \tag{4-43}$$

The enthalpy gradient at the wall calculated from equation (4-38) is

$$\left(\frac{\partial h}{\partial r}\right)_w = n_s \frac{Pr}{\mu} \left[\frac{e^{\frac{Pr}{\mu} r_s n_s} h_w - n_\infty}{e^{\frac{Pr}{\mu} r_s n_s}} \right] \tag{4-44}$$

Using this, the energy balance may be written

$$q_s = n_s \left[h_s + \frac{e^{\frac{Pr}{\mu} r_s n_s} h_w - h_\infty}{1 - e^{\frac{Pr}{\mu} r_s n_s}} \right] \tag{4-45}$$

The adiabatic wall condition is

$$q_s = 0 \tag{4-46}$$

so that the adiabatic wall enthalpy is

$$h_s = \frac{n_\infty - e^{\frac{Pr}{\mu} r_s n_s} h_w}{1 - e^{\frac{Pr}{\mu} r_s n_s}} \tag{4-47}$$

Concentrations at the Surface

In order to simplify the numerical calculations an approximation of the surface concentrations was made. It was assumed that no elemental or molecular oxygen was present at the surface and that the equilibrium partial pressure of aluminum at the surface corresponded to the vapor pressure of aluminum at the particle temperature. The accuracy of these assumptions was checked by the complete flame structure calculations performed later.

Under these conditions the element mass fractions at the surface are

$$\bar{C}_O = \frac{M_O}{M_{AlO}} C_{AlO} + \frac{M_O}{M_{Al_2O}} C_{Al_2O} + \frac{2M_O}{M_{Al_2O_2}} C_{Al_2O_2} \tag{4-48}$$

$$\bar{C}_{Al} = C_{Al} + \frac{M_{Al}}{M_{AlO}} C_{AlO} + \frac{2M_{Al}}{M_{Al_2O}} C_{Al_2O} + \frac{2M_{Al}}{M_{Al_2O_2}} C_{Al_2O_2} \tag{4-49}$$

$$\bar{C}_N = C_{N_2} \tag{4-50}$$

Inserting these into the two diffusion equations (4-30) and (4-31), simplifying, and substituting

$$C_i = \frac{P_i M_i}{\sum P_i M_i} \tag{4-51}$$

yields

$$P_{N_2} = \frac{CM_O}{M_{N_2}} \left[P_{AlO} + P_{Al_2O} + P_{Al_2O_2} \right] \tag{4-52}$$

where

     C = ratio of nitrogen to oxygen in the ambient environment.

The chemical reactions considered in this case are

$$Al\ (liquid) \xrightleftharpoons{K_1} Al\ (gas) \qquad [A]$$

$$Al\ (gas) + \frac{1}{2} O_2 \xrightleftharpoons{K_2} AlO \qquad [B]$$

$$2Al\ (gas) + \frac{1}{2} O_2 \xrightleftharpoons{K_3} Al_2O \qquad [C]$$

$$2Al\ (gas) + O_2 \xrightleftharpoons{K_4} Al_2O_2 \qquad [D]$$

The final equation necessary to determine the surface concentrations is

$$\sum_i P_i = P \qquad (4\text{-}53)$$

The equilibrium constants for the reactions [A] - [D] written in terms of partial pressures can be manipulated to yield

$$P_{Al_2O} = \frac{K_1 K_3}{K_2} P_{AlO} \qquad (4\text{-}54)$$

$$P_{Al_2O_2} = \frac{K_4}{K_2^2} P_{AlO}^2 \qquad (4\text{-}55)$$

Also, equation (4-52) can be combined with the equilibrium constants to yield

$$P_{A10} = - \frac{\left[\frac{K_1 K_2 K_3}{2K_4} + \frac{K_2^2}{2K_4} \right]}{2}$$

(4-56)

$$+ \sqrt{ \frac{\left[\frac{K_1 K_2 K_3}{2K_4} + \frac{K_2^2}{2K_4} \right]^2}{4} + \frac{K_2^2}{2K_4} \frac{M_{N_2}}{CM_0} P_{N_2} }$$

Equations (4-54) and (4-55) can be substituted into equation (4-53) and arranged to yield

$$P_{A10} = - \left[\frac{K_2 [K_2 + K_1 K_3]}{2K_4} \right]$$

(4-57)

$$+ \frac{K_2}{K_4} \sqrt{ \left[\frac{K_2 + K_1 K_3}{2} \right]^2 + K_4 [1 - K_1 - P_{N_2}] }$$

An order of magnitude check of the terms within the radicals of the last two equations showed that over the temperature range of interest the binomial theorem could be used to simplify the solution of the equations. Neglecting higher order terms the solution for the partial pressure of nitrogen at the surface is

$$P_{N_2} = \frac{1 - K_1}{1 + \frac{M_{N_2}}{CM_0}}$$

(4-58)

The surface conditions are determined by selecting the temperature which matches the enthalpy calculated from

$$h = \sum_i C_i h_i \qquad (4\text{-}59)$$

and the enthalpy given by equation (4-47). It should be noted that

$$\frac{r_s n_s}{\rho D_{ij}} = \ln\left(\frac{\bar{C}_{N_\infty}}{\bar{C}_{N_s}}\right) \qquad (4\text{-}60)$$

and since we are assuming that Le = 1

$$\frac{r_s n_s}{\rho D_{ij}} = \frac{Pr}{\mu} r_s n_s \qquad (4\text{-}61)$$

Flame Structure

The numerical computations for the concentration profiles and temperature profile were carried out on a Burroughs 5500 digital computer. The reactions $[A] - [D]$, page , and the reaction

$$\tfrac{1}{2} O_2 \xrightleftharpoons{K_5} O \qquad [E]$$

were considered in these computations. The technique used in these computations was to start at a position far from the surface and assume an appropriate temperature. The five equilibrium constants were calculated from data of reference (58). These constants expressed in terms of partial pressures, the diffusion equation and Dalton's Law completely determined the concentrations at the assumed temperature. The enthalpy of the mixture was calculated from equation (4-59). The position, $\frac{r_s}{r}$,

corresponding to these concentrations, was calculated from the diffusion equation integrated from the surface to a position $\frac{r_s}{r}$. This value was substituted into the general expression for the enthalpy distribution, equation (4-38), and a value for the enthalpy determined. Iteration on concentrations was carried out by means of a standard pattern search technique, reference (59), until the two enthalpies were equal. This was a solution for the assumed temperature and the position, $\frac{r_s}{r}$, was given by the integrated diffusion equation.

This procedure was repeated stepwise for a higher temperature and the iteration started from the last solution. When the assumed temperature exceeded the maximum for the temperature profile no solution could be obtained. At this point the temperature was decreased, step-wise, and the procedure repeated. In this fashion the entire flame structure was calculated, starting at a position far from the sphere and proceeding to the surface in increments of $\frac{r_s}{r}$.

The results of these computations are given in Figure 11, page 57. The concentrations of elemental oxygen and AlO were small throughout the flame structure. The validity of the earlier assumptions in neglecting oxygen at the surface to simplify calculation of the surface concentrations is supported by these results.

Criterion for Al_2O_3 (liquid) Formation

The problem was to determine for a given gas composition in equilibrium at a fixed pressure and temperature whether or not the formation of Al_2O_3 (liquid) would cause a reduction in free energy at the same temperature and pressure. The gas mixture consists of n_i moles of N_2,
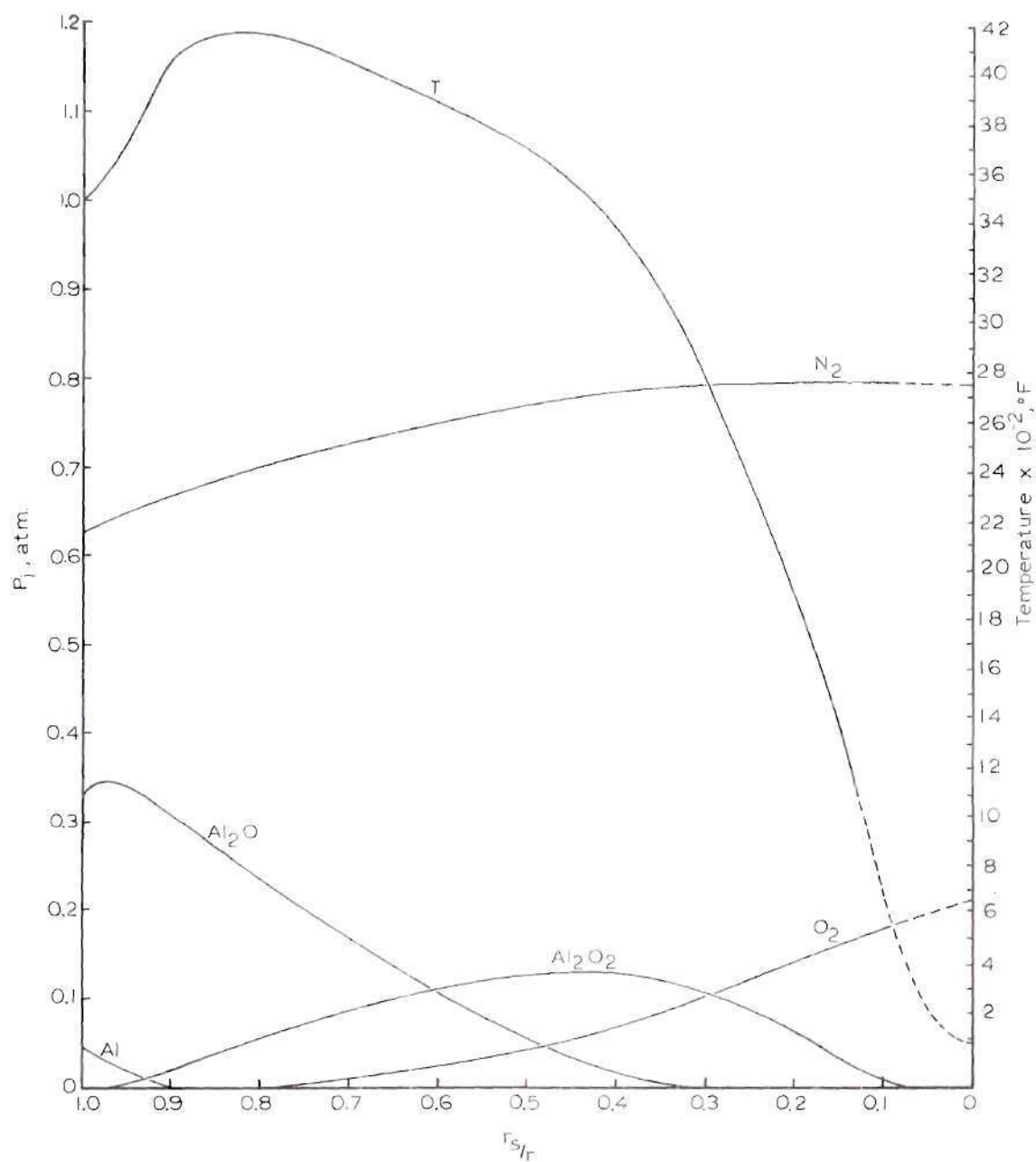
Figure 11. Flame Structure–Aluminum Particle Burning in Air, $T_\infty = 77°F$.

O_2, O, Al, AlO, Al_2O and Al_2O_2. Although the following represents a standard approach to predicting the formation of a chemical species this appears to be the first time it has been applied to aluminum combustion in predicting condensation.

One possible variation at the same pressure and temperature is

$$2 \text{ Al (gas)} + 3/2 \text{ } O_2 \text{ (gas)} \xrightleftharpoons{K_p} Al_2O_3 \text{ (liquid)} \quad [F]$$
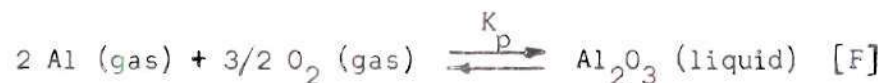
If

$$\Delta n = \text{moles of } Al_2O_3 \text{ (liquid) formed}$$

then the new concentration values, denoted by primes, for the other species are

$$n'_{O_2} = n_{O_2} - \frac{3}{2} \Delta n \qquad (4\text{-}62)$$

$$n'_{Al_2O_2} = n_{Al_2O_2} \qquad (4\text{-}63)$$

$$n'_{Al} = n_{Al} - 2\Delta n \qquad (4\text{-}64)$$

$$n'_{AlO} = n_{AlO} \qquad (4\text{-}65)$$

The free energy may be written as

$$\Delta F = \Delta F^o_f + RT \ln P \qquad (4\text{-}66)$$

or

$$\Delta F = \Delta n \Delta F^o_{f_{Al_2O_3}(liquid)} - \frac{3}{2} \Delta n \Delta F^o_{f_{O_2}} - 2\Delta n \Delta F^o_{f_{Al}} \qquad (4\text{-}67)$$

$$- n_{O2} \, RT \, \ln \frac{P_{O_2}}{P'_{O_2}} - \frac{3}{2} \Delta n \, RT \, \ln P'_{O_2}$$

$$- n_{Al_2O_2} \, RT \, \ln \frac{P_{Al_2O_2}}{P'_{Al_2O_2}} - 2\Delta n \, RT \, \ln P'_{Al}$$

$$- n_{Al} \, RT \, \ln \frac{P_{Al}}{P'_{Al}} - n_{AlO} \, RT \, \ln \frac{P_{AlO}}{P'_{AlO}}$$

Dividing by Δn and taking the limit as $\Delta n \to 0$ results in

$$\frac{dF}{dn} = \Delta F^o_{f_{Al_2O_3}(liquid)} - \frac{3}{2} \left[\Delta F^o_{f_{O_2}} + RT \, \ln P_{O_2} \right] \qquad (4\text{-}68)$$

$$- 2\left[\Delta F^o_{f_{Al}} + RT \, \ln P_{Al} \right]$$

or

$$\frac{dF}{dn} = -2.303 \, RT \left[\log K_{P_{Al_2O_3}(liquid)} - \frac{3}{2} \log K_{P_{O_2}} \right. \qquad (4\text{-}69)$$

$$\left. - 2 \log K_{P_{Al}} + \log\left(P_{O_2}^{\frac{3}{2}} P_{Al}^2\right) \right]$$

Thus

$$\frac{dF}{dn} = - 2.303 \ RT \ \log \left[\frac{K_p}{\frac{1}{P_{O_2}^{3/2} \ P_{Al}^2}} \right] \qquad (4-70)$$

From a thermodynamics standpoint, if

$$\frac{dF}{dn} < 0$$

it is possible for Al_2O_3 (liquid) to form. Thus, if

$$K_p < \frac{1}{P_{O_2}^{3/2} \ P_{Al}^2}$$

the condensed phase will not form by the reaction considered. However, it can be shown that Al_2O_3 (liquid) formed from any of the possible species considered here results in the same criterion and consequently, the result is quite general.

CHAPTER V

EXPERIMENTAL PROCEDURE AND RESULTS

The procedures used in this investigation for the determination of velocities or dynamic pressure, temperatures, concentrations and particle distributions are presented in this section in the order listed. A description of the instrumentation and the techniques used to obtain the temperature measurements were presented in Chapter III entitled Instrumentation and Experimental Apparatus.

Velocity Measurements

A small water cooled probe was used to measure the differences in stagnation pressure and static pressure at the chamber wall. The design and construction of this probe has been described earlier in Chapter III, page 16. The turbulent mixing and chemically reacting regions of the flow were of primary interest in this study and consequently, the accompanying high temperatures required the use of water cooled probes.

It was found to be impractical to use this probe in the flow with the entrained aluminum particles. In every test in which the cooled probe was used with aluminum particles, it eventually became covered and plugged with particles and metal oxide. Without the entrained aluminum particles, water condensed on the probe and in several tests covered the pressure port affecting the readings. To prevent water from condensing on the probe, the cooling water flow was

gradually reduced in an effort to raise the surface temperature of the probe. Although this was accomplished, it was found to be impractical due to the high heating rates encountered in some regions of the flame. Small fluctuations in coolant flow resulted in sudden and severe heating of the probe. When this occurred the fuel flow was stopped immediately to prevent severe damage to the probe. The overheating in some cases melted some of the silver solder used in fabricating the probe.

A second method was tried to prevent condensation of water on the probe which proved to be satisfactory. This technique involved using the maximum flow of cooling water at all times, and preheating the water to approximately 140°F before circulating it through the probe. This allowed the surface temperature of the probe to be maintained high enough to prevent condensation but without the danger of suddenly over-heating a part of the probe. This technique was used in all tests in which the probe was placed in the flame, including the species sampling tests performed later.

Test Setup and Calibration

The probe was mounted on the tracking mechanism so that the probe tip pointed downward. Mounted in this fashion, the probe measured the stagnation pressure. The tracking mechanism permitted the probe to be moved vertically or horizontally. The alignment of the probe with the flow was checked after installation of the probe by measuring the horizontal distance from a vertical rod, one end of which slipped inside the fuel nozzle, and the probe tip at different heights. The rod was removed after this alignment check prior to performing the tests.

It was assumed that the pressure difference as measured by the

probe was the dynamic pressure at the probe tip location. Due to the high temperatures in the flame, it was not practical to attempt a direct velocity calibration of the probe. The velocities were calculated from the pressure measurements and values of local densities determined from chemical composition and temperature data.

The stagnation pressure measuring setup was calibrated with a Trimount Instrument Company micromanometer filled with n-butyl alcohol. The pressure was measured with two Magnehelix gauges with ranges of 0 - 0.5 and 0 - 5.0 inches of H_2O. The micromanometer produced pressure readings which were reproducible with this experimental setup to within 0.005 inches of n-butyl alcohol. The system was pressure checked and recalibrated before each series of measurements and one point rerun after completing each of the tests. Prior to performing each series of tests, the entire system was carefully checked for leaks by applying a soap-water mixture to all connections while operating the air blower at maximum flow.

The pressure gradient in the direction of flow was measured to determine if several wall taps would be necessary for measuring the velocity head at various heights in the flow. These measurements were made using the micromanometer for two different cases, with air flow only and with the hydrogen flame. In the first case, the measured gradient in the direction of flow was -0.0031 inches of n-butyl alcohol per foot and in the second case -0.0077 inches of n-butyl alcohol per foot. These values were low enough to neglect the drop in static pressure in the axial direction. A single wall tap was used for all dynamic pressure tests.

ΔP Measurements

Several initial profiles at different heights were obtained with air flow only to determine whether or not the flow was reasonably symmetric and constant over most of the area. A plot of the initial test data showed that the small hydrogen nozzle located above the screen section and in the center of the duct had a significant effect on the flow. This effect was observed at 12 inches (h/d = 96) downstream of the nozzle. This effect is shown in Figure 12, page 65, which gives the initial ΔP profiles measured at two different heights.

This effect could not be completely eliminated with air flow only, but it was greatly reduced by extending the air duct upward 6 inches so that the hydrogen nozzle exit and the air duct exit were at the same height and by placing a stainless steel screen across the air duct at the nozzle exit. A small hole was cut in the center of the screen to permit the tip of the nozzle to pass through it. This modification reduced the influence of the hydrogen nozzle on the velocity profile. Figure 13, page 66, gives the ΔP measurements with air flow only with the duct extension and additional screen modifications. Based on this data it was apparent that with flow in the fuel nozzle the air velocity profile at the hydrogen nozzle exit was fairly flat. The flow with combustion involved highly turbulent fluctuations and it was felt that further attempts to smooth the air flow were not warranted. The data plotted in Figures 12 and 13, pages 65 and 66, plus ΔP data on six additional profiles for these two cases are given in Appendix A, page 159.

The air jet flow setting was fixed at the conditions corresponding
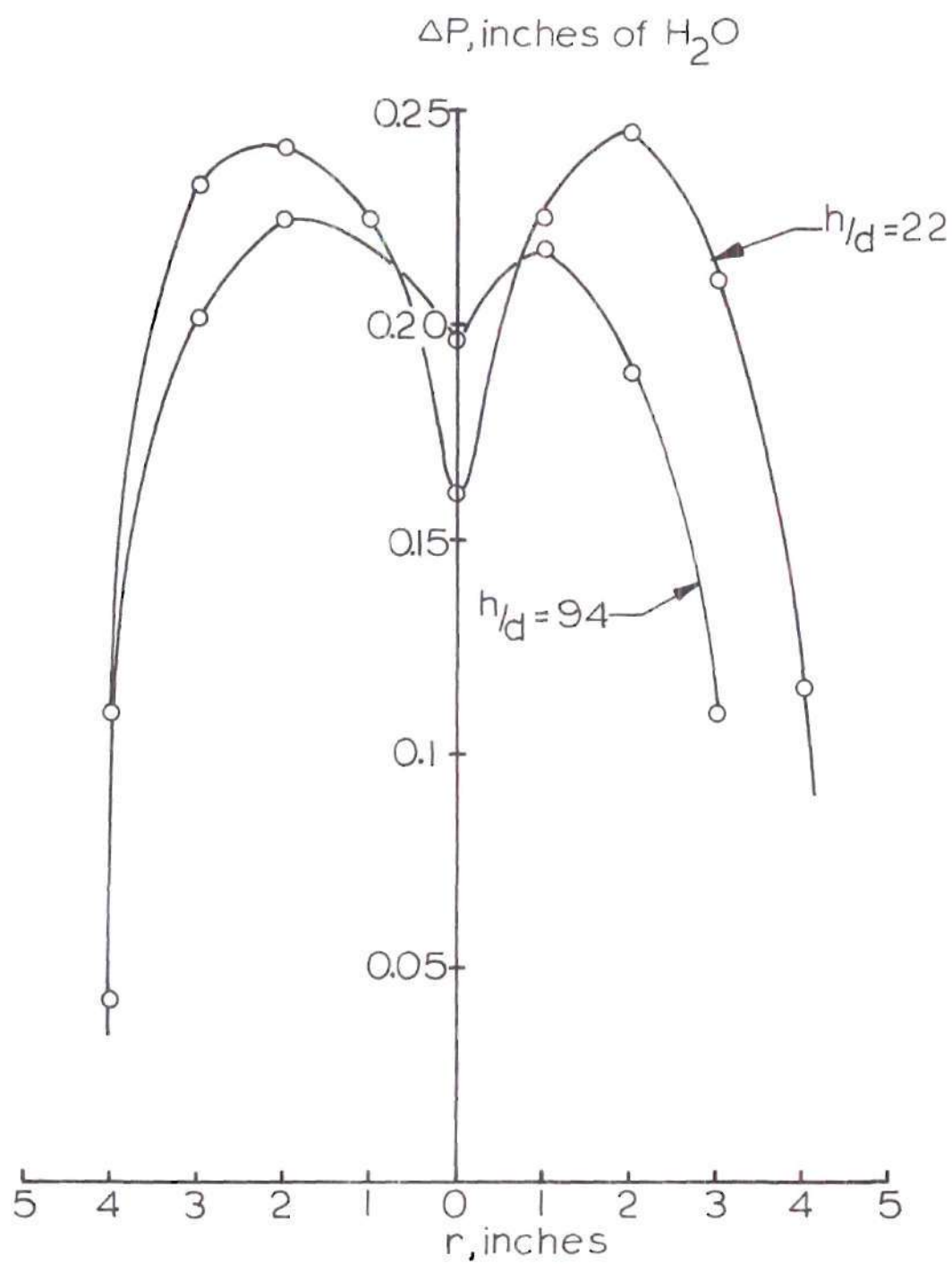
Figure 12. Dynamic Pressure Measurements with Air Only.
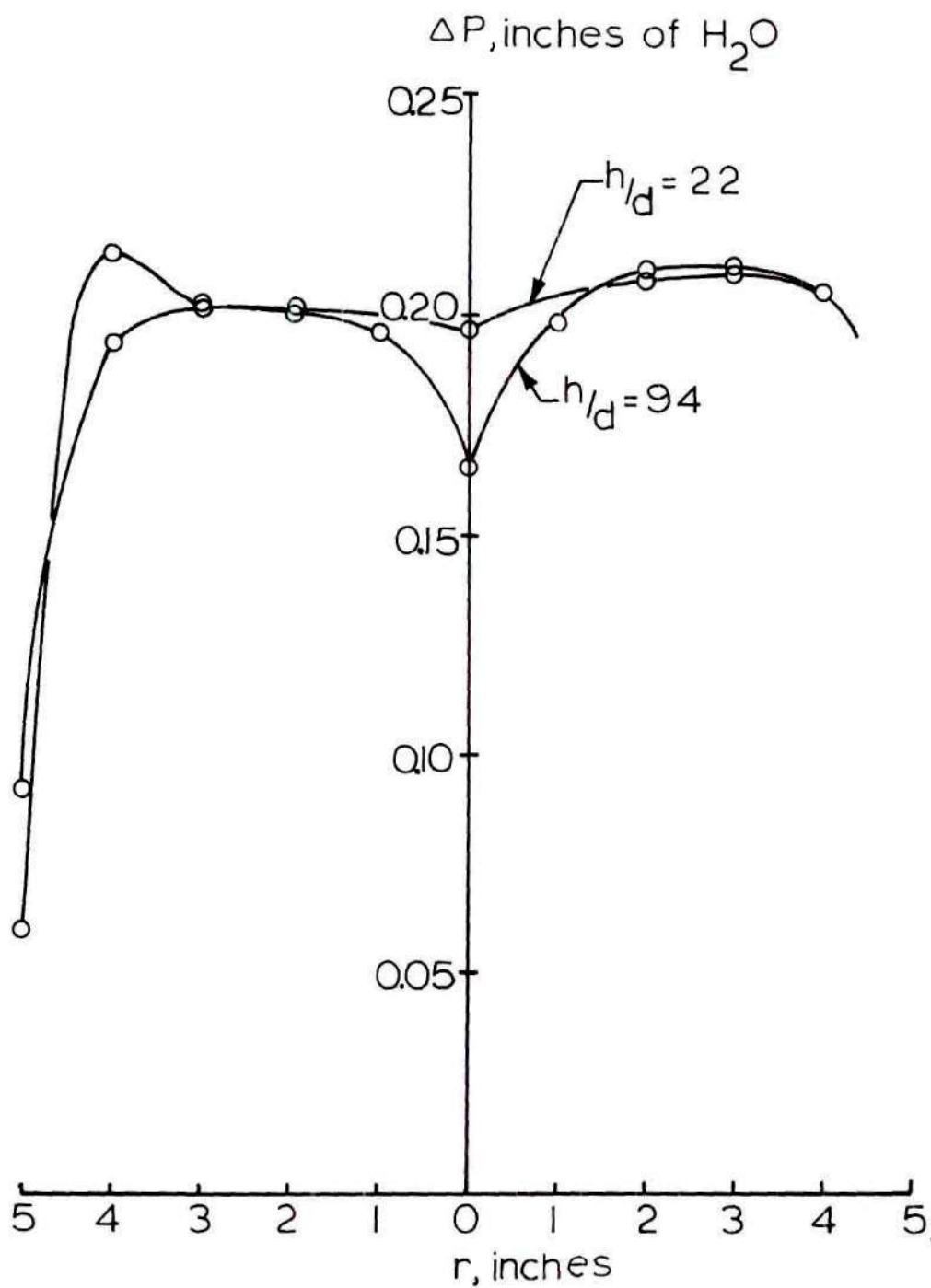
Figure 13. Dynamic Pressure Measurements with Air Only with Duct Extension and Screen.

to the dynamic pressure distribution shown in Figure 13, page 66, for all subsequent testing. This was done to limit the number of parameters to be experimentally studied due to the complexity of the overall test program and to the difficulties involved in obtaining experimental data in the flame environment.

The variation of the velocity head along the centerline was measured for four different values of injection velocity of the fuel jet. These were 550, 406, 326, and 250 ft/sec. These data are plotted in Figure 14, page 68 and given in tabulation form in Appendix A, page 160. The ΔP for the nozzle exit position for each of the four cases was calculated from the flow measurement of hydrogen and the nozzle area. At axial positions less than approximately 0.6 inches from the nozzle, the probe diameter was approximately the size of the fuel jet. Consequently, no measurements were made with the probe at axial positions less than this value.

One additional traverse was made with the probe at a height of 2.75 (h/d = 22) inches from the nozzle exit. The exit velocity of the fuel jet was 550 ft/sec for this case. The measured dynamic pressure is given in Figure 15, page 69 with the corresponding velocity distribution calculated from chemical composition and temperature data for this location. Numerical data are presented in tabular form in Appendix A, page 160. The dip in the dynamic pressure profile is due to the low density in that region.

Temperature Measurements

Measurements of temperature were obtained on the hydrogen-air
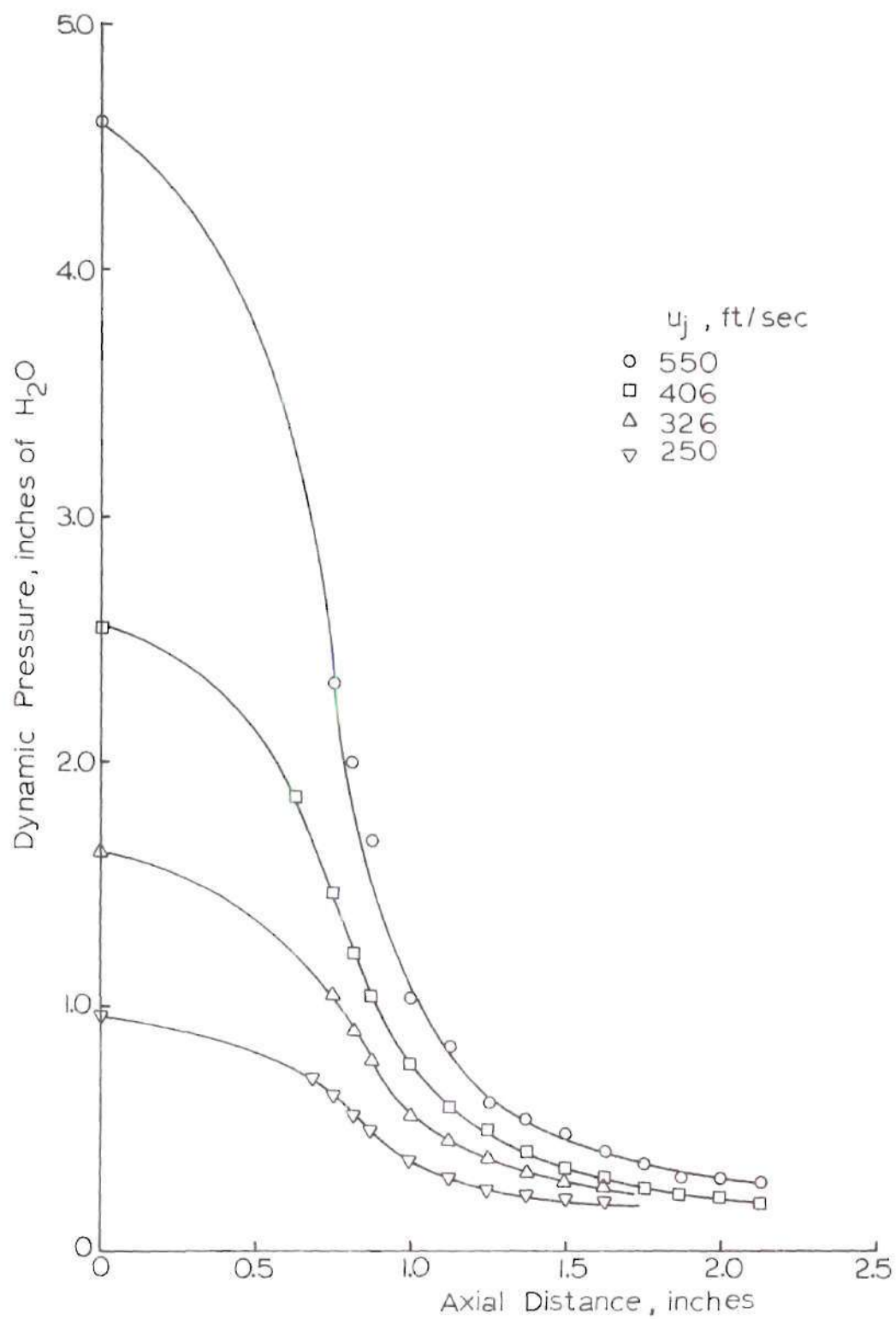
Figure 14. Centerline Dynamic Pressure
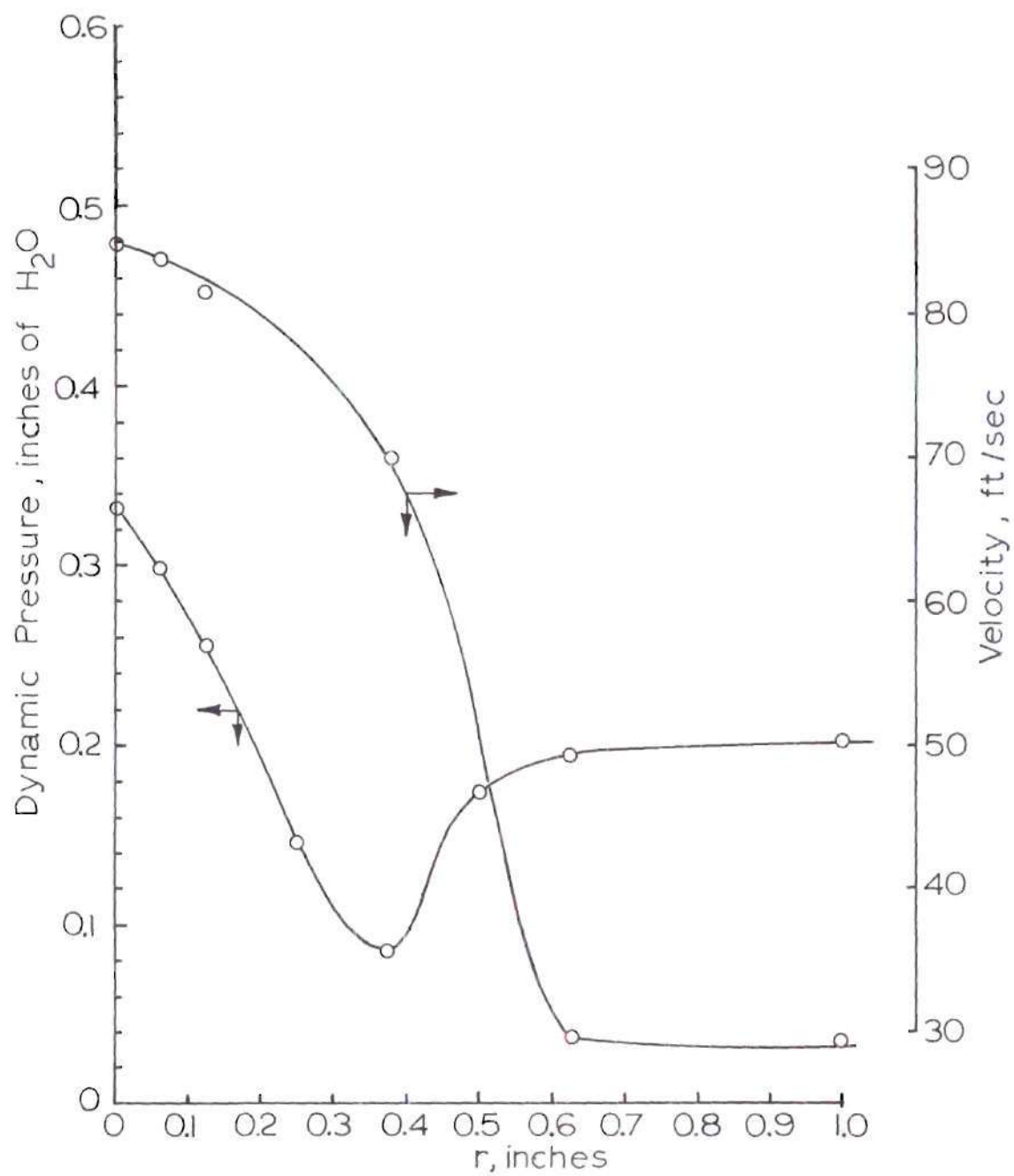
Figure 15. Velocity Profile at h/d = 22, u_j = 550 ft/sec.

diffusion flame by two different techniques and corrections applied for chemical species variations, velocity and thermal radiation. The theoretical flame sheet temperature for a hydrogen-air diffusion flame was calculated to be 4109°F. The maximum temperature of the diffusion flame considering dissociation was calculated to be 3830°F. These values are for an adiabatic flame and, consequently, represent the maximum temperature which could be encountered. The temperature gradients in the reacting region were very steep and in some cases resulted in the probe reading a lower value than the expected peak temperature.

Steady-State Temperature Data

A 1/16 inch diameter sheathed thermocouple probe with a hemispherical shaped tip, constructed as illustrated in Figure 3, page 19, was used to obtain a series of temperature profiles in the hydrogen-air flame. The probe was mounted on a support which was attached to the tracking mechanism. Measurements across the jets were performed with the probe in position 1 as shown in Figure 3, page 19, for values of h/d of 22, 30, 38, 54, 70, 86, 94 and 102. These data are presented in Figures 16 through 23, pages 71 through 78. The average temperatures are plotted with a vertical line at each point indicating the maximum and minimum readings.

A second profile was obtained with the probe oriented in position 2 for h/d = 22. These data are shown in Figure 16, page 71. The heat-transfer coefficient for the position 2 flow was calculated from concentration data and velocity data for h/d = 22 and by using the mixture rules as given by Mason and Saxena (60). These data and a probe emissivity of 0.8 were used to calculate T_g. These data are also plotted
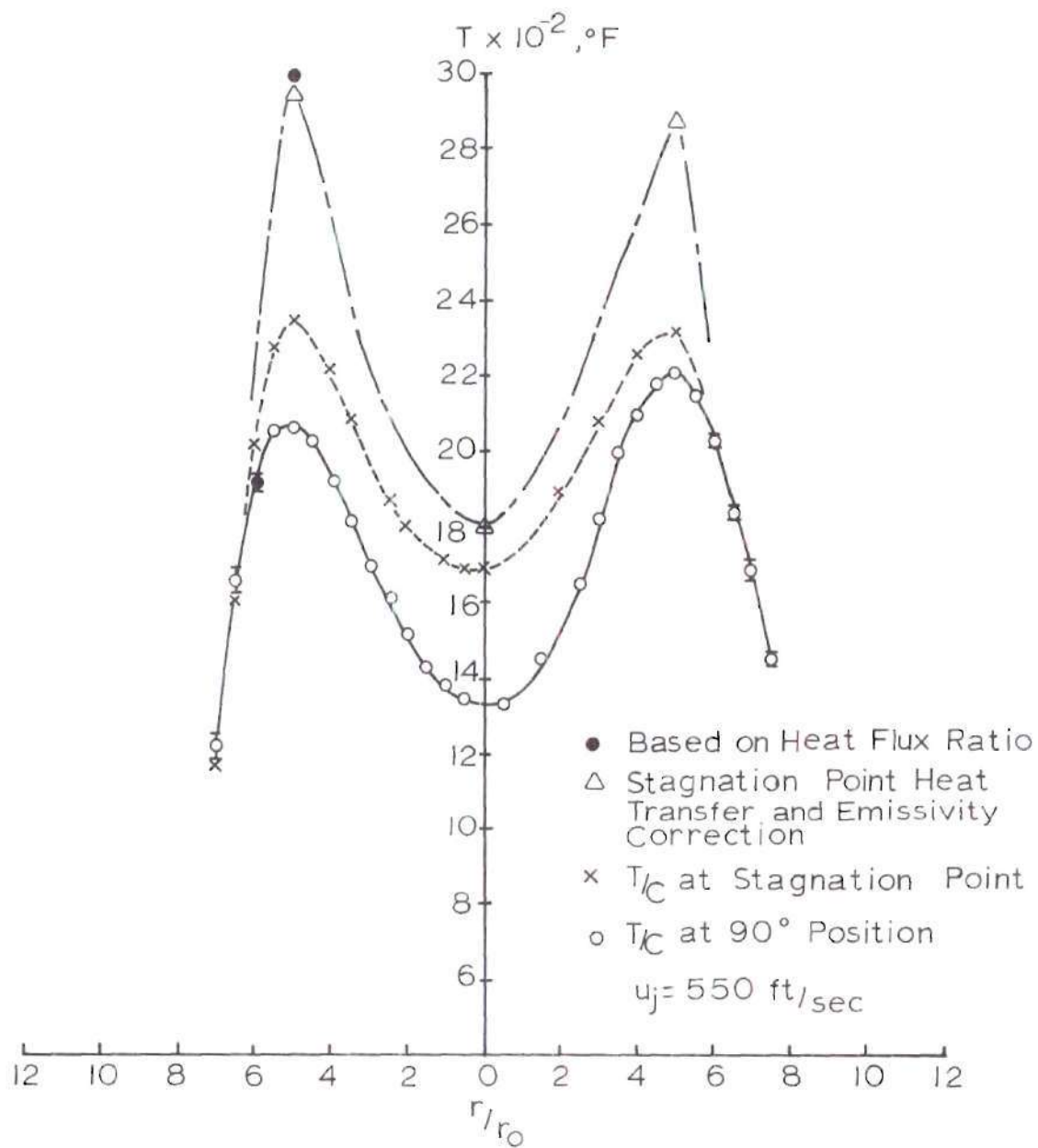
Figure 16. Temperature Profile at h/d = 22
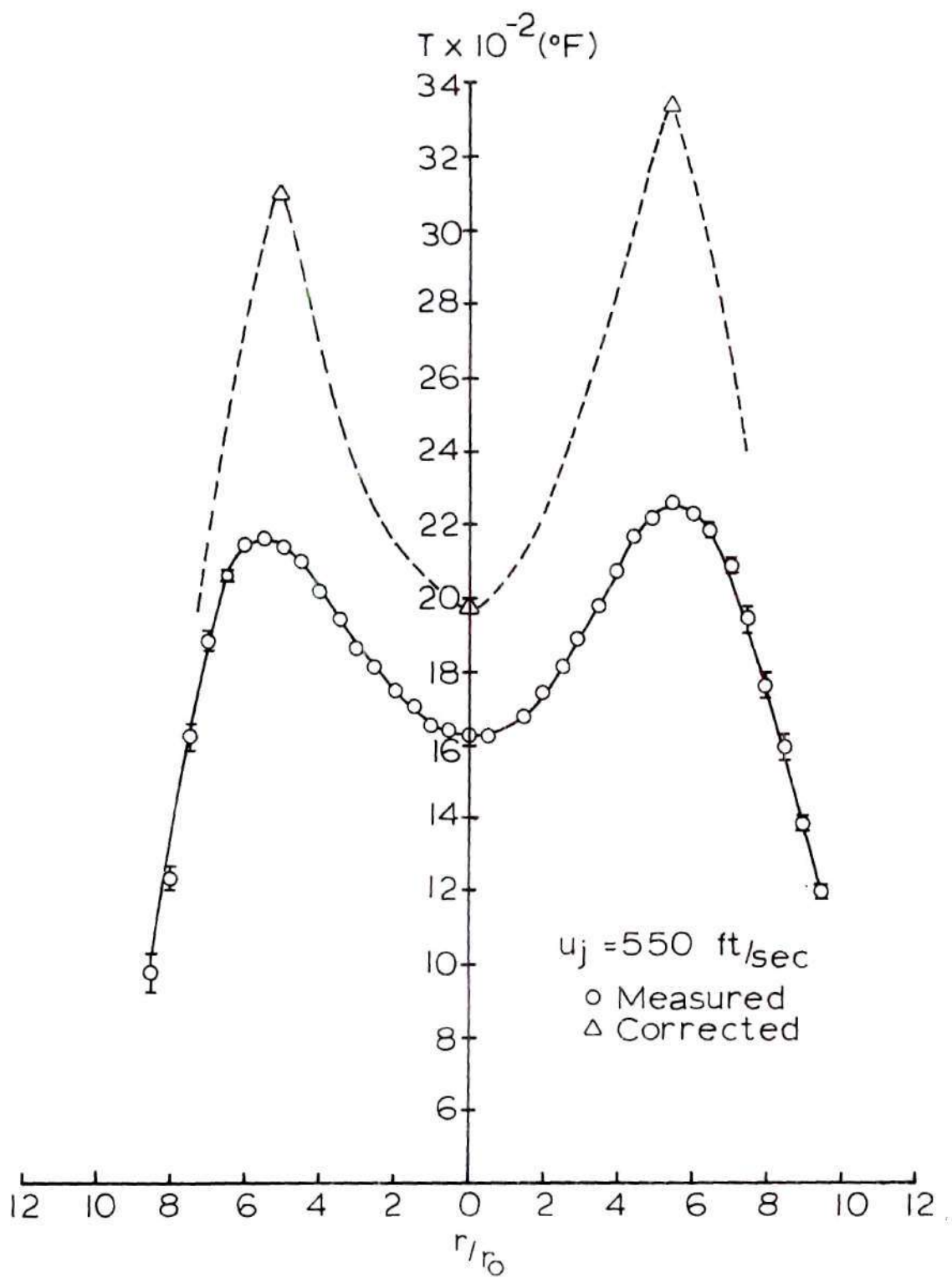
Figure 17. Temperature Profile at h/d = 30.

73
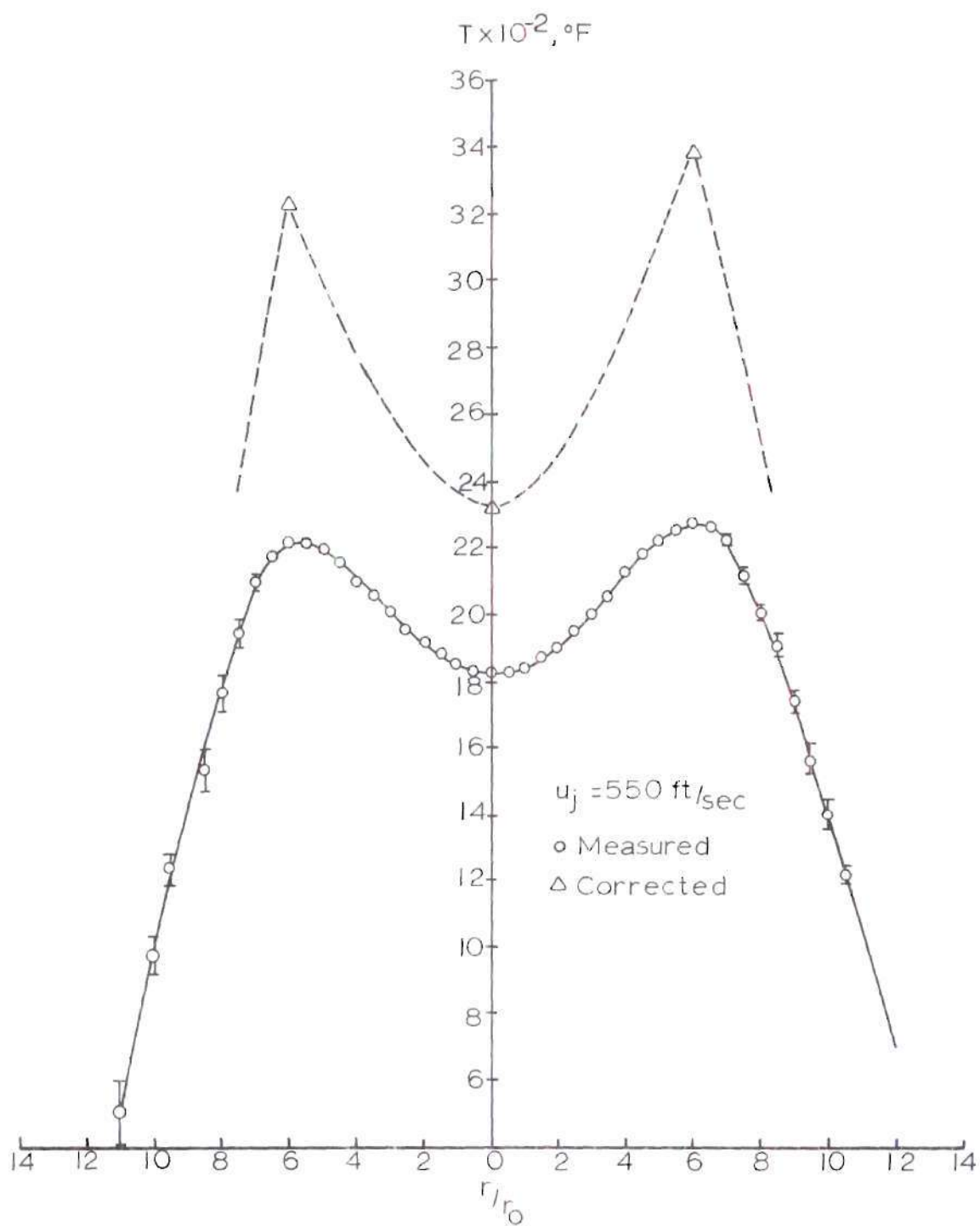
Figure 18. Temperature Profile at h/d = 38
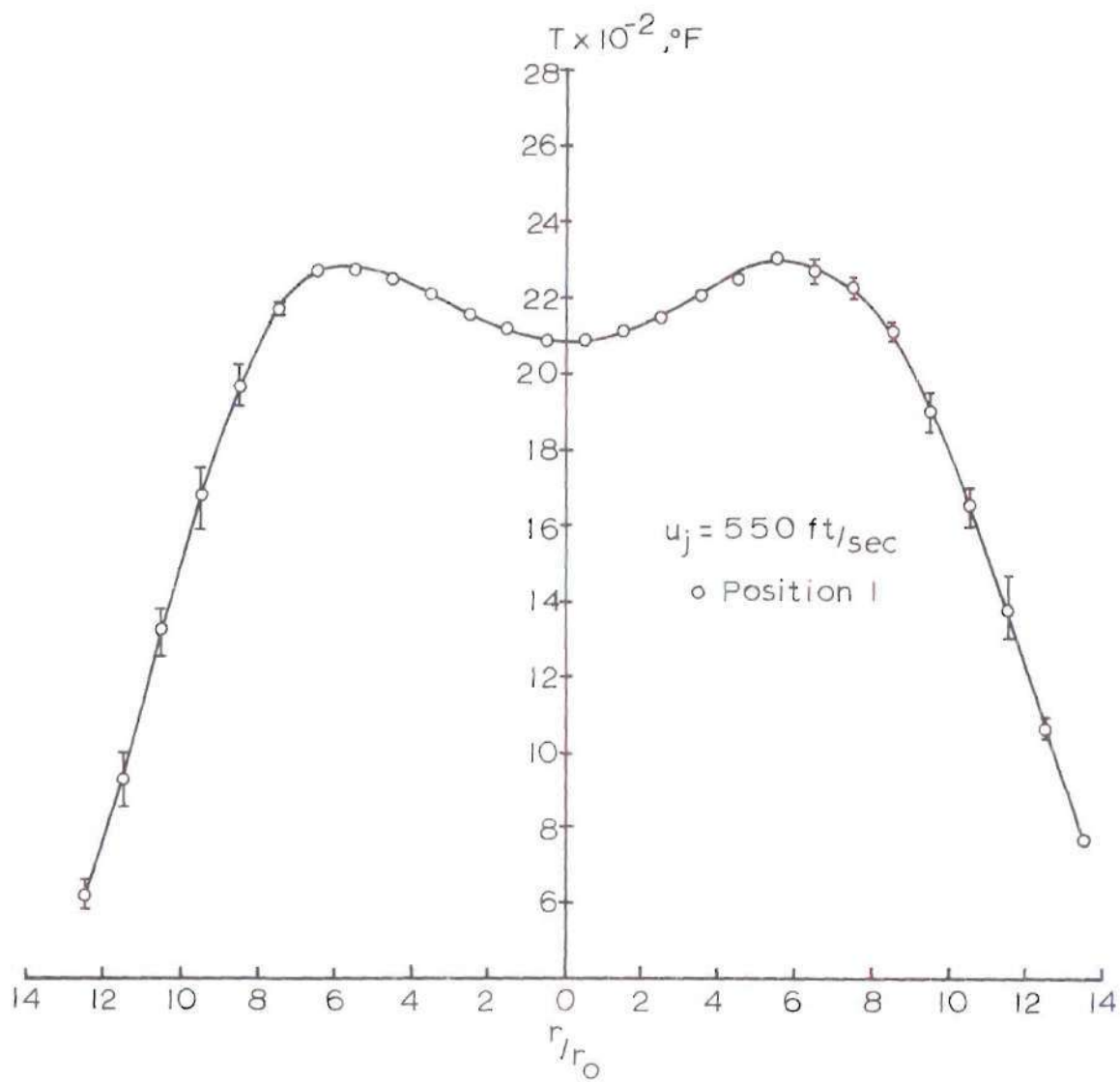
Figure 19. Temperature Profile at h/d = 54
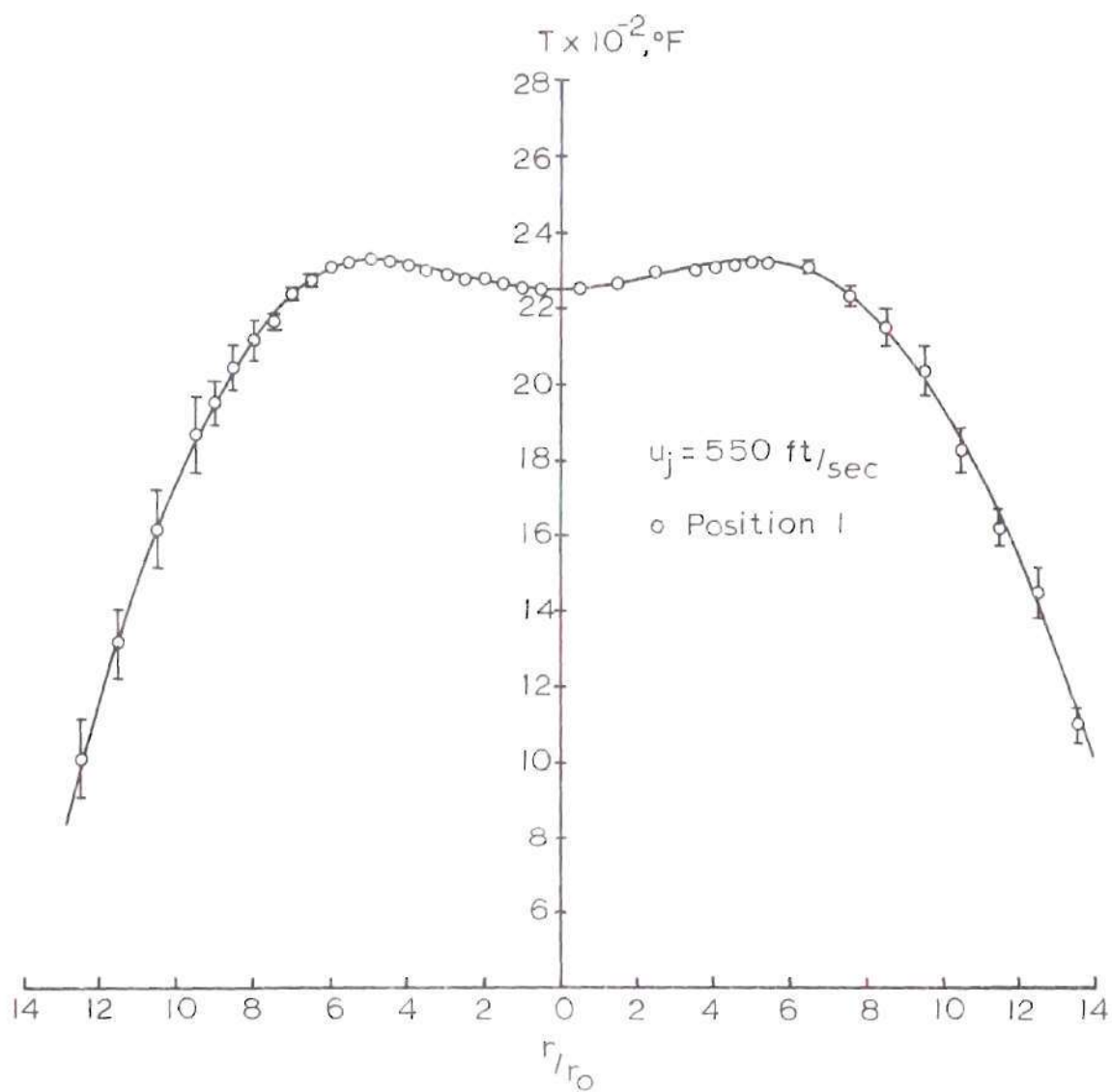
Figure 20. Temperature Profile at h/d = 70
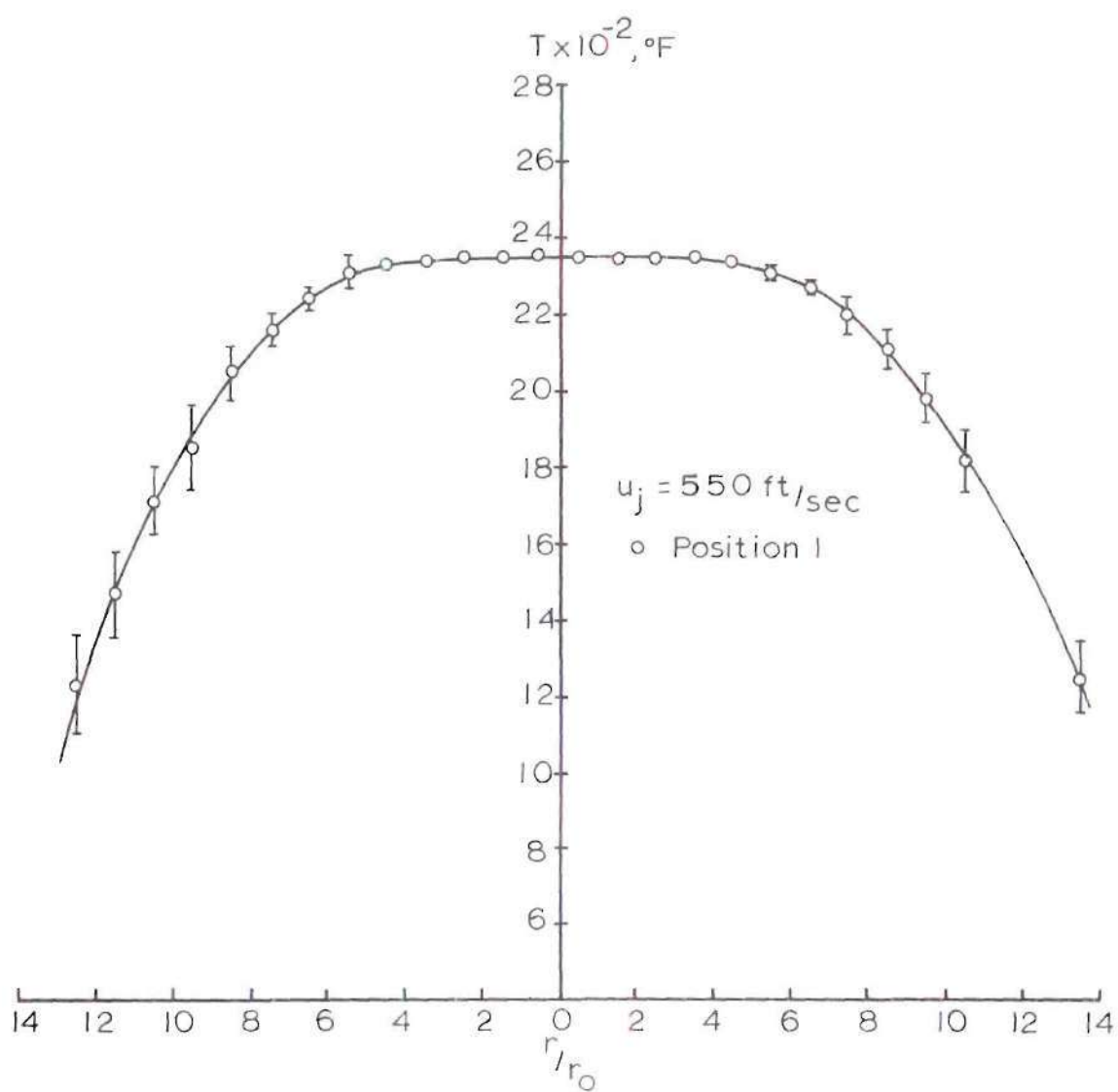
Figure 21. Temperature Profile at h/d = 86
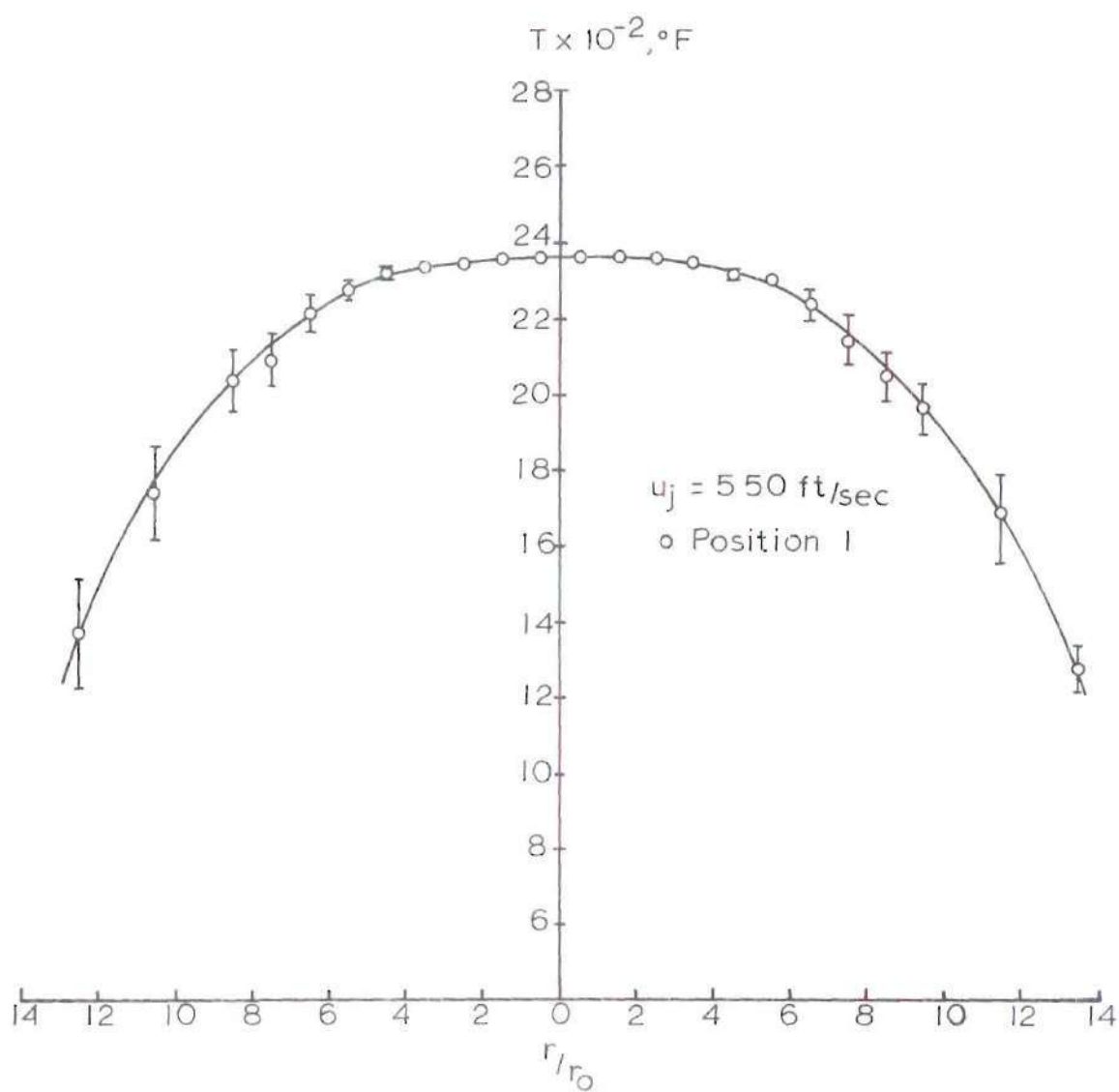
Figure 22. Temperature Profile at h/d = 94.
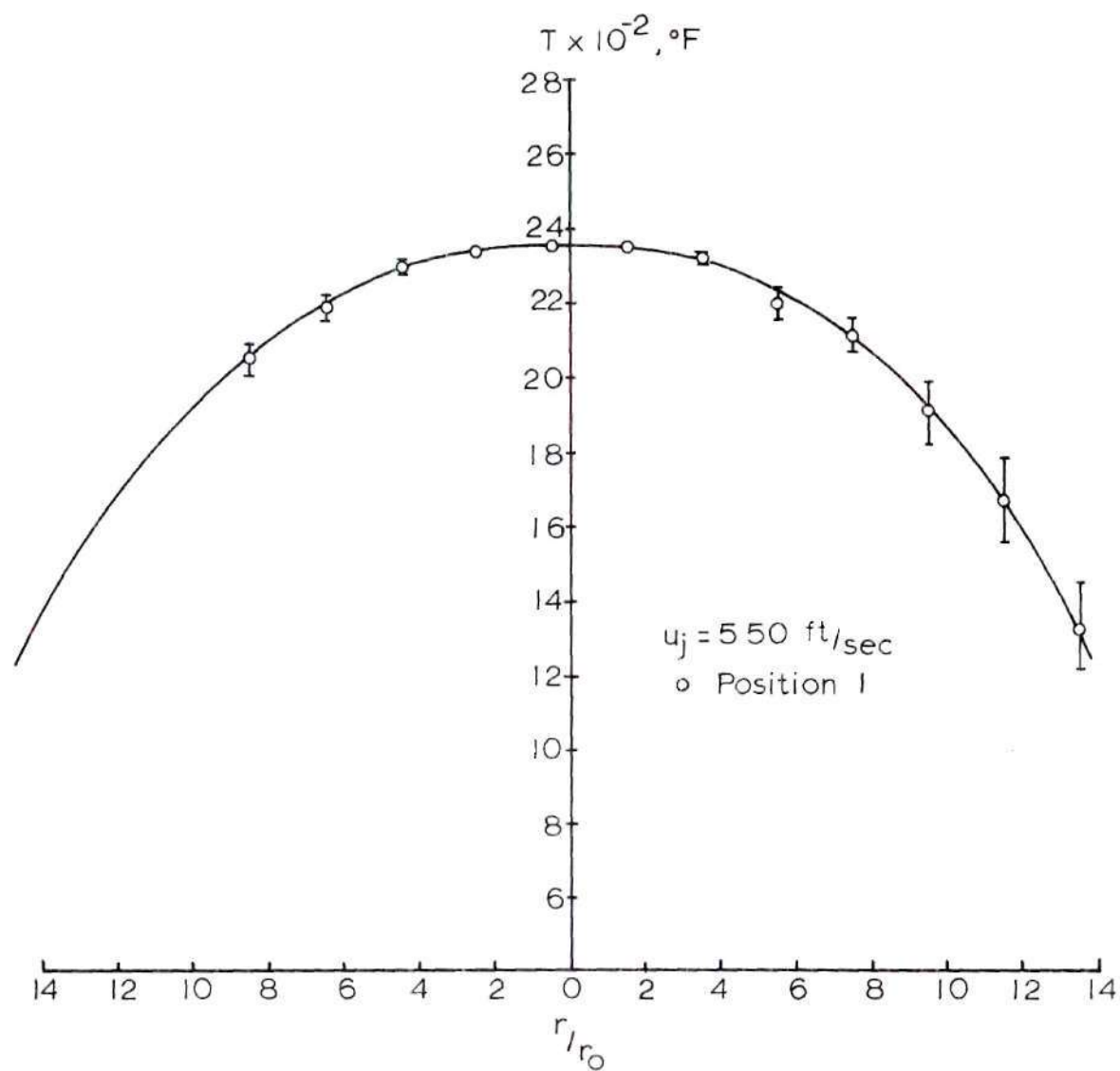
Figure 23. Temperature Profile at h/d = 102

in Figure 16, page 71. The peak temperature predicted from equation
(3-12), the heat flux ratio technique, using the probe position 1 and
2 data is also given in Figure 16, page 71.

It appeared from these measurements that separation may have
occurred on the probe in the position 1 orientation at the position in
the flow of maximum velocity, the centerline position at $h/d = 22$. This
would account for the low values obtained at the centerline at this
axial position. Similarly, the high reading on the second peak of
the profile for the position 1 orientation may be due to a transition
to turbulent flow. However, it is pointed out that the effects of an
oscillating free stream and the combustion processes on the boundary
layer development on the probe cannot be predicted.

Pulsed Thermocouple Data

The pulsed thermocouple was mounted on the positioning device
and positioned in the flow so that the thermocouple junction was located
at the highest temperature region. The coolant flow was intermittently
interrupted and the transient response of the thermocouple recorded on
an oscilloscope.

An energy balance for the thermocouple can be written as

$$\bar{h} \frac{A}{\ell} (T_g - T) = \frac{m}{\ell} C_p \frac{dT}{dt} \qquad (5-1)$$

If $(\dfrac{mC_p}{\bar{h}A})$ is a function of T_g only then

$$T_g = \frac{T e^{\frac{\bar{h}A}{mC_p}t} - T_i}{e^{\frac{\bar{h}A}{mC_p}t} - 1} \qquad (5-2)$$

where

T_g = gas temperature

T_i = initial temperature of T/C

T = temperature of T/C at time t

$\bar{h}$ = average heat transfer coefficient for thermocouple

t = time

m/ℓ = mass per unit length of T/C

A/ℓ = surface area per unit length of T/C

As shown in Table VIII, Appendix C, page 166, the heat-transfer coefficient is a function of T_g so that a trial and error process was required to solve for the gas temperature using pulsed thermocouple measurements. The solution was obtained for the region corresponding to an excess air-mixture ratio.

Figure 24, page 81, shows a typical oscillograph trace of one cycle of the pulsed thermocouple with the junction located in the maximum temperature region. The temperature-time curve for this oscillograph trace is given in Figure 25, page 82. The following values were used in equation (5-2)

$$C_p = 0.11 \ \frac{BTU}{lbm^{\circ}F}$$

$$m/\ell = 4.78 \times 10^{-4} \ lb/ft$$

$$A/\ell = 3.299 \times 10^{-3} \ ft$$

The calculations were performed for t = 0.3 sec and the result was

$$T_g = 3480^{\circ}F$$
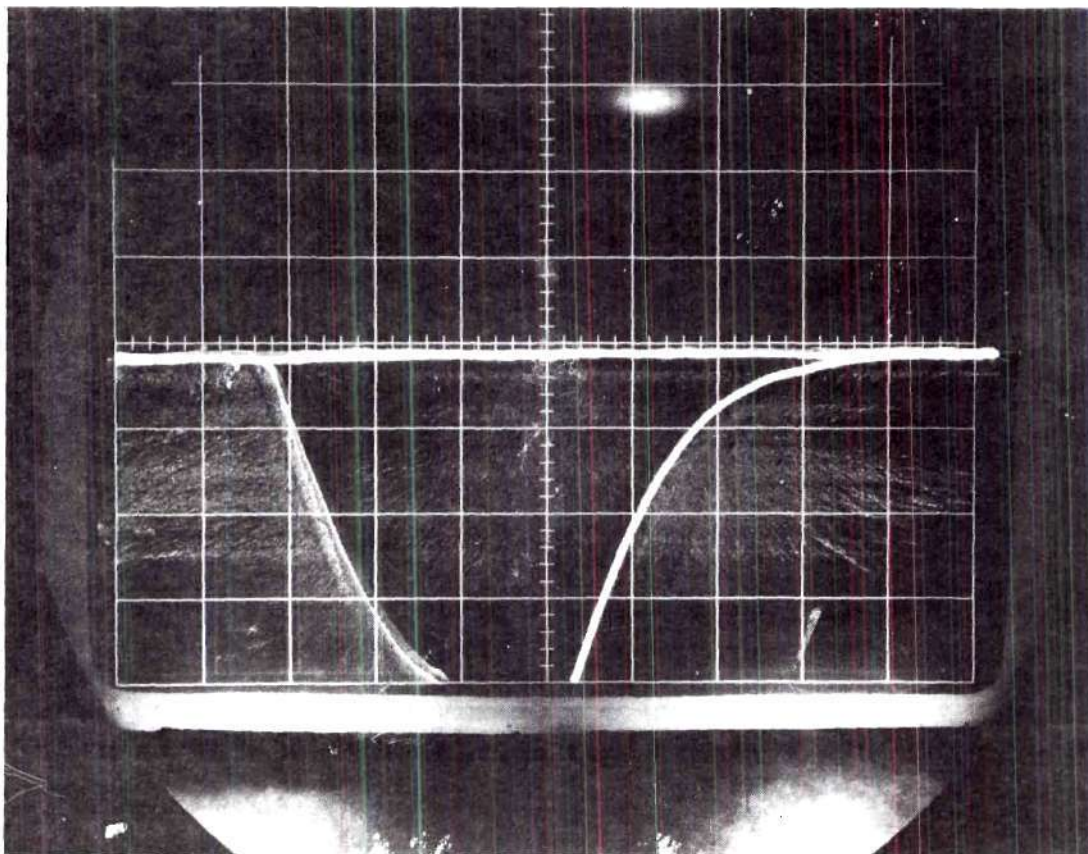
TIME SCALE: 0.2 SEC/DIVISION

EMF SCALE: 10 MV/DIVISION

Figure 24.   Typical Oscillograph Trace for One Cycle of Pulsed
Thermocouple Probe.
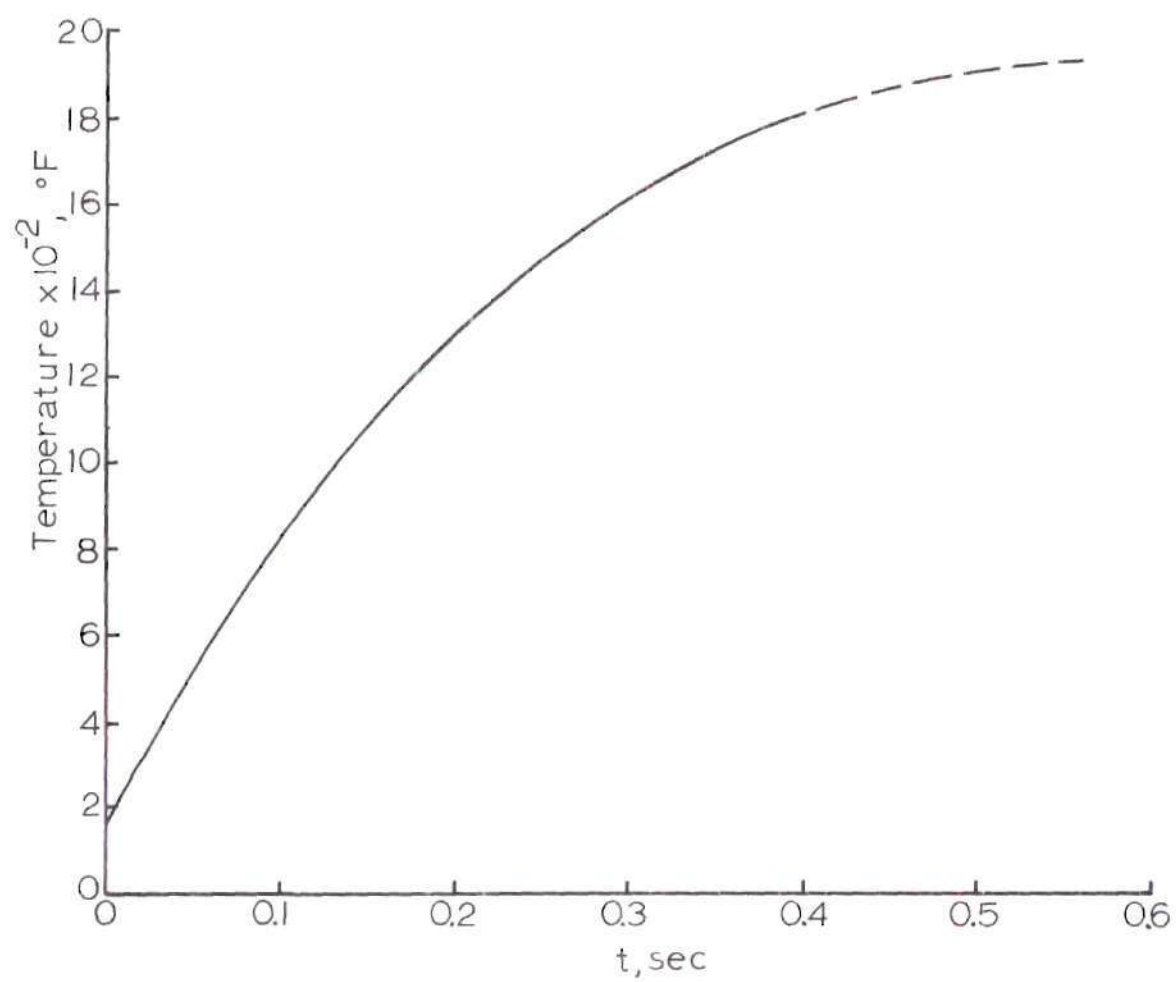
Figure 25. Temperature of Pulsed Thermocouple as a Function of Time

It was noted that a 300°F higher or 300°F lower value than the above resulted if t was decreased or increased, respectively. This probably resulted from the fact that small changes in $\bar{h}A/mC_p$ had a significant effect on T_g and the fact that C_p was not constant.

Although this technique does not give a precise determination of the gas temperature, it does not involve the usual requirement for determining the temperature-time derivatives. Accurate determination of these derivatives from transient thermocouple measurements are extremely difficult.

Chemical Species Measurements

Experimental measurements of concentrations were made on the hydrogen diffusion flame. The measurements were carried out by direct sampling and by using a gas chromatograph for quantitative analysis. These experiments were conducted without the entrained solid particles. In this case the water cooled, stagnation probe was used as a sampling probe. This probe has been previously described in Chapter III.

The presence of a condensible, H_2O, in the flame complicated the determination of the actual species concentrations. Water vapor condensed from the samples as they were extracted due to being cooled. This resulted in the concentrations in a sample being different from the concentrations in the flow. However, the mass ratios of the non-condensibles in the sample were not changed by the condensation of the water vapor. This fact made it possible to perform measurements with the cooled probe which could be related directly to the flame environment. This technique is presented later in this section.

Sampling System

The water cooled probe was mounted and aligned in the positioning device such that the probe opening was located at the stagnation point. The cooling water flow was kept at a maximum at all times, but the water was preheated to approximately 140°F prior to entering the cooling passages to prevent condensation on the probe. A schematic of the sampling system is shown in Figure 26, page 85. The system consists of the water cooled, sampling probe, positioning device, hose connections, sample chamber, micrometer valve, exhaust, and a 2.5 cm^3 syringe for sample transfer to the gas chromatograph. The sample chamber had a thick, selfsealing, flexible wall so that the syringe needle could be inserted into the sample chamber without leakage.

The entire system was pressurized prior to each series of tests and carefully checked for leaks. The exhaust from the vacuum pump was vented to the outside since free hydrogen was present in many cases. During initial tests with the system it was noticed that the opening of the micrometer valve, or sampling rate, had an effect on the sample obtained. However, it was observed that this effect could be eliminated by continuously flushing the system with the sample for several minutes. Also, with the micrometer valve full open the sample composition did not change after 20 seconds of flushing. As a result of these observations the following procedure was selected:

1. The probe's preheated coolant was turned on and allowed to come to a steady condition.

2. The vacuum pump was turned on with the micrometer valve in the full open position.

FLEXIBLE
SEAL
COOLANT

PROBE

MOTION

SLOTTED CHAMBER
WALL

POSITIONING DEVICE

SAMPLE SYRINGE

MICROMETER VALVE

EXHAUST

SAMPLE CHAMBER

VACUUM
PUMP
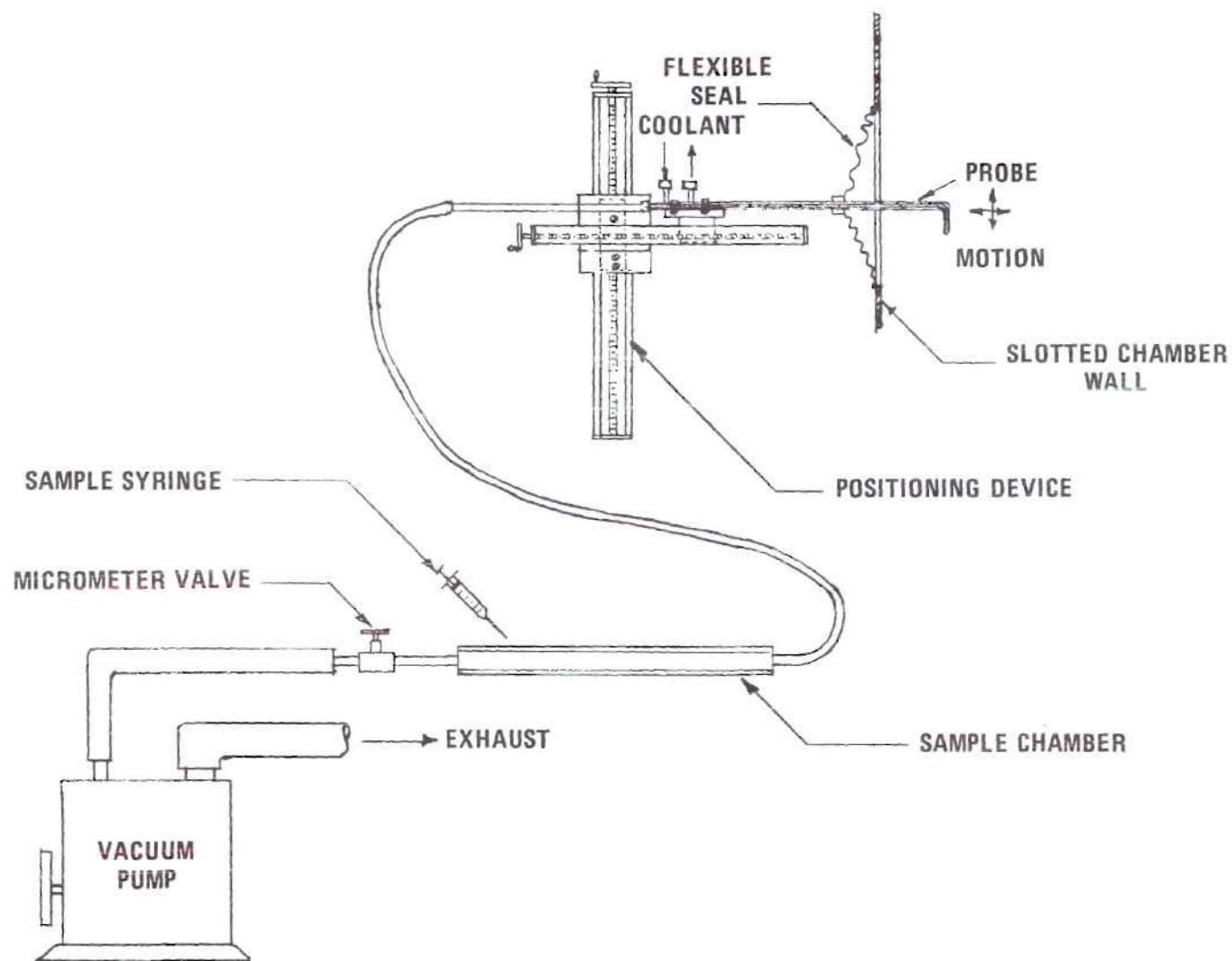
Figure 26. Schematic Drawing of Sampling System

3. The probe was positioned in the flame and the system flushed with the sample for 40 seconds.

4. The micrometer valve was closed and the sample chamber was allowed to reach the stagnation pressure in the test chamber.

5. The syringe needle was inserted through the sample chamber wall and a sample extracted.

During the flushing process the pressure in the sample chamber was maintained well below atmospheric until the micrometer valve was closed. This allowed the water vapor to pass through the system with little or no accumulation. Considerable condensation of water occurred in the vacuum pump exhaust system, however. A very slight amount was observed in some cases on the sample chamber interior walls after the micrometer valve was closed. This usually disappeared on the next flushing of the sample chamber so that no accumulation occurred.

Calibration of the Gas Chromatograph

The Beckman Gas Chromatograph with a conductivity cell was used for all composition measurements. Several factors had to be considered in using this instrument for these particular tests. First, oxygen was present in varying concentrations in the samples. This limited the current settings for the conductivity cell to low values to prevent irreversible changes in the elements of the cell. The elements at high current settings are at high temperatures and the injection of oxygen may completely destroy them. Second, it was entirely possible to have unreacted hydrogen and oxygen in a sample which could result in damage to the conductivity cell due to reaction on the surfaces of the elements if complete component separation was not obtained. Fortunately, the gas

column used accomplished a complete separation and no observable chemical reaction occurred on the elements during any of the tests. Third, the primary components which were present in a sample were H_2, N_2, O_2 and H_2O. Consequently, the differences in component sensitivities in the conductivity cell were very large.

The first effort to avoid the component sensitivity problem was to perform separate measurements for the components with more than one sample at one location. Two different carrier gases, helium and nitrogen, were used in these measurements. This required two entirely different adjustments and settings on the chromatograph, but did allow very accurate measurements to be performed. The disadvantage to this approach was the fact that different samples were used for different components. This introduced the additive error in sample sizes and, worst of all, the turbulent fluctuations of the flame appeared to affect the sample composition measured at a particular location at different times by as much as 15 percent for some components. The high accuracy obtainable with separate measurements on individual samples was lost on combining the results. A considerable amount of data was taken during these tests using separate measurements, but was not used due to this problem.

A much more satisfactory method was settled upon which sacrificed the very high accuracy possible with the chromatograph in order to make measurements of all components from the same sample. Examination of the data showed that the error involved was still quite low, only a few percent, and quite acceptable considering the complexities and unknowns associated with the turbulent, chemically reacting flow.

The method selected used argon as a carrier gas and a heated

molecular seive column and during the test the attenuator setting was switched to a higher value for the hydrogen component peak. Calibration data were obtained using an identical procedure with known samples.

It is possible to use either peak height or peak area measurements with properly prepared calibration data to determine concentrations. However, there are advantages and disadvantages to each and a choice must be made with consideration given to a number of factors. These include instrument temperature, flow rate and type of carrier gas, sample size, type and concentration of components, degree of resolution between sample components and the intended use of the data. The wide differences in the components of the samples meant large differences in component sensitivities as measured by areas. Also, all the components passed through the cell in a relatively short time, which meant that the peak width to peak height ratio was relatively low.

Due to the different characteristics of these components, the necessity of attenuator switching during the test and the associated increases in error, it was decided to carry out a series of calibration tests with known samples with a fixed carrier gas flow rate and instrument temperature. Both peak area and peak height measurements were made for all components and compared with additional measurements of known samples. The results of these tests showed that due to the reduced sensitivity at low filament currents and the accompanying reduction in precision, either method, peak area or peak height, could be used provided the carrier gas flow rate, instrument temperature and sample size were constant. There was a slightly better result obtained with the hydrogen component on a peak area basis, but for the other

components there were little differences in the two methods. As a result
of these tests the calibration was carried out on a weight basis using
hydrogen, nitrogen, and oxygen samples and comparing peak areas for
hydrogen and, for convenience, peak height for nitrogen and oxygen. The
instrument settings for all final calibrations and tests were as follows:

      carrier gas - argon

      carrier gas pressure - 30 psi

      filament current - 40 ma

      temperature - 40°C

      attenuator - 20 for hydrogen, otherwise 1

Sample Measurements

The presence of water vapor in the flame and its condensation in
the sampling system complicated these measurements. Actually the meas-
ured amount of each component in a sample was not identical to the con-
centrations in the flame due to the large temperature drop of the sample
and condensation. Also, it was not practical to maintain the entire
sampling system at temperatures above the boiling point of water to pre-
vent condensation, and the existing gas chromatograph system could not
be used to measure water vapor concentrations.

The ratio of the masses of any two non-condensibles in the system,
however, does remain constant with or without condensation. Conse-
quently, the ratio of nitrogen to hydrogen or nitrogen to oxygen will
be the same in the flame and the gas chromatograph sample.

As a convenient method of presenting the data, comparing the
numerical values with theory and using values directly relating to the
flame conditions, the following relationships were used.

Using the non-dimensional parameter

$$\bar{\beta} = \frac{\bar{C}_k - \bar{C}_{k_j}}{\bar{C}_{k_e} - \bar{C}_{k_j}} \qquad (4\text{-}7)$$

we have for the flame conditions

$$\bar{C}_H = C_{H_2} + \frac{2M_H}{M_{H_2O}} C_{H_2O} \qquad (5\text{-}3)$$

$$\bar{C}_O = C_{O_2} + \frac{M_O}{M_{H_2O}} C_{H_2O} \qquad (5\text{-}4)$$

$$\bar{C}_N = C_{N_2} \qquad (5\text{-}5)$$

Thus,

$$C_{H_2} + \frac{2M_H}{M_{H_2O}} C_{H_2O} - 1 = -\bar{\beta} \qquad (5\text{-}6)$$

$$C_{O_2} + \frac{M_O}{M_{H_2O}} C_{H_2O} = \bar{\beta}\, C_{O_{2_e}} \qquad (5\text{-}7)$$

$$C_{N_2} = \bar{\beta}\, C_{N_{2_e}} \qquad (5\text{-}8)$$

Examination of the data shows that the oxygen concentration within the reaction envelope is negligible except very close to the reacting region. The same is true for hydrogen outside the reaction envelope. This information can be used with the above equations to give two expressions for $\bar{\beta}$ in terms of the mass ratio of the non-

condensibles. Within the reaction envelope the following relationship holds:

$$\bar{\beta} = \frac{\left(\dfrac{m_{N_2}}{m_{H_2}}\right)}{C_{N_{2_e}} + \dfrac{m_{N_2}}{m_{H_2}}\left[1 + \dfrac{2M_H}{M_O}C_{O_{2_e}}\right]} \tag{5-9}$$

Outside the reaction envelope the expression is

$$\bar{\beta} = \frac{\dfrac{m_{N_2}}{m_{O_2}}\left(\dfrac{M_O}{2M_H}\right)}{\dfrac{m_{N_2}}{m_{O_2}}\left[C_{O_{2_e}} + \dfrac{M_O}{2M_H}\right] - C_{n_{2_e}}} \tag{5-10}$$

The limiting value of $\bar{\beta}$ for both equations

$$C_{H_2} \rightarrow 0$$

and

$$C_{O_2} \rightarrow 0$$

is 0.9724.

It should be noted that the two equations are strictly valid only in the regions where $C_{O_2} \equiv 0$ and $C_{H_2} \equiv 0$, respectively. In other words, in regions which are not close to the reaction envelope. At positions close to the reaction envelope, it is possible to have quantities of hydrogen and oxygen present. In this case the general equation for $\bar{\beta}$ may be used,

$$\bar{\beta} = \cfrac{\cfrac{m_{N_2}}{m_{O_2}}}{\cfrac{m_{N_2}}{m_{O_2}}\left[\cfrac{2M_H}{M_O}C_{O_{2e}} + \cfrac{C_{N_{2e}}}{C_{O_{2e}}\left(\cfrac{m_{N_2}}{m_{H_2}}\right)} + 1\right] - \cfrac{2M_H}{M_O}C_{N_{2e}}} \qquad (5\text{-}11)$$

The two previous $\bar{\beta}$ equations can be obtained from this equation by imposing the conditions $C_{O_2} \rightarrow 0$ and $C_{H_2} \rightarrow 0$, respectively.

Two typical chromatograph traces are given in Figures 27 and 28, pages 93 and 94. The first is a sample taken on the centerline at a height of 9" above the hydrogen nozzle. The "hash" which resulted from the scale change made during the run was removed from the trace and replaced by the broken lines as shown in the figures. The traces shown on the lower scale represents a standard number of "counts per unit time" and the total number represented by the entire trace of a component is a measure of the area under the component peaks.

The components shown in Figure 27, page 93, are hydrogen and nitrogen only. Of course a small amount of water vapor was present in practically all samples, but this component does not show on the chromatograph traces. The amount of water vapor present in a one cubic centimeter sample is approximately that corresponding to the vapor pressure of water at room temperature. At a room temperature of 68°F this water vapor volume represented a maximum of two percent of the sample volume. This also means that the sum of the measured volumes of the components will not total 1.0 cm^3 for samples containing water vapor. If it is known that the amount present is that represented by saturation
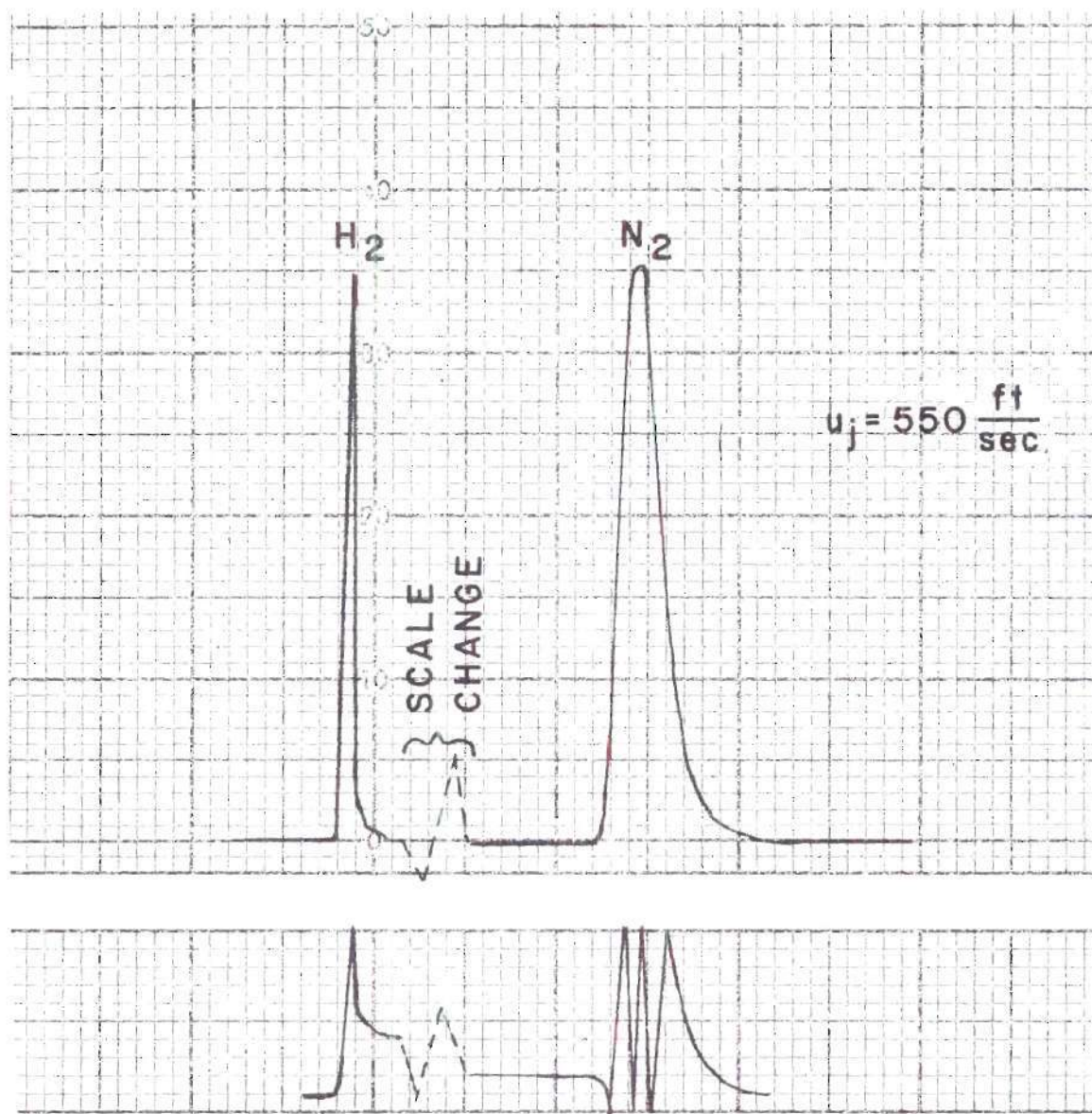
Figure 27. Typical Gas Chromatograph Trace of a Sample at
h/d = 22 and r/r_o = 0.0
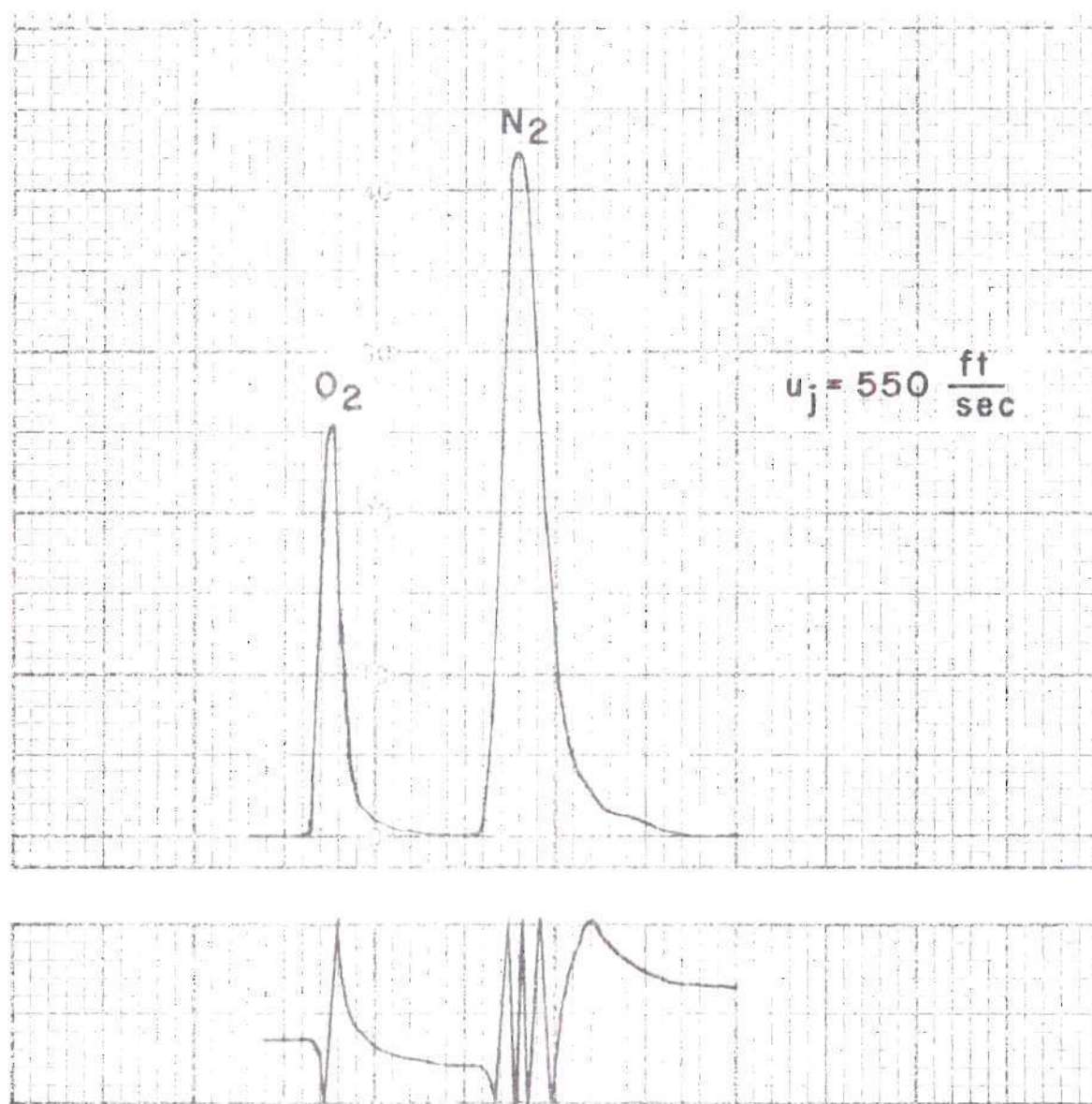
Figure 28. Typical Gas Chromatograph Trace of a Sample at
h/d = 22 and r/r_o = 16.

conditions at the sample extraction temperature then the volume of water
vapor in a sample can be calculated. As pointed out in the preceding
discussions, however, the mass ratio of the non-condensible components
is the same in the flame and the sample. The handling of the data
based on this ratio avoids the complications introduced by the conden-
sation and sample volume variations.

The chromatograph traces shown in Figure 28, page 93, show oxygen
and nitrogen components only. This sample was taken at a position out-
side the reaction envelope at h/d = 22. The "hash" on this trace
occurred prior to the oxygen peak as a result of switching the attenua-
tor setting during the test and consequently, it was not necessary to
interrupt the chromatograph trace to present the results.

The concentration data for measurements along the centerline are
given in Table 6, Appendix B, page 164. The measured quantities of hydro-
gen, nitrogen and oxygen are given for several samples extracted at
various positions along the jet centerline. Also, the mass fraction
ratios for the non-condensibles are given with the corresponding values
of $\bar{\beta}$. All of these measurements were made within the reaction envelope
so that values of $\bar{\beta}$ were determined with the measured data and equation
(5-9). The data are plotted in Figure 29, page 96, showing both β and
C_{N_2}/C_{H_2} as functions of height above the hydrogen nozzle.

The chemical species variation with radial position is given by
the data in Table 7, Appendix B, page 165. These data were obtained with
samples extracted at a height of h/d = 22. The mass fraction ratios of
nitrogen and hydrogen and nitrogen and oxygen are also given in the
table. A plot of the compositions of one cubic centimeter samples in
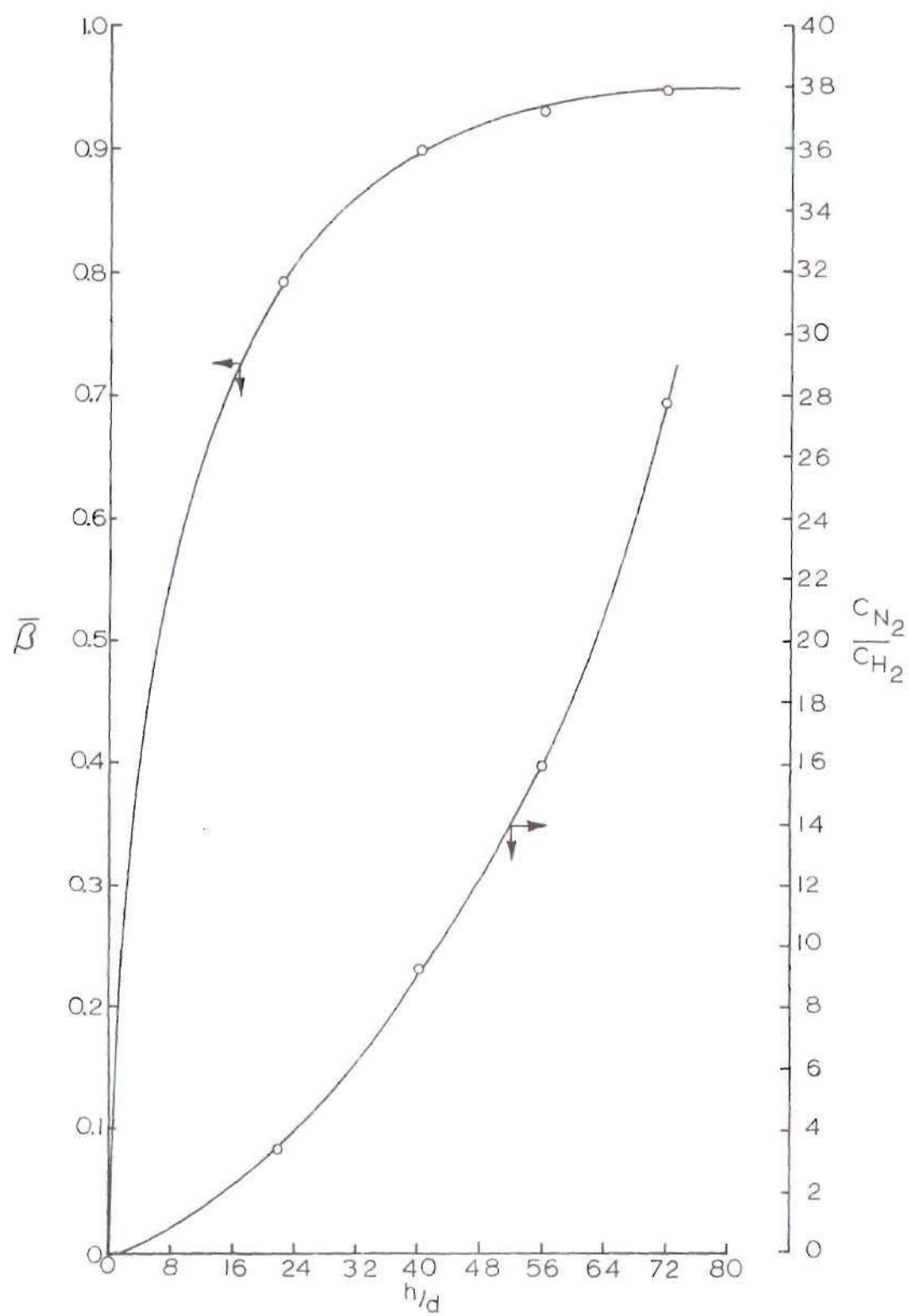
Figure 29.   Centerline Concentration Ratios

terms of mole fraction as a function radial position is given in Figure
30, page 98. A plot of the mass fraction ratios of the non-condensibles
is given in Figure 31, page 99, as a function of radial position. All
of the data given in Table 2, page 101, was not included on this plot
in order to have an expanded scale for the mass fraction. These few
data points would fall on the curve if it were extrapolated upward in
the reacting regions.

The variation of $\bar{\beta}$ with radial position is given in Figure 32,
page 102, for a height of h/d = 22. Equation (5-9) and the mass frac-
tion ratios of hydrogen to nitrogen were used to plot the curve within
the reaction envelope. The curves are joined at two points calculated
with equation (5-11) and data on m_{N_2}/m_{H_2} and m_{N_2}/m_{O_2} for each of
the points.

The measured data which has been presented thus far on the
chemical species in the flame has been in terms of $\bar{\beta}$ or mass fraction
ratios. The actual concentrations of hydrogen, nitrogen, oxygen and
water vapor in the flow may be calculated from this data, however.
Equations (5-9), (5-10) and (5-11) were used with the measured values
of C_{N_2}/C_{H_2}, C_{N_2}/C_{O_2} and $\bar{\beta}$ to give the actual concentrations. These
data for the centerline variations of the chemical species are given in
Table 1, page 100 and Figure 33, page 103, and for radial variation at
h/d = 22 in Table 2, page 101, and Figure 34, page 104.

Particle Distribution

The solid combustibles used in the investigation were aluminum
powder with an average particle size of 50 microns. The powder was
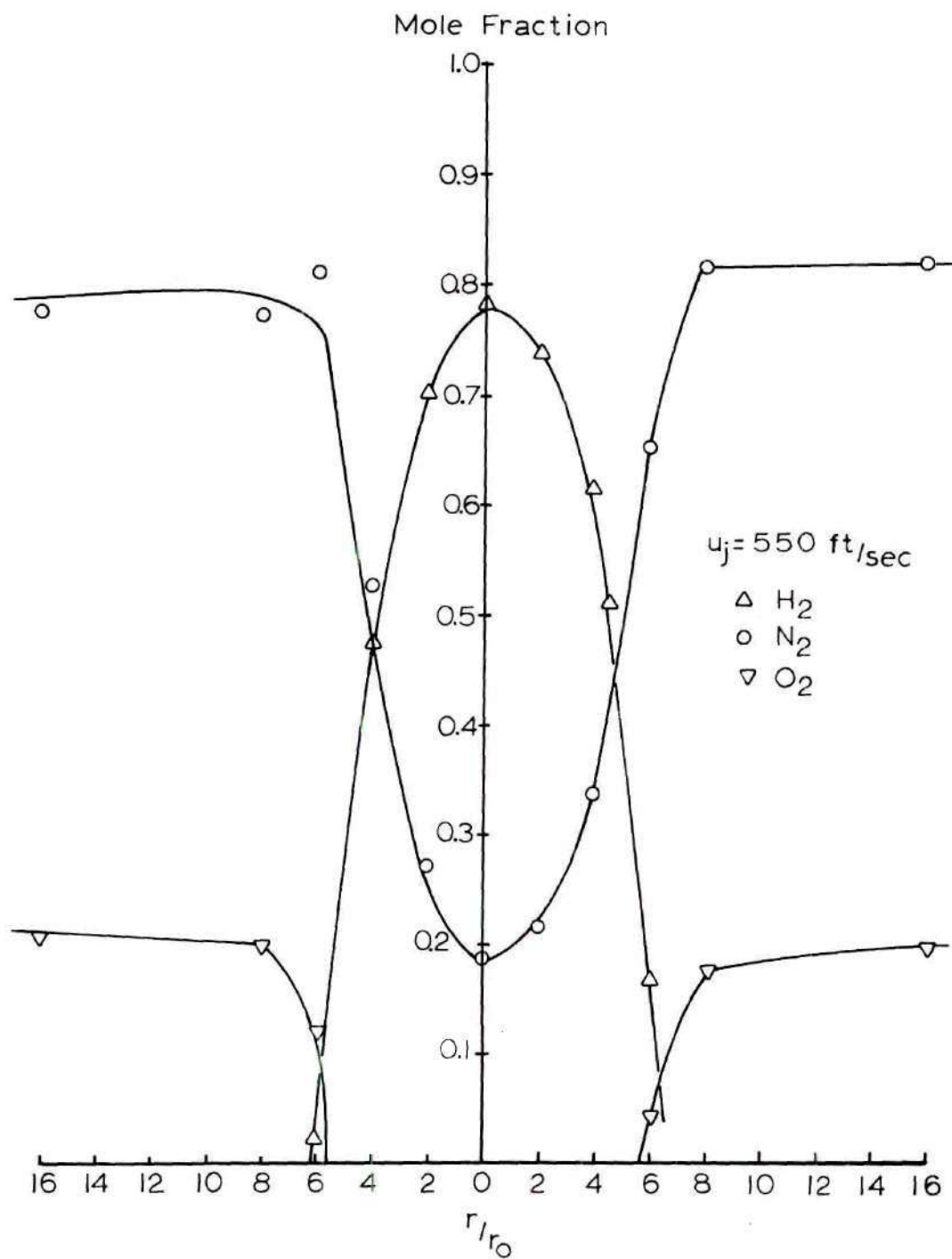
Figure 30. Composition of Sample as Function of Radial Position at h/d = 22
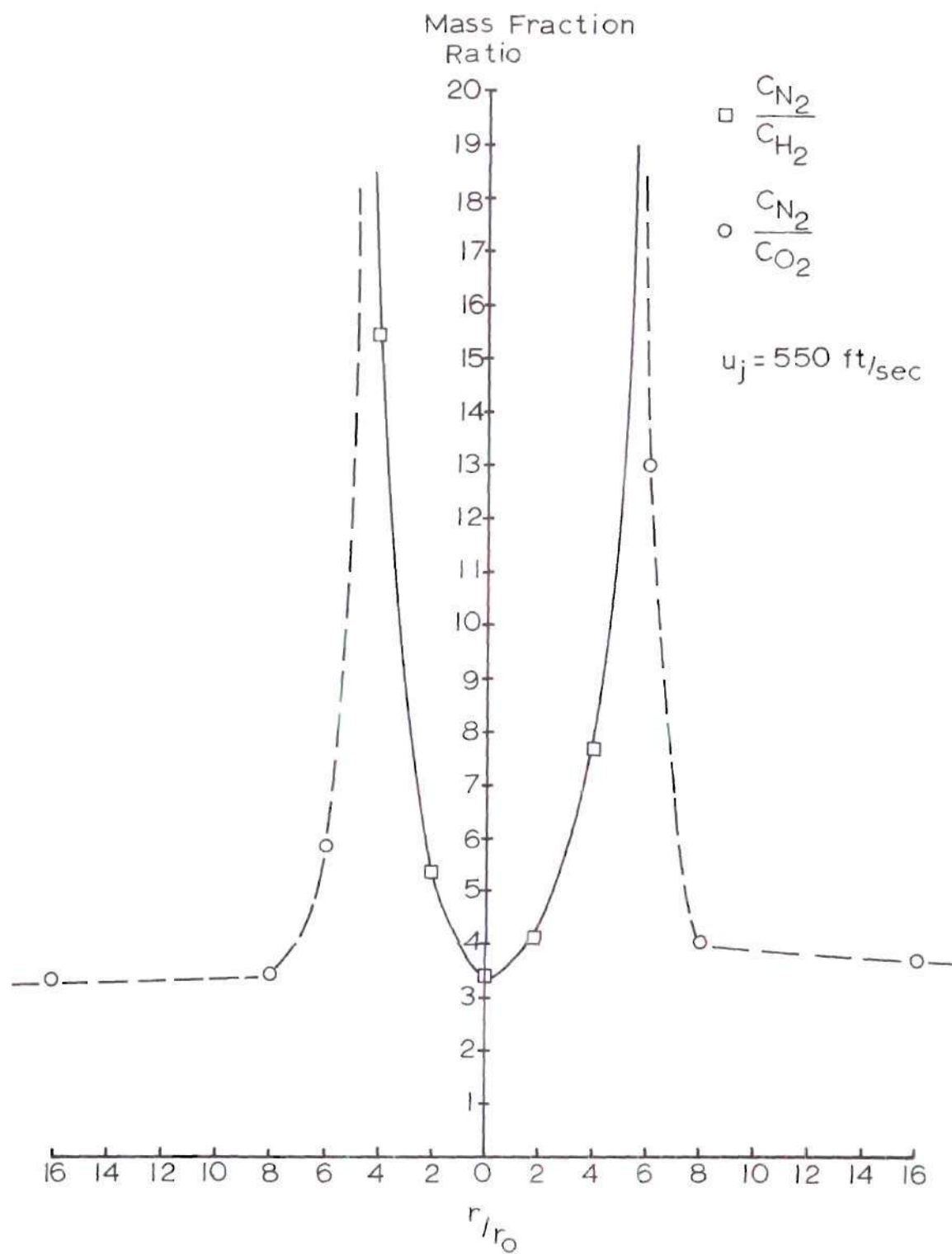
Figure 31. Radial Variation of Mass Fraction Ratios of Non-Condensibles at $h/d = 22$.

Table 1. Centerline Chemical Species Concentrations

h/d	$\bar{\beta}$	C_{N_2}	C_{H_2}	C_{H_2O}	X_{N_2}	X_{H_2}	X_{H_2O}
0	0	0	1.0	0	0	1.0	0
22	0.7926	0.6143	0.1849	0.2008	0.1758	0.7349	0.0893
40	0.8988	0.6966	0.0757	0.2277	0.3314	0.5002	0.1684
56	0.9285	0.7196	0.0452	0.2352	0.4201	0.3665	0.2134
72	0.9467	0.7332	0.0264	0.2404	0.4976	0.2488	0.2536

Table 2. Chemical Species Concentrations for h/d = 22

r/r_0	$\bar{\beta}$	c_{N_2}	c_{O_2}	c_{H_2}	c_{H_2O}	x_{N_2}	x_{O_2}	x_{H_2}	x_{H_2O}
48	1.00	0.7750	0.2250	0	0	0.7974	0.2026	0	0
16	1.00	0.7750	0.2250	0	0	0.7974	0.2026	0	0
8	1.00	0.7750	0.2250	0	0	0.7974	0.2026	0	0
6	0.9869	0.7647	0.1306	0.0016	0.1029	0.7205	0.1078	0.0209	0.1508
4	0.9272	0.7186	0	0.0465	0.2349	0.4155	0	0.3734	0.2111
2	0.8524	0.6606	0	0.1235	0.2159	0.2436	0	0.6326	0.1238
0	0.7926	0.6143	0	0.1849	0.2008	0.1758	0	0.7349	0.0893
2	0.8206	0.6360	0	0.1561	0.2079	0.2034	0	0.6933	0.1033
4	0.8854	0.6862	0	0.0895	0.2243	0.3012	0	0.5457	0.1531
6	0.9659	0.7486	0.0574	0.0139	0.1801	0.5886	0.0395	0.1518	0.2201
8	0.9955	0.7715	0.1891	0	0.0394	0.7729	0.1658	0	0.0613
16	0.9980	0.7735	0.2265	0	0	0.7974	0.2026	0	0
48	1.00	0.7750	0.2250	0	0	0.7974	0.2026	0	0
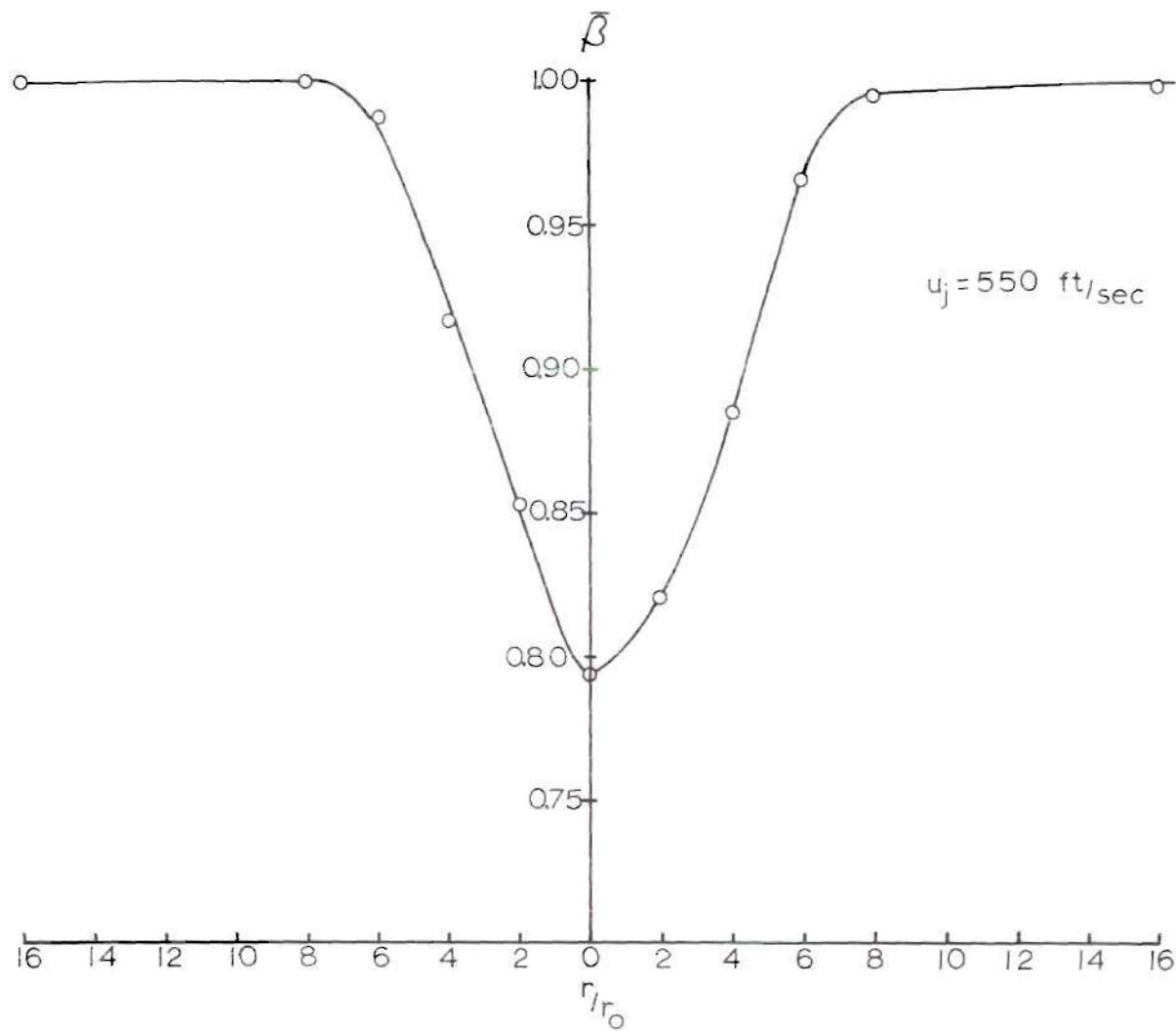
Figure 32. Radial Variation of $\bar{\beta}$ at h/d = 22
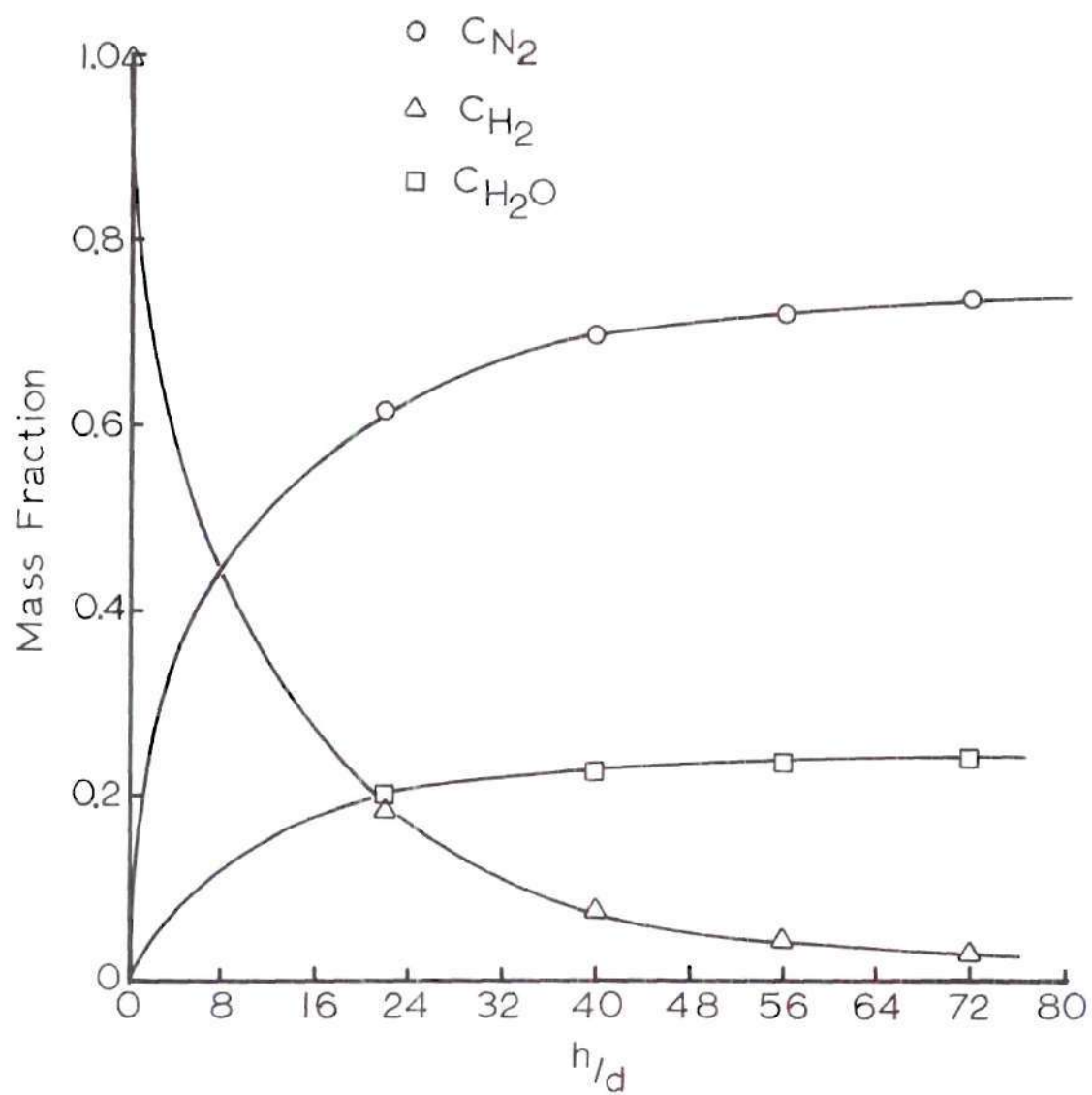
Figure 33. Centerline Species Concentrations.
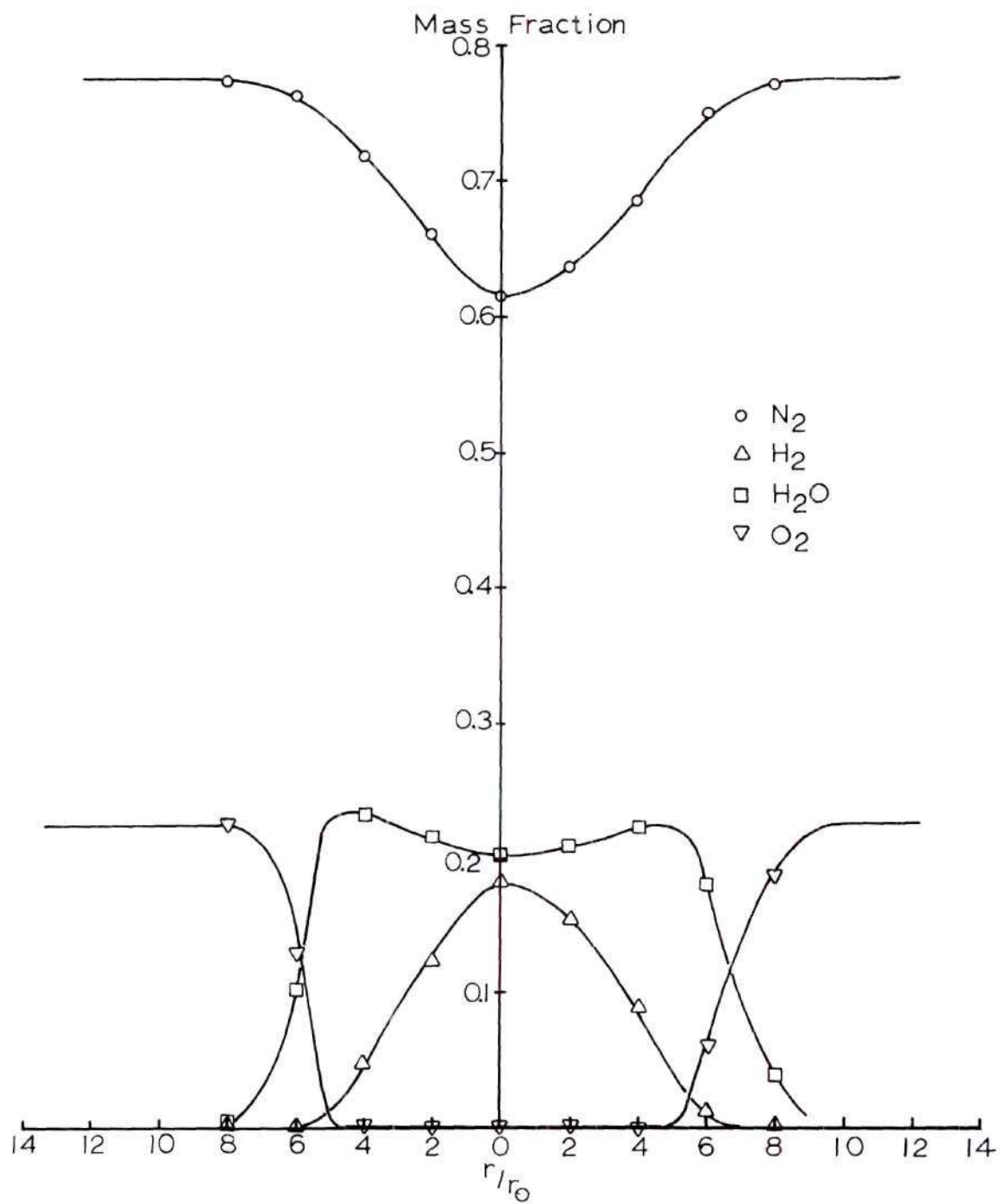
Figure 34.   Radial Variation of Species Concentrations

mechanically fed with a hydrogen carrier gas at a controlled rate into
a hydrogen jet. The particles were entrained in the hydrogen jet and
conveyed through the mixing region within the test chamber by the flow.
Initially, all of the particles were inside the reaction envelope and
no particles ignited and burned until they crossed the reaction envelope.

The purpose of this part of the investigation was to determine by
experimental measurements the distribution of the mass flux of aluminum
throughout the mixing region and to determine the actual aluminum mass
density and particle density in the flow. This required the development
of a suitable technique for sampling the particles in the flow and deter-
mining the aluminum content of the sample.

Generally speaking, the aluminum particles in the hydrogen
stream pass upward through the fuel nozzle into the test chamber. On
leaving the nozzle each of the particles is influenced by the turbulent
mixing and spreading of the jet and each particle is heated as it moves
upward. The velocity of the particles at the fuel jet was probably
very close to the velocity of the gaseous jet. Consequently, each
particle possessed a significant momentum in the vertical direction
which may have influenced the spreading of the particles. It is
natural to expect the particles to be concentrated along the centerline
of the concentric jets at positions near the nozzle exit. At higher
positions in the flow the particles spread out across the jet with a
reduction in the centerline concentration. Depending on the actual
spreading of the particles, a number may remain within the reaction
envelope of the flame where there is little or no oxygen. These par-
ticles are heated by radiation from the high temperature combustion

region and by conduction and convection inside this region while moving
the entire length of the flame. Thus, some of the particles arrive at
the upper regions of the flame after being heated for a relatively long
period. A very bright, elongated reaction region develops in the flame
tip in this case as the aluminum vapor and molten droplets move into the
flame tip region.

The measurements reported in this section are for three differ-
ent particle feed rates, corresponding to particle feeder settings of 100,
50, and 0. These measurements were carried out at h/d = 22 and a con-
stant hydrogen flow rate. Additional measurements were obtained at a
particle feeder setting of 50 at h/d = 72.

Particle Distribution Measurement Technique

In order to measure the particle distribution across the con-
centric jets, it is necessary to distinguish between oxidized, or par-
tially oxidized particles, and those which have not ignited. To accom-
plish this directly represents a very difficult, if not impossible task.
For this reason, a method was utilized which allowed measurement of the
distribution of elemental aluminum in condensed phase across the flame
and these measurements, coupled with data of the average particle size
and local velocities, allowed the particle distribution to be calcu-
lated. This technique does not identify the burned or unburned par-
ticles, but does give the particle concentration as a function of spa-
tial position within the flame.

A particle collector was constructed using a thin strip of pyro-
lytic boron nitride (BN) attached to a metal rod which could be rotated.
The pyrolytic form of boron nitride is inert in the flame environment

and does not exhibit any tendency to crack due to thermal shock. The boron nitride collector strip was 2" x 1/4" x 0.030". The strip was inserted across the jets by means of the metal rod, with the strip aligned with the flow. Once in position the strip was rotated 90 degrees until it was perpendicular to the flow and after being exposed for a period of time rotated back to its original position and immediately withdrawn from the flame. The exposure time for the collector varied slightly from sample to sample and on a first inspection this may appear to create a serious difficulty. However, as shown in the following paragraphs, exposure time for the collector and the projected area terms were eliminated from the analysis by a simple technique.

If it is assumed that the 1/4" wide collector is sufficiently small compared to the jet diameter and that all of the particles which impinge on the collector stick to it, then the following analysis can be made for the mass of aluminum adhering to the collector.

The mass of aluminum adhering to a small segment of the collector can be approximated by

$$M_i = \rho_i V_i A_i' t \tag{5-12}$$

where

M_i = mass of aluminum on the ith segment of the collector, lbm

t = total exposure time, second

V_i = velocity of the particles, ft/sec

A_i' = average projected area exposed during the $\pm 90°$ rotation, ft^2

ρ_i = aluminum density in the gas, lbm/ft^3

Dividing by the product of the actual area, A, and the exposure time, t, yields

$$m_i = \rho_i V_i \frac{A_i^0}{A} \qquad (5\text{-}13)$$

where

$$m_i = \frac{M_i}{At} \qquad (5\text{-}14)$$

A_i^0/A is a constant for a given collector strip and m_i is the particle flux impinging on the ith collector segment during the time, t.

If the particle distribution is assumed to be symmetric about the centerline then the total mass of particles per unit time in the flow impinging on a washer shaped area at a distance r_i from the center is

$$M_{T_i} = \pi m_i (r_i^2 - r_{i-1}^2) \qquad (5\text{-}15)$$

and the total mass flux of aluminum across the entire flow is

$$M_T = \sum_i \pi m_i (r_i^2 - r_{i-1}^2) \qquad (5\text{-}16)$$

Thus, the fraction of the total aluminum mass flux through a washer shaped area at a distance r_i from the center is given by

$$\frac{M_{T_i}}{M_T} = \frac{\rho_i V_i (r_i^2 - r_{i-1}^2)}{\sum_i \rho_i V_i (r_i^2 - r_{i-1}^2)} \qquad (5\text{-}17)$$

Now, writing the area of the ith segment as $2\pi r_i \Delta r$ and all Δr's equal, then

$$\frac{M_{T_i}}{M_T} = \frac{\rho_i V_i r_i}{\sum\limits_i \rho_i V_i r_i} \qquad (5\text{-}18)$$

These expressions also represent the particle flux distribution across the flame if the particles are assumed to be of uniform size. Thus

$$\frac{N_{T_i}}{N_T} = \frac{\rho_i V_i r_i}{\sum\limits_i \rho_i V_i r_i} \qquad (5\text{-}19)$$

where

N_{T_i} = particle flux through a washer shaped area at $r = r_i$

N_T = total particle flux

The above equations give a convenient method for calculating the particle distribution using independent measurements of velocities, the total aluminum particle feed rate, and measurements of the mass of aluminum on the collector strip per unit area.

This last measurement, however, requires the determination of the quantity of elemental aluminum present at each location on the collector strip. The method utilized in this study was neutron activation analysis using the Georgia Tech Research Reactor for a neutron source.

Each collector strip of boron nitride was sectioned and each

small piece irradiated for one minute in the research reactor. A gamma spectrum was obtained on each segment and the peak representing the aluminum isotope identified. This "peak" was integrated and the result compared with standard sample measurements of known quantities of aluminum on one side of a piece of pyrolytic boron nitride. It should be noted that since boron has such a large cross section for slow neutrons, the aluminum sample was not irradiated from all sides. The collector strip blocked the neutron flux from one side and consequently the standard samples had to be prepared with aluminum on only one side of the boron nitride segment. For the same reason it was necessary to insure that none of the aluminum particles were dislodged from the boron nitride segments during exposure to the neutron flux. If this happened an extremely high reading would be obtained. This occurred with two segments of the collector strip for the $h/d = 72$ and a feeder setting at 50 in these tests. These two readings were discarded without seriously affecting the distribution measurements. Also, it should be noted that a significant gamma heating occurred with boron nitride and therefore the total exposure time in the plastic sample carrier was limited.

The data on each measurement and the calibration measurements are given in Appendix D, page 169 along with a brief discussion of the measurement technique. A typical curve for a complete gamma spectrum is given in Figure 35, page 111 with the aluminum peak identified.

The determination of M_{T_i} was obtained from these measurements by noting that it is the mass flux of elemental aluminum through a washer shaped area symmetric about the jet centerline at a distance r_i from
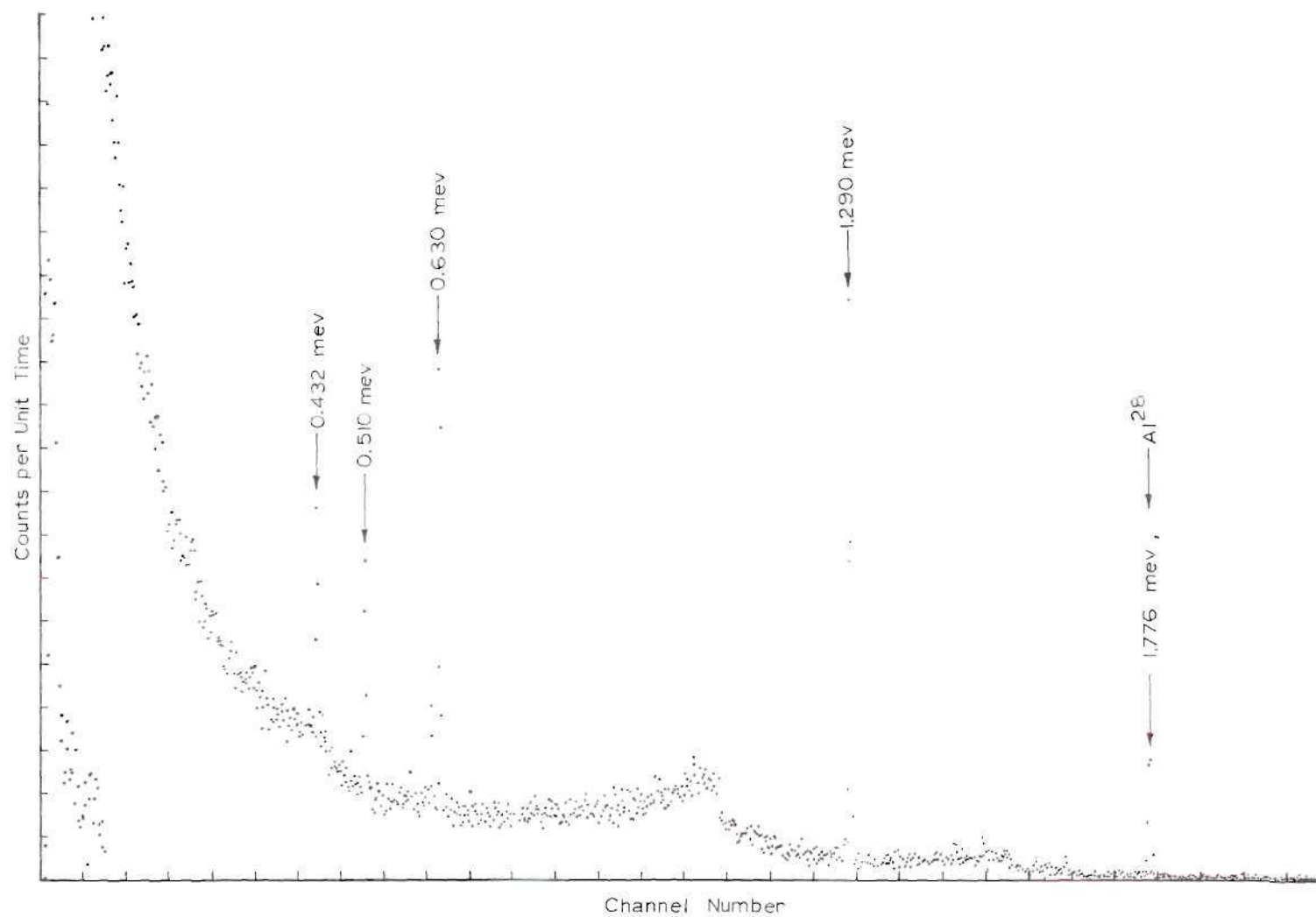
Figure 35. Typical Spectrum of Aluminum Sample on Boron Nitride
Collector, 1024 Channels, 2 Kev per Channel.

the center.

Thus

$$M_{T_i} = \frac{\pi(r_i^2 - r_{i-1}^2)m_{Al_i}}{t} \tag{5-20}$$

where m_{Al_i} is the mass per unit area of elemental aluminum measured on a sample located at an average distance of r_i from the center line.

Particle Distribution Measurements

The concentrations of elemental aluminum on the boron nitride collector strip measured by neutron activation analyses are plotted in Figures 36 through 39, pages 113 through 116, with mass per unit area as the ordinate and X as the abcissa. In this case X is the distance in inches measured on sample lengths equal to the bar widths. A curve is drawn through these average values locating a "peak" in the distribution of aluminum across the jet. This point was assumed to correspond to the jet centerline and the radial positions were measured from this point. It can be seen from the graphs that this does not involve large inaccuracies since the centerline concentrations are high and a maximum can be easily approximated. The total aluminum flux was determined by the setting of the powder feed rate. The calibration curve for the powder feeder is given in Figure 5, page 26. It should be noted that zero feed rate does not mean zero particle flux.

The results of these measurements are presented in Figures 36 through 39, pages 113 through 116, as m_{Al_i} vs. distance from the end of the collector strip. The measurements were carried out for three
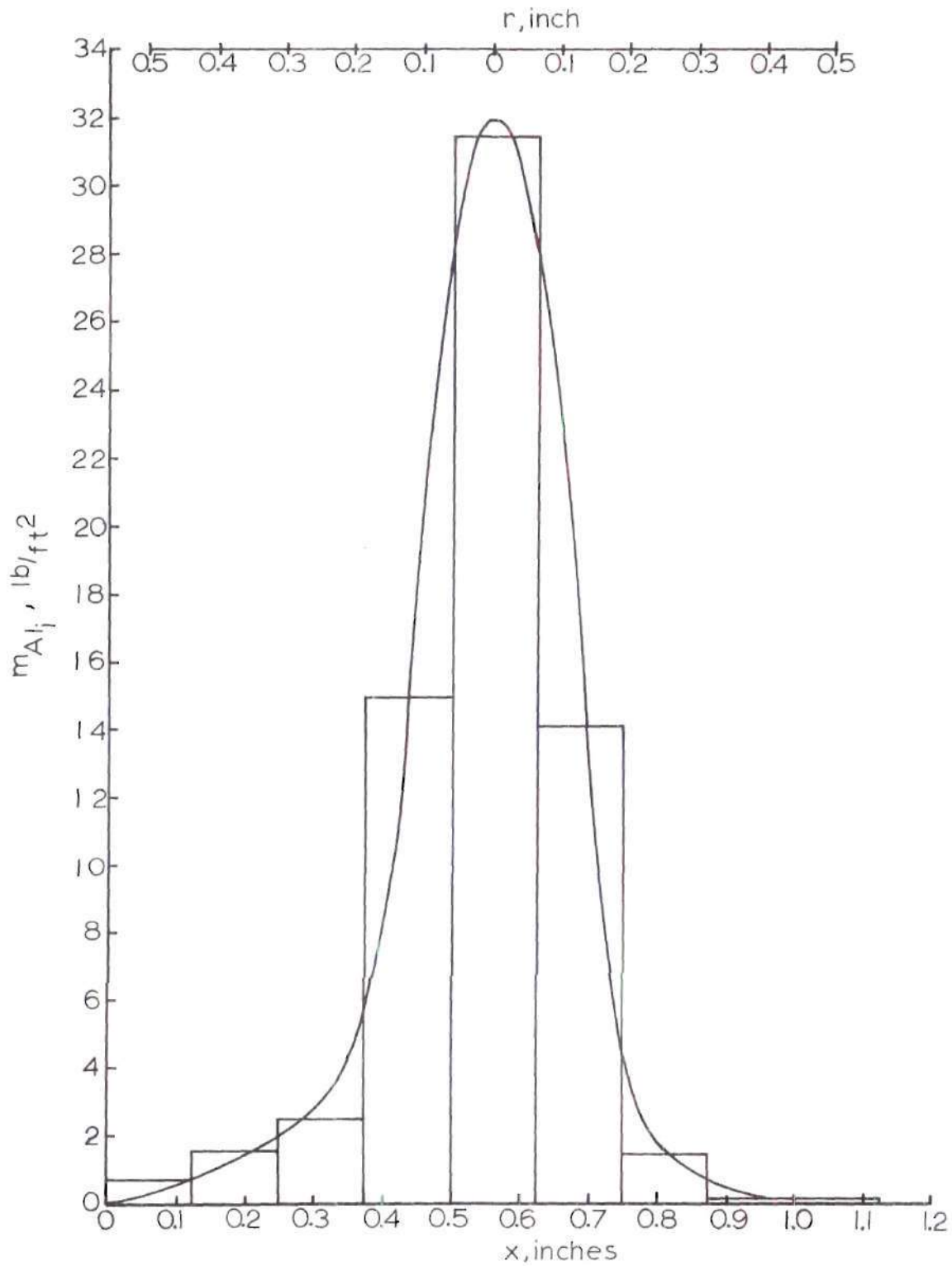
Figure 36.   Aluminum Distribution on a Boron Nitride Collector at
h/d = 22 and Feeder Setting at 100.
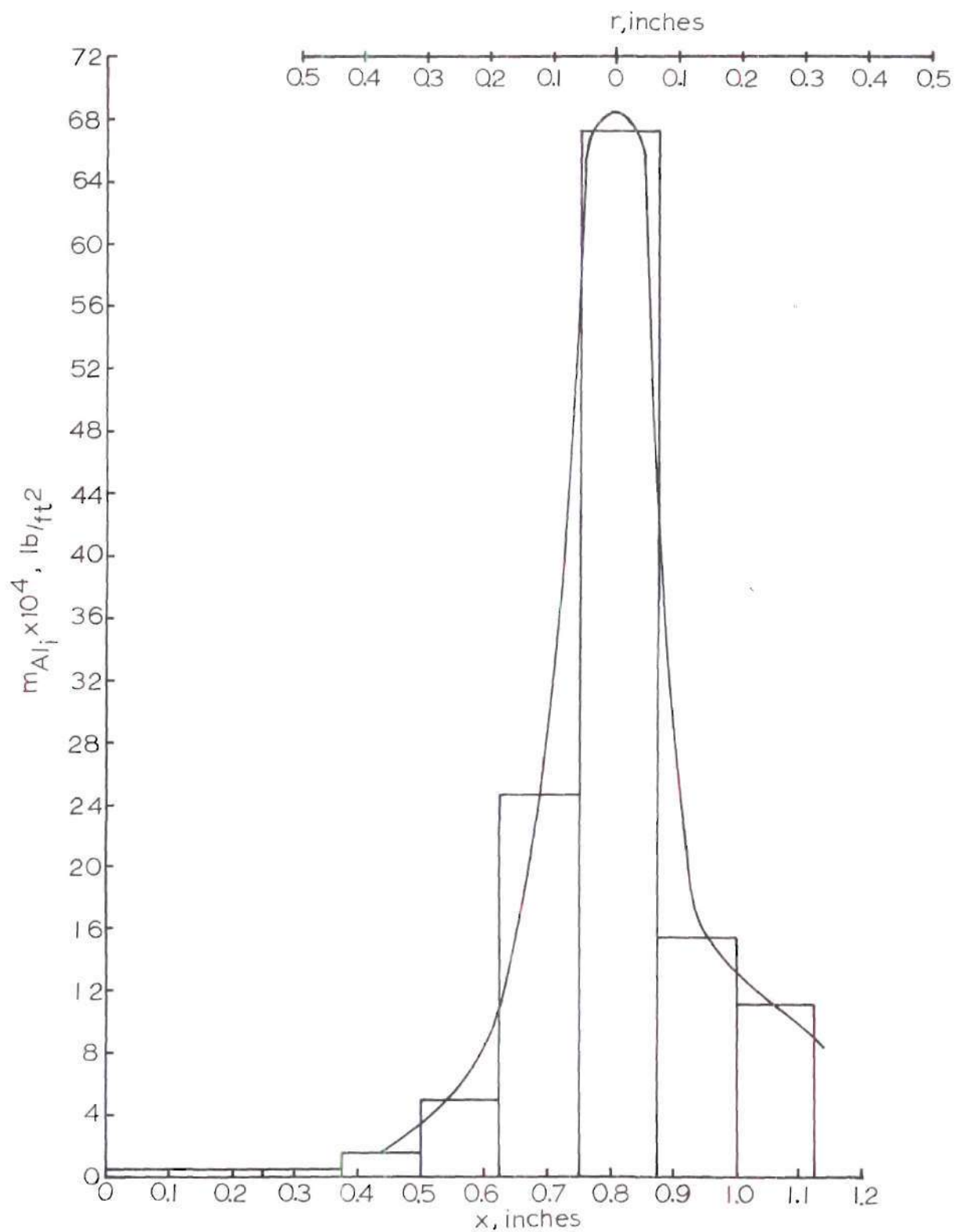
Figure 37. Aluminum Distribution on a Boron Nitride Collector at
h/d = 22 and Feeder Setting at 50.
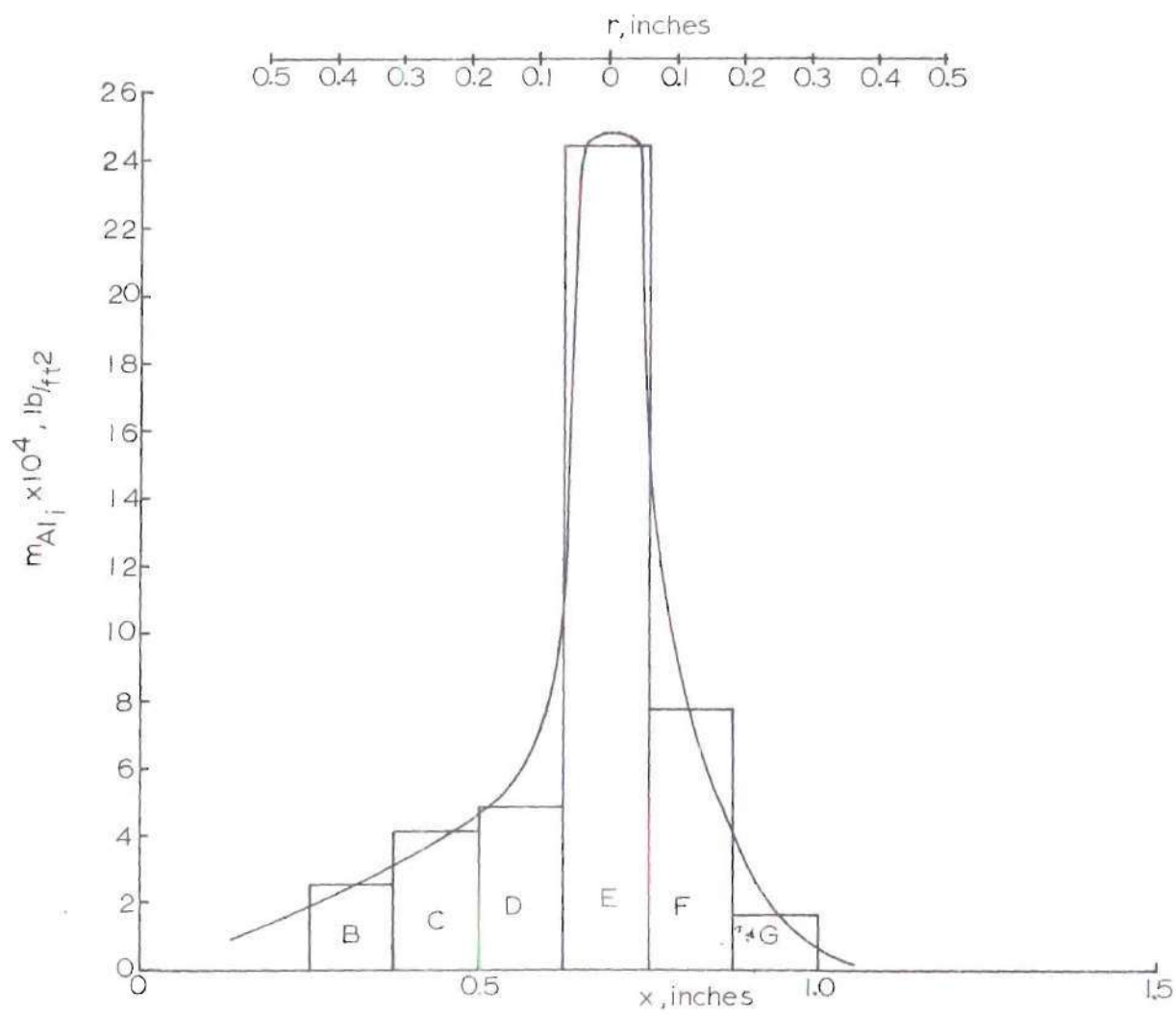
Figure 38. Aluminum Distribution on a Boron Nitride Collector at
h/d = 22 and Feeder Setting at Zero.
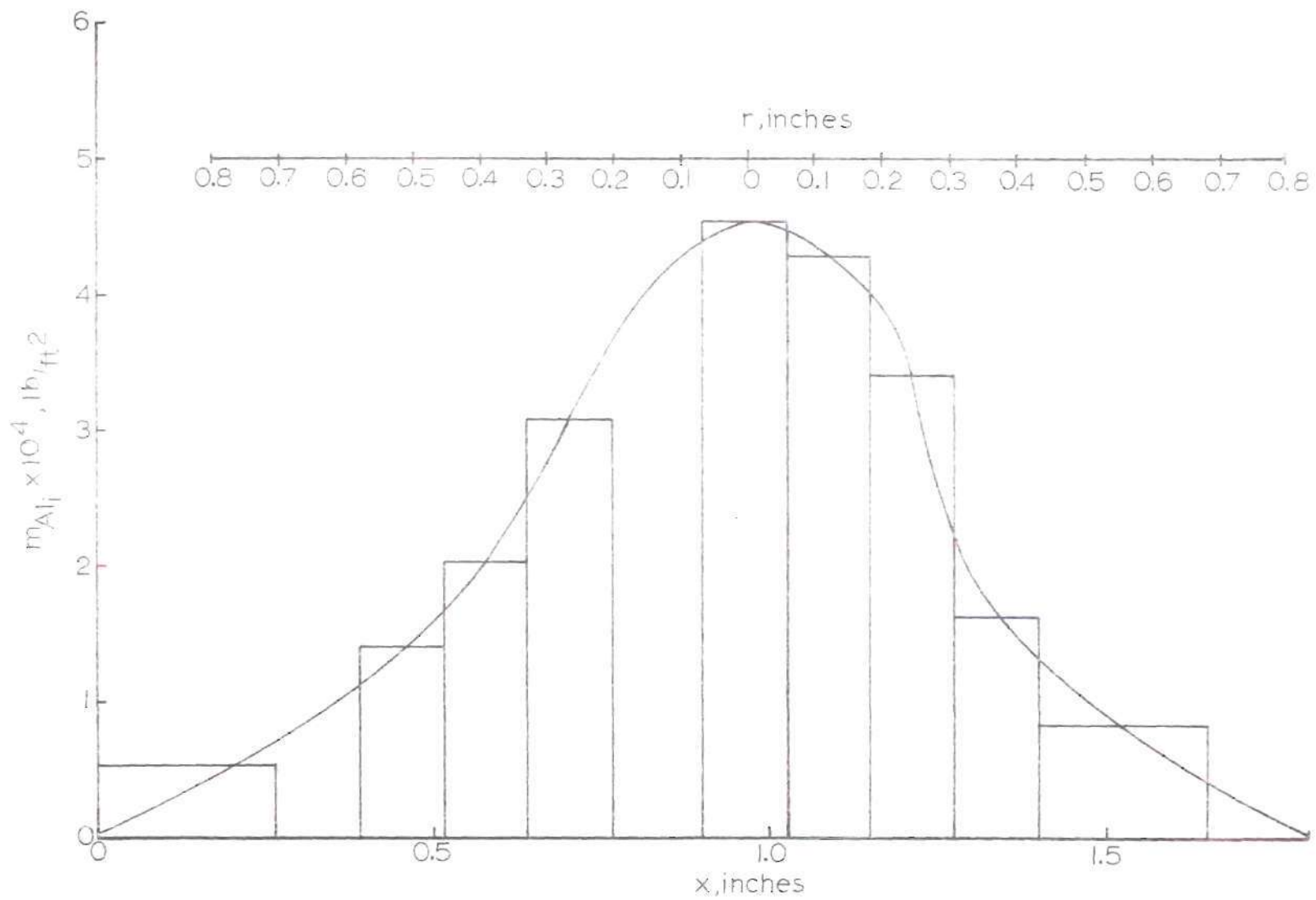
Figure 39.   Aluminum Distribution on a Boron Nitride Collector at
h/d = 72 and Feeder Setting at 50.

different feeder settings at a height in the flame of h/d = 22, and for
a feeder setting of 50 for a position higher in the flame, h/d = 72. It
is pointed out that these values do not correspond directly to the par-
ticle flux due to geometrical considerations and since the velocities
can be expected to vary across the flow. An expression for the total
mass flux of aluminum can be written as

$$M_T = \sum_i \frac{\pi(r_i^2 - r_{i-1}^2)m_{Al_i}}{t} \tag{5-21}$$

and similarly

$$N_{T_i} = \frac{\pi(r_i^2 - r_{i-1}^2)m_{Al_i}}{t\,a} \tag{5-22}$$

where a = mass per particle

In this case the aluminum particle flux is given by

$$\frac{\rho_i v_i}{a} = M_T \left(\frac{M_{T_i}}{M_T}\right) \frac{1}{\pi(r_i^2 - r_{i-1}^2)} \tag{5-23}$$

and with corresponding data on the velocities, the particle density is
given by

$$\frac{\rho_i}{a} = M_T \left(\frac{M_{T_i}}{M_T}\right) \frac{1}{\pi(r_i^2 - r_{i-1}^2)} \frac{1}{v_i} \tag{5-24}$$

In the last two expressions the values of (M_{T_i}/M_T) are obtained using

equations (5-20) and (5-21) and the neutron activation analysis results. The calculations were performed using data from the curves in Figures 36 through 39, pages 113 through 116, M_T values from the powder feeder calibration curve, and values of $(r_i - r_{i-1})$ of 0.02 inches.

The results for the aluminum flux distributions are given in Figures 40 through 43, pages 119 through 122, and the fraction of the total particles lying outside a given radial position are given in Figures 44 through 47, pages 123 through 126.

The data presented so far includes the effect of the particle velocities in the results. This means that only particle flow rates per unit area or mass flow rates per unit area have been given. The data on the aluminum mass flux distribution also includes the velocity effect since it involves the flow of particles through a given area for a particular period of time divided by the total particle flow for the same time period.

In order to obtain particle concentrations across the flow field, the average particle size must be specified and the velocity distribution of the particles across the flow must be obtained. The aluminum powder used in these experiments was obtained from Alcan Metal Powders, Incorporated. It is grade MCX-85-1 and sold as spherical particle aluminum powder. The average particle size specified by the manufacturer was 50 microns.

In order to characterize the particles and to inspect the samples collected in the flame, a series of photographs were taken using optical microscopy techniques. Due to the small sizes of these particles the photographs with high magnifications were not satisfactory. This is

$$\rho_i \, v_i \times 10 \,, \, \text{lb/ft}^2 \text{-sec}$$

Figure 40.   Particle Mass Flux Distribution at h/d = 22 and Feeder
Setting at 100.

Figure 41. Particle Mass Flux Distribution at h/d = 22 and Feeder Setting at 50.
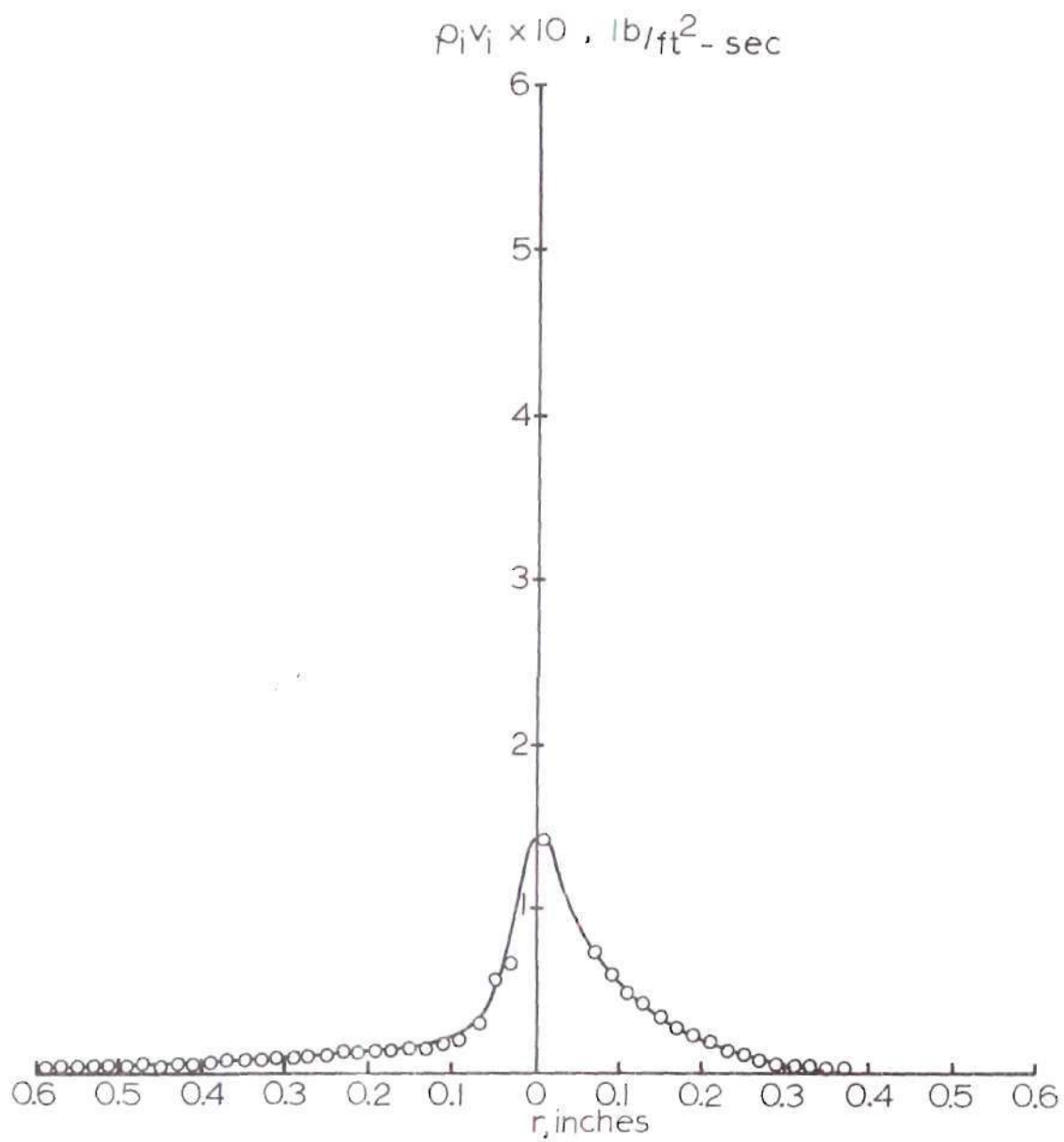
Figure 42. Particle Mass Flux Distribution at h/d = 22 and Feeder Setting at Zero.
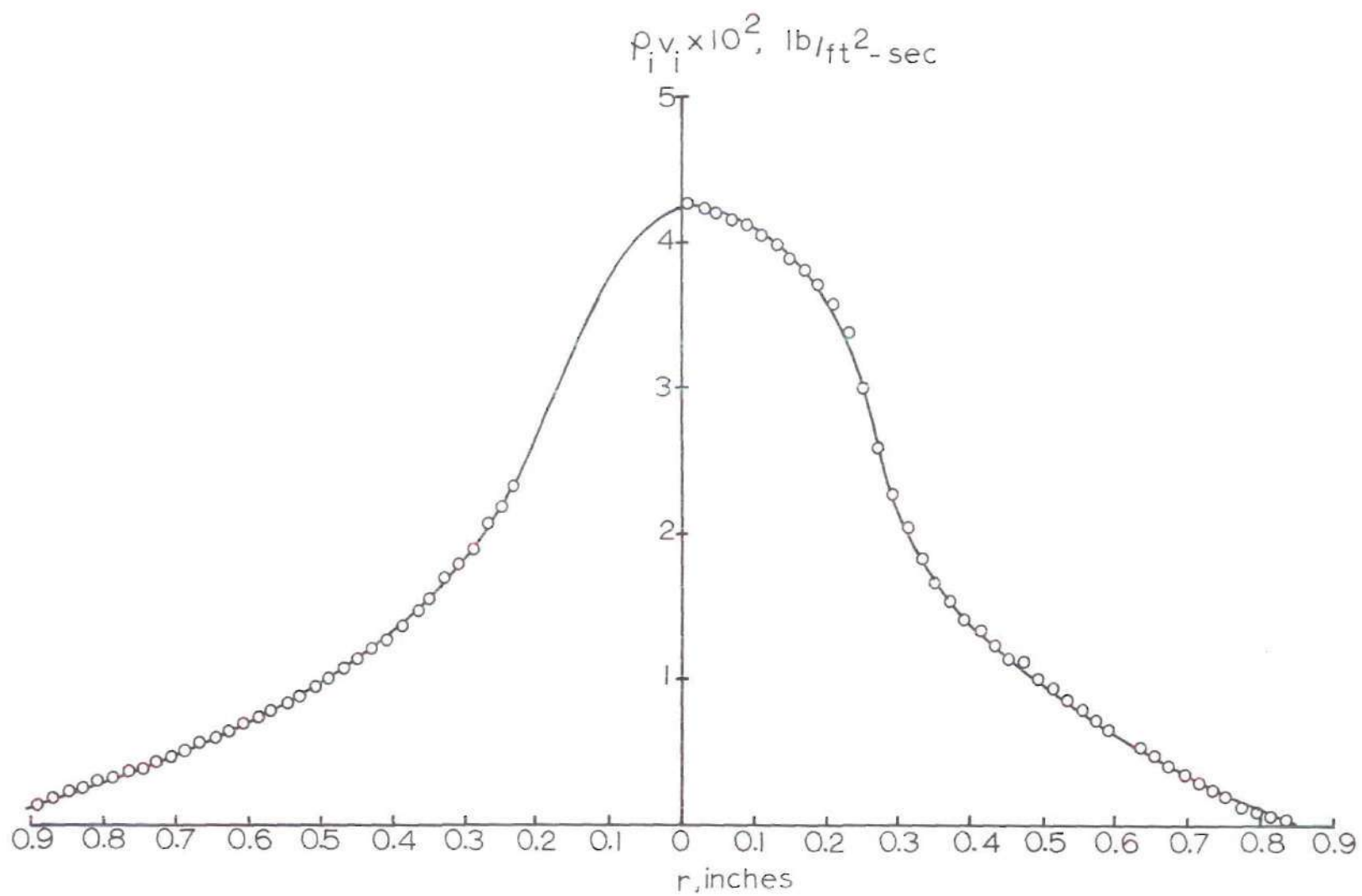
Figure 43. Particle Mass Flux Distribution at h/d = 72 and Feeder Setting at 50.
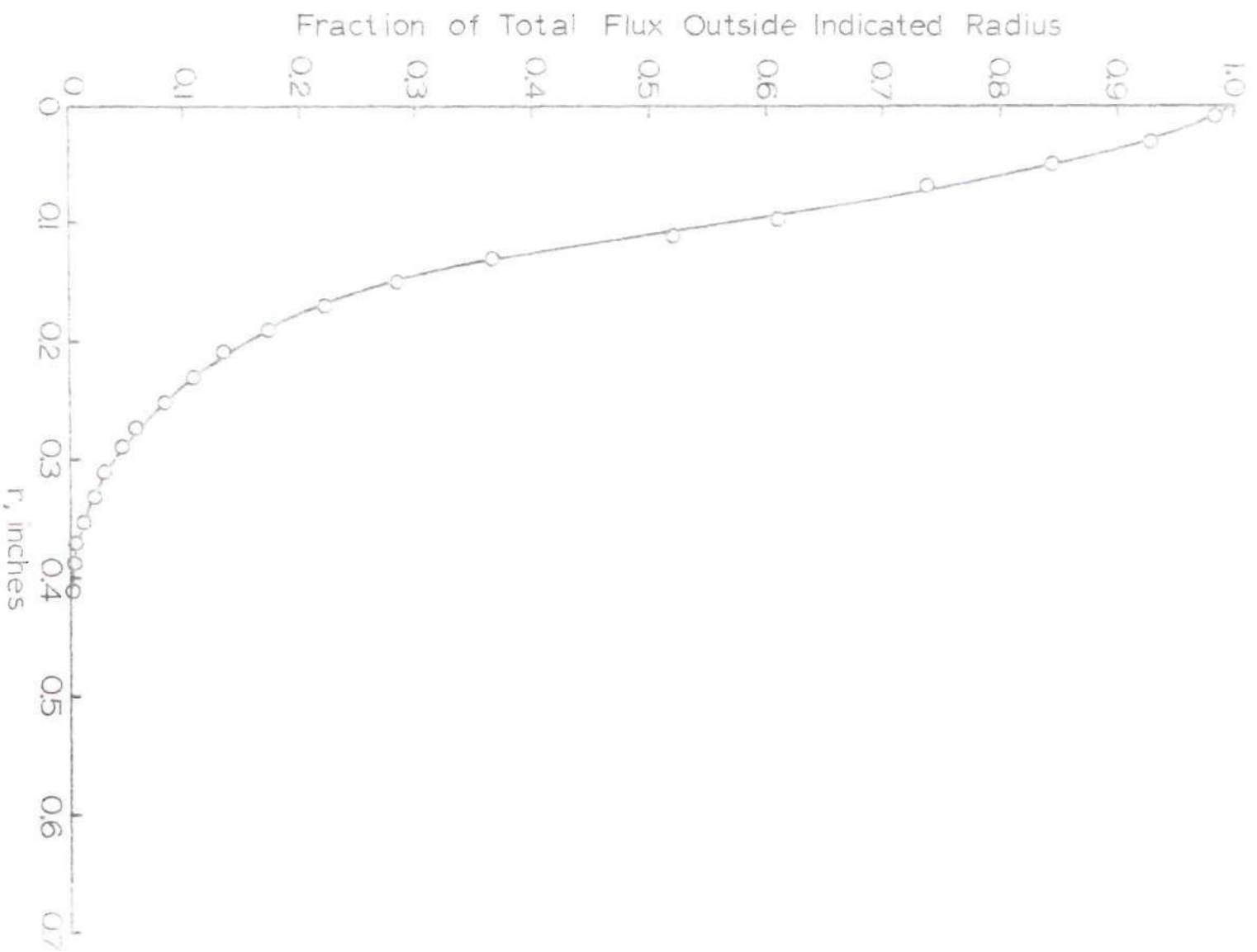
Figure 44. Aluminum Mass Flux Distribution at h/d = 22 and Feeder Setting at 100.
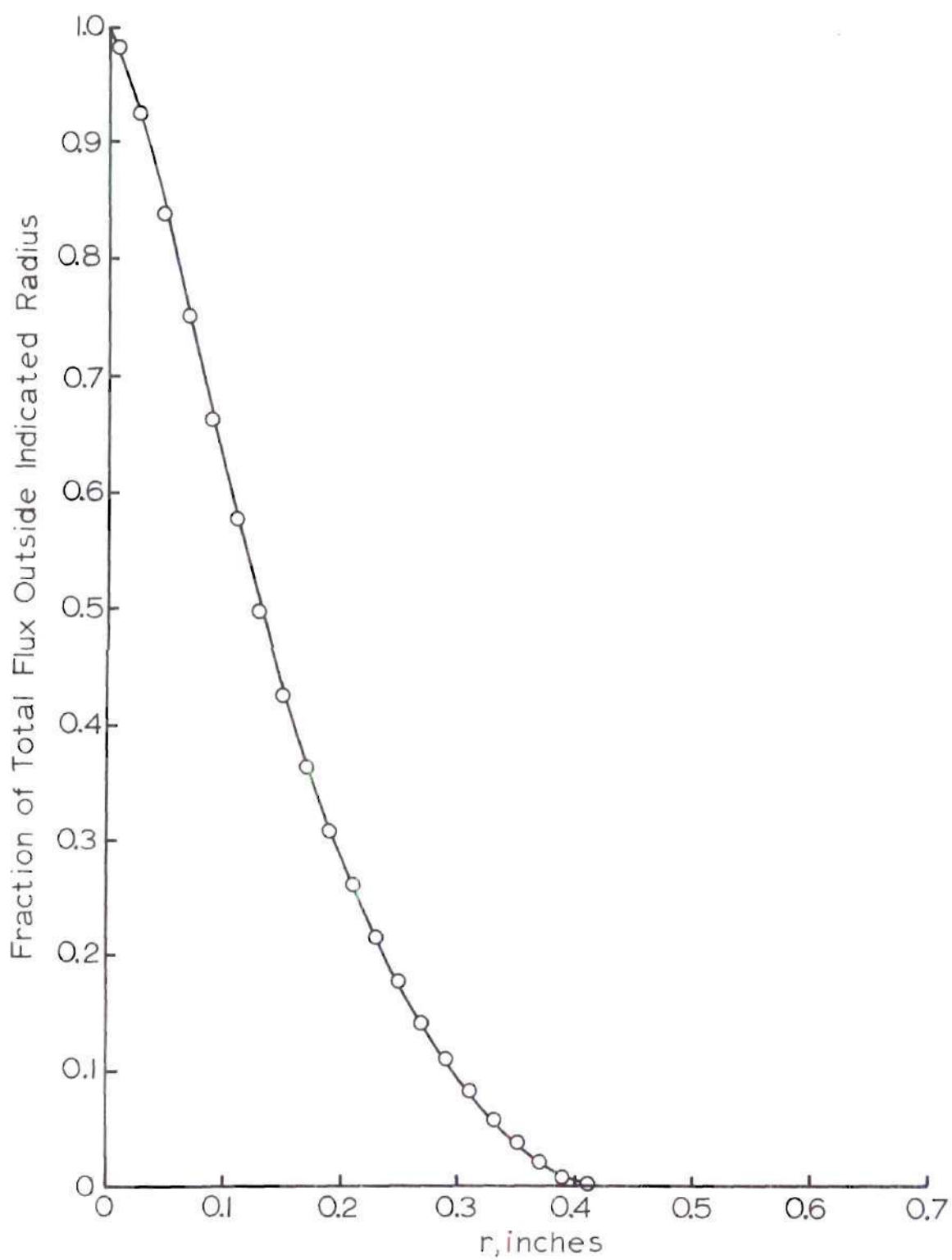
Figure 45. Aluminum Mass Flux Distribution at h/d = 22 and Feeder Setting at 50.
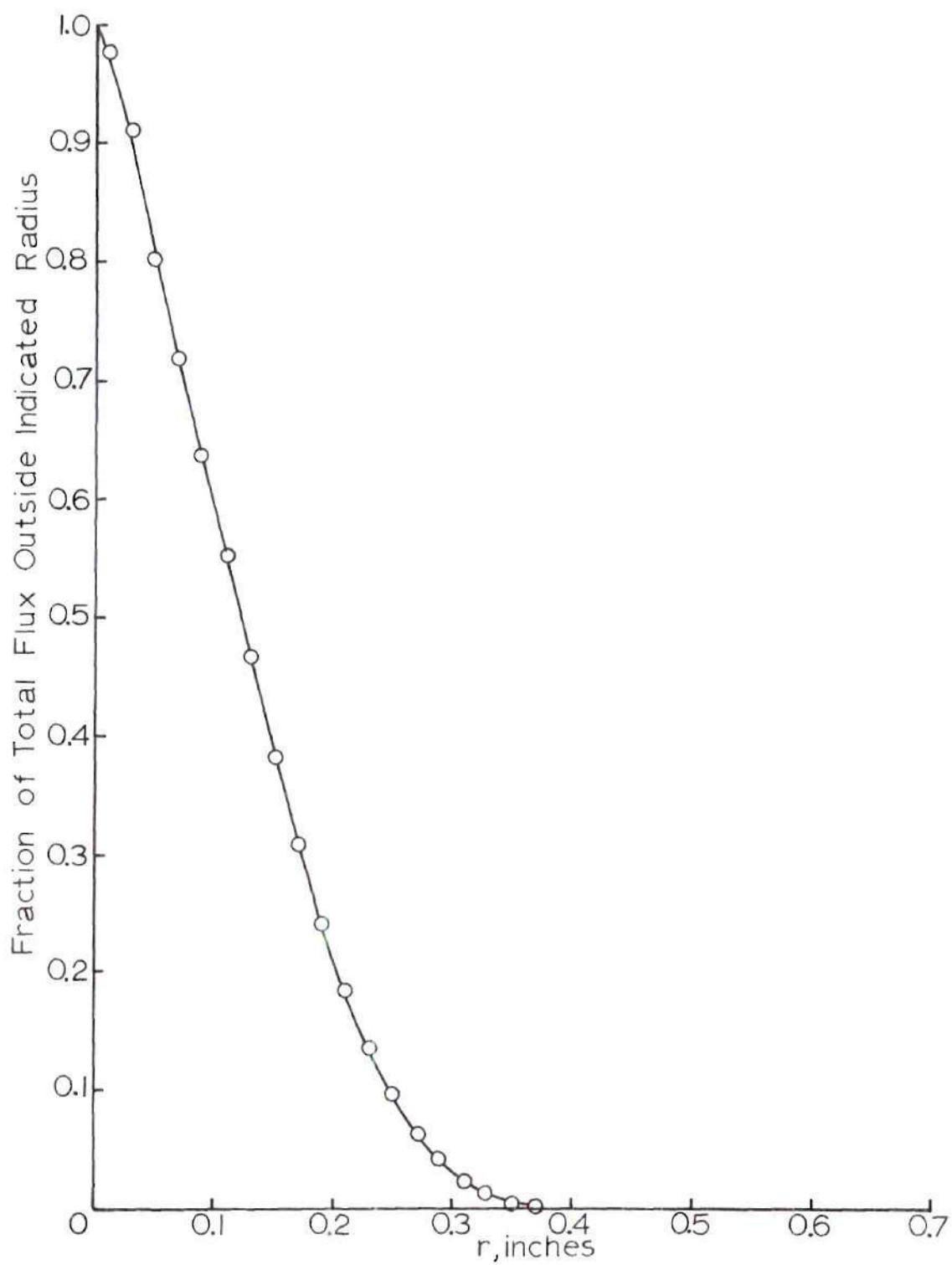
Figure 46.   Aluminum Mass Flux Distribution at h/d = 22 and Feeder
            Setting at Zero.
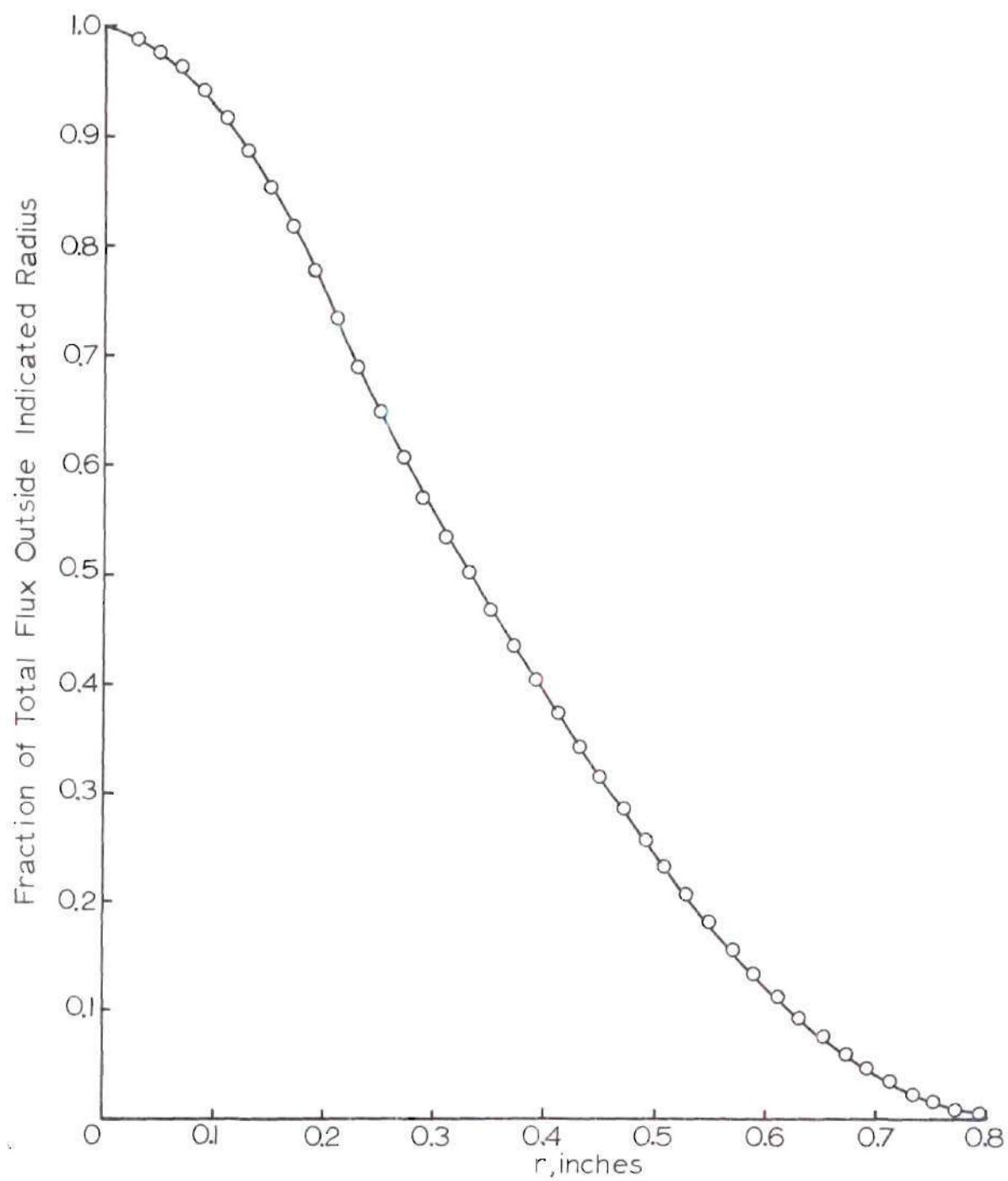
Figure 47.   Aluminum Mass Flux Distribution at h/d = 72 and Feeder
Setting at Zero.

a result of the depth of the field limitation of optical microscopes. At magnifications of 60X and lower, groups of particles can be identified, but the small, individual particles are not visible.

Photographs of samples at 60X on a boron nitride collector strip at distances of 0, 0.1, 0.2, 0.3 and 0.4 inches from the center and collected at H = 9", and with powder feeder setting at 50 are shown in Figures 46 and 49, pages 128 and 129. The large groups of particles can be readily identified in the photographs, but very little information concerning the individual particles can be obtained. However, comparison of the photographs showed the *decreasing amount of aluminum* on the strip as the distance from the center increased. Each division of the scale shown on each photograph represents 0.005 inches. It is evident that the particles are much smaller in diameter than 0.005 inches and many are grouped together in clusters.

A second series of photographs of aluminum particles and a boron nitride collector are shown in Figures 50, 51 and 52, pages 130, 131 and 132. These photographs were made with a scanning electron beam microscope at magnifications of 540X and 2300X. This type of microscopy is not limited by the depth of the field as is optical microscopy and the tiny aluminum particles are easily identified. Also, the diameters of the individual particles can be measured directly from the photographs. Figure 50, page 130 shows a typical group of particles adhering to the boron nitride surface at a magnification of 540X. The bonding of some of the particles to each other can be seen at this magnification. The smaller particles are probably spheres of Al_2O_3 which were formed during the combustion of an aluminum particle and suddenly quenched by impact

r = 0.3"
60 X
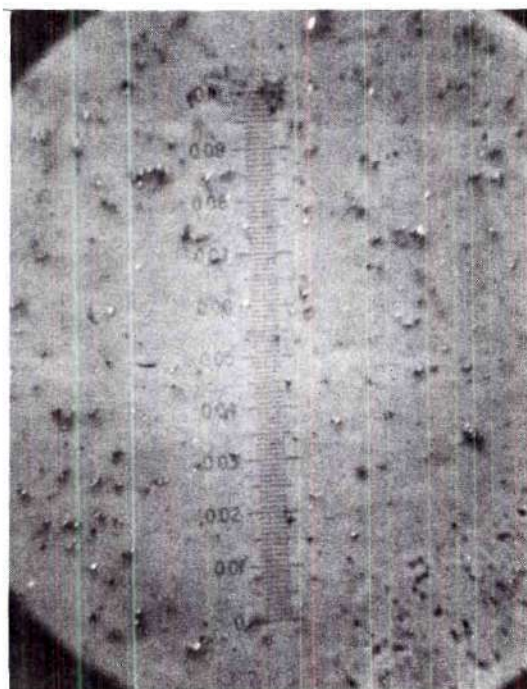
r = 0.4"
60 X

Figure 48. Particles Collected at h/d = 72 and Feeder Setting
at 50.

r = 0.0"
60 X
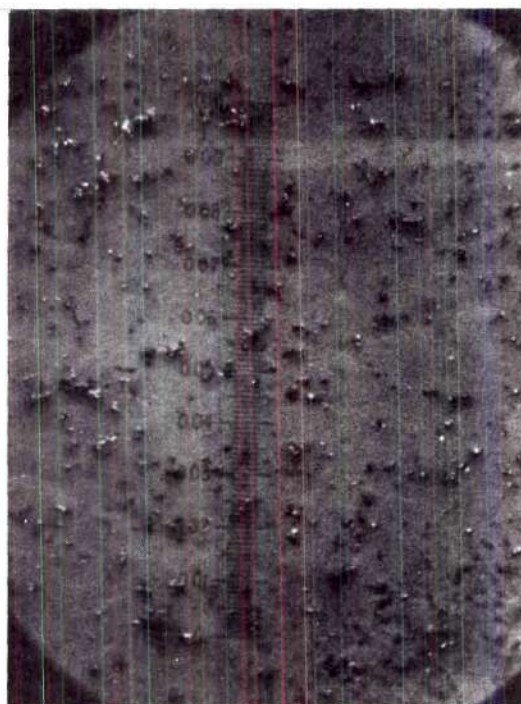
r = 0.1"
60 X

r = 0.2"
60 X

Figure 49.   Particles Collected at h/d = 72 and Feeder Setting
at 50.

540X

Figure 50.   Aluminum Particles on a Boron Nitride Collector Strip.
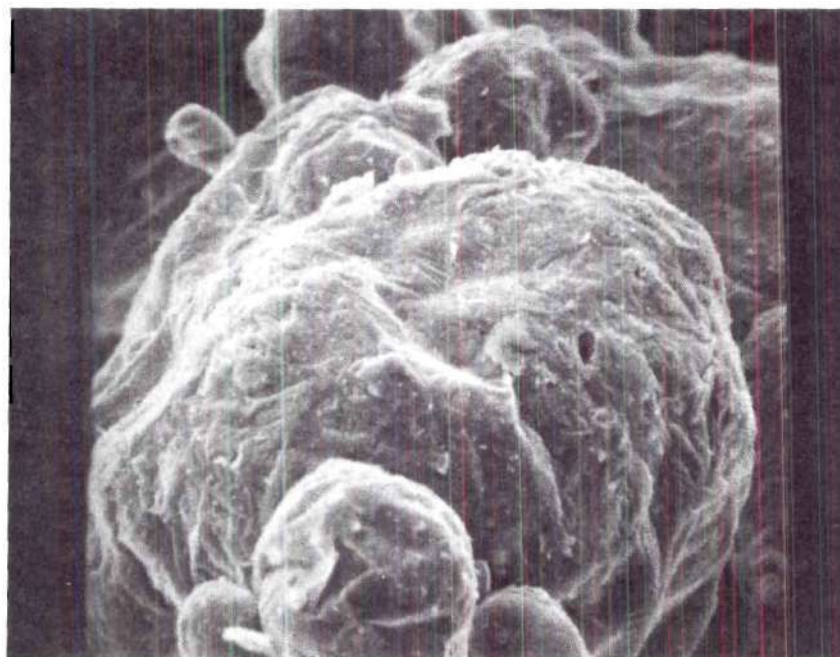
2300X

Figure 51.   Aluminum Particles on a Boron Nitride Collector Strip
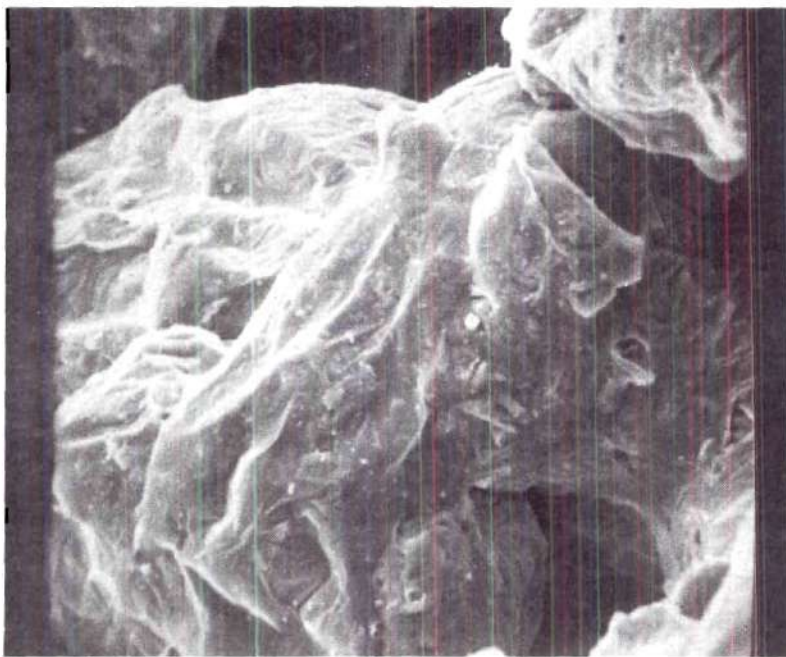
2300X

Figure 52. Two Aluminum Particles Bonded Together on a Boron
Nitride Collector Strip.

with the boron nitride strip. Figure 51, page 131 at 2300X shows a typi-
cal aluminum particle with three much smaller particles attached and
Figure 52, page 132 shows two aluminum particles at 2300X bonded together.
This bonding which can also be seen in the other two photographs was prob-
ably the result of an impact by a molten droplet, perhaps a burning drop-
let with accompanying Al_2O_3 particles.

Measurements of the diameters of the larger particles in the
photographs yielded particle diameters of approximately 35-40 microns.
This was smaller than the manufacturer's specification of 50 microns
average particle size, but of course the electron beam photographs
involved only a very limited number of particles and no representative
average could be obtained from them. For this reason an average par-
ticle size of 50 microns was used in the calculations.

The velocity distribution in the hydrogen flame at a position
h/d = 22 without entrained particles was presented in a previous sec-
tion. For the purpose of calculating the particle density distribution,
it was assumed that at this position in the flame the velocity of the
particles corresponded to the measured velocity of the gases at the
same location without particles.

In this case the particle velocity distribution corresponds to
the velocity profile given in Figure 15, page 69 in the section entitled
Velocity Measurements. The particle density distributions can be cal-
culated from the particle flux distributions and a value for the average
mass of a particle. The density of aluminum is 168.5 pounds per cubic
foot which means a 50 micron particle will weigh approximately 8.366 x
10^{-7} pounds. These values were used with particle flux data to produce

the particle density distribution curves given in Figures 53, 54, and 55,
pages 135, 136 and 137.
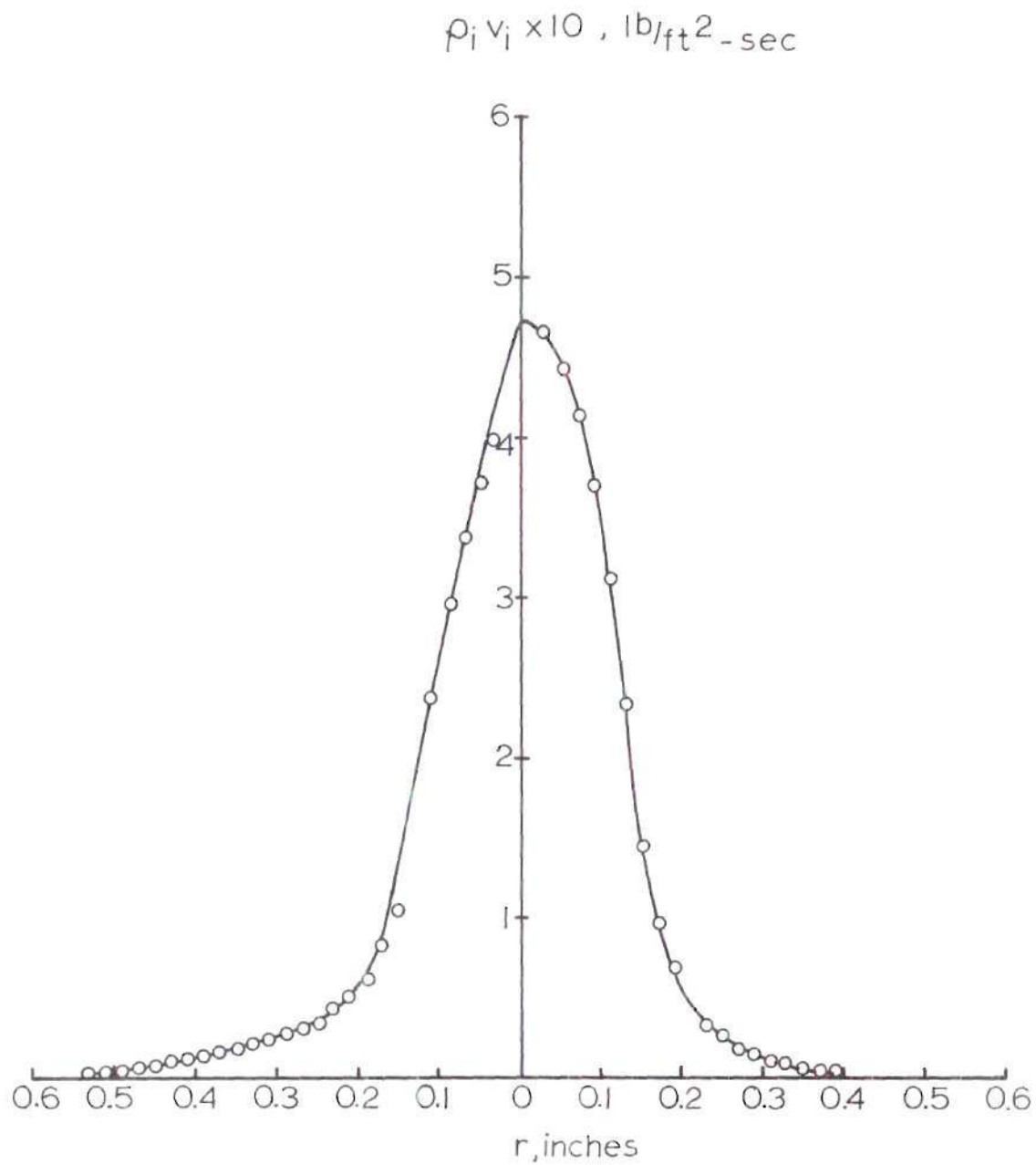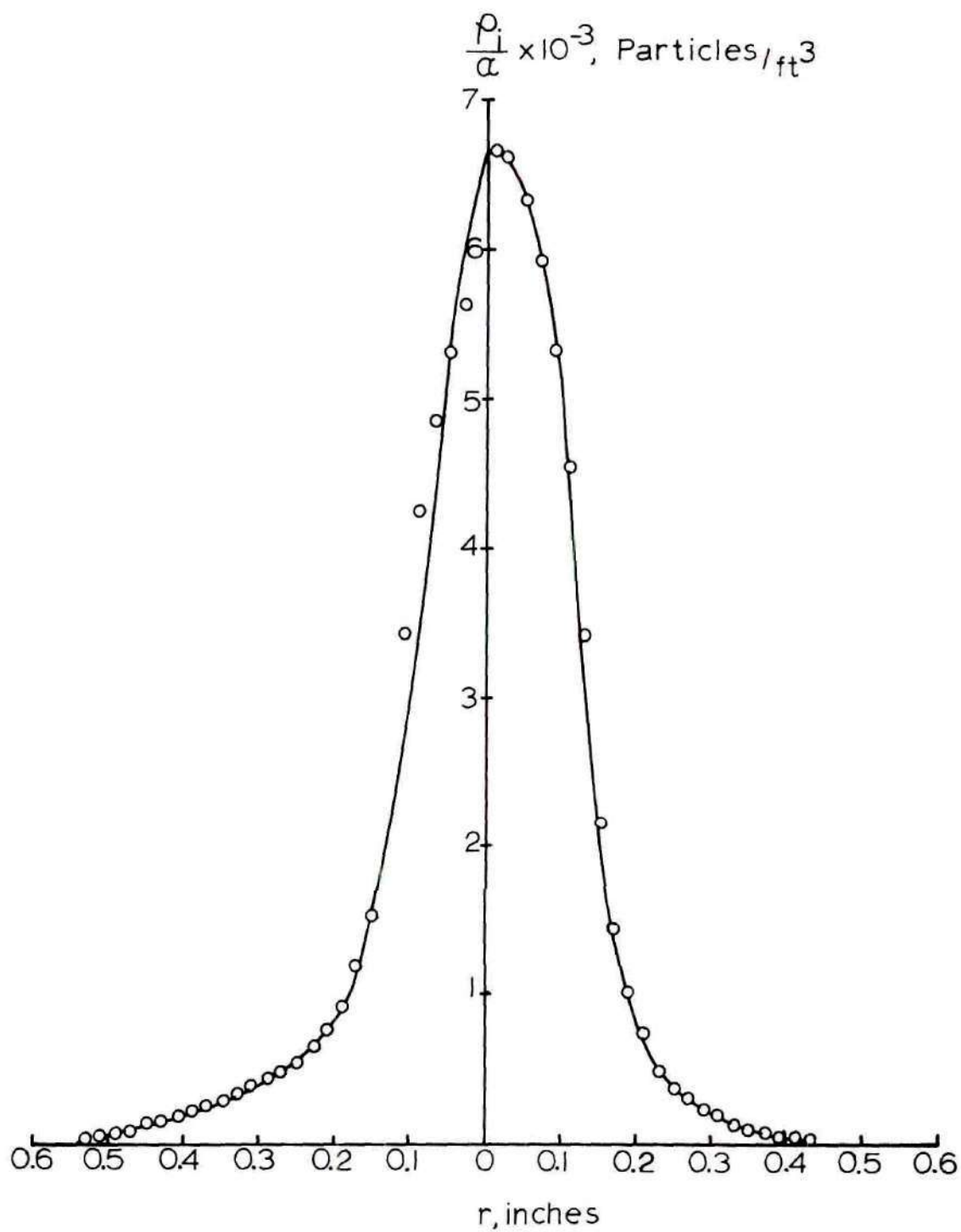
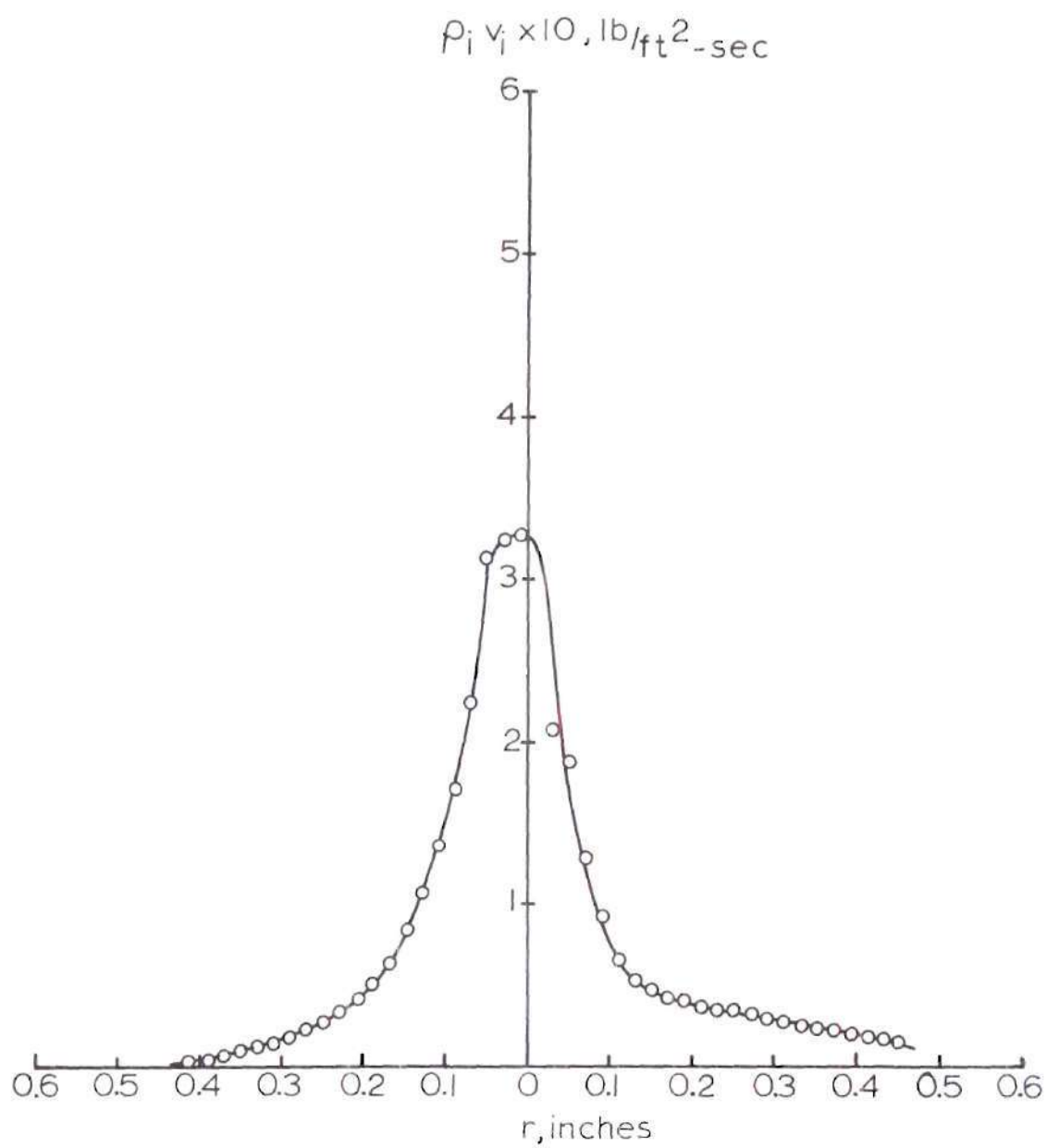Figure 53. Particle Density Distribution at h/d = 22 and Feeder
Setting at 100.
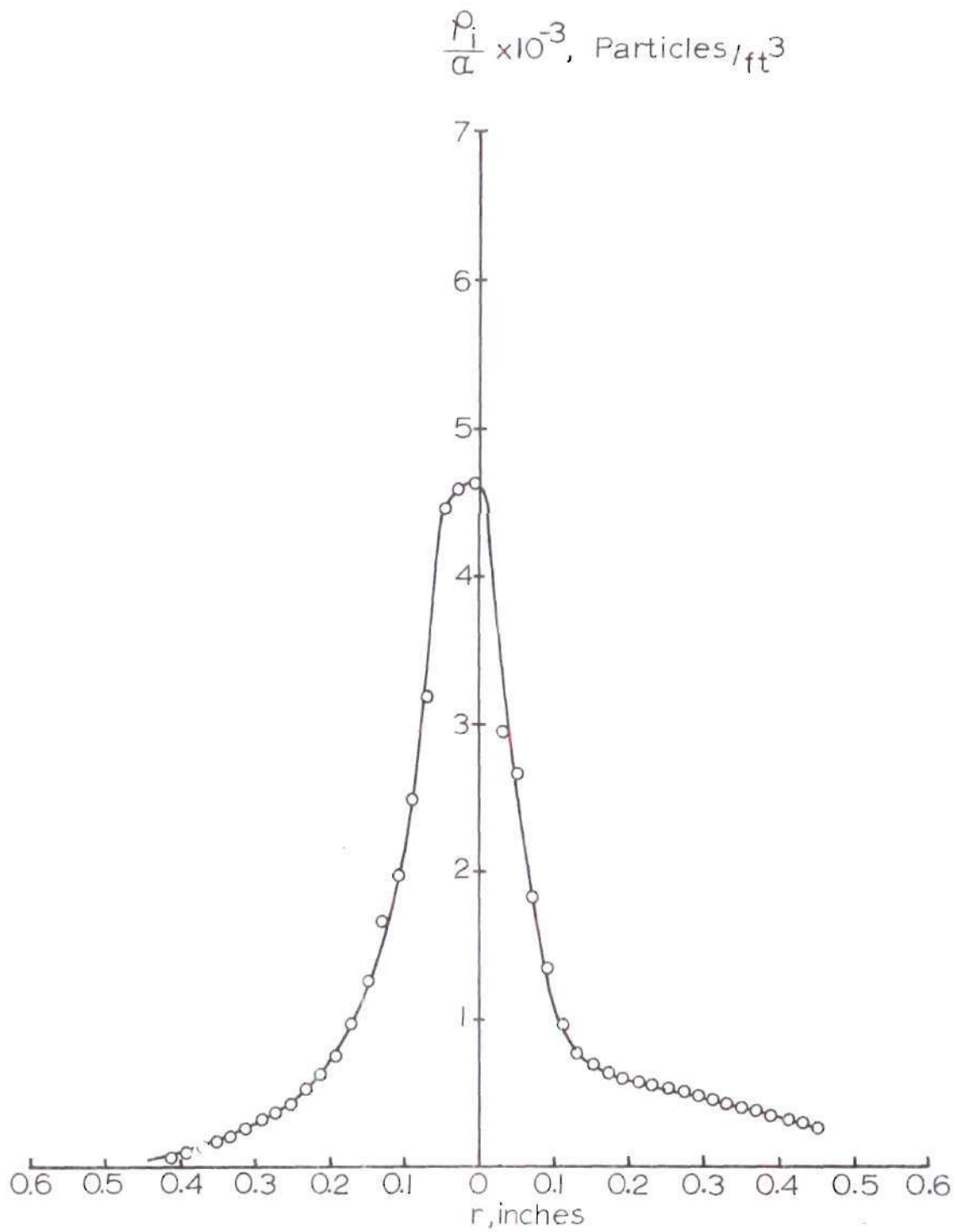
Figure 54. Particle Density Distribution at h/d = 22 and Feeder Setting at 50.
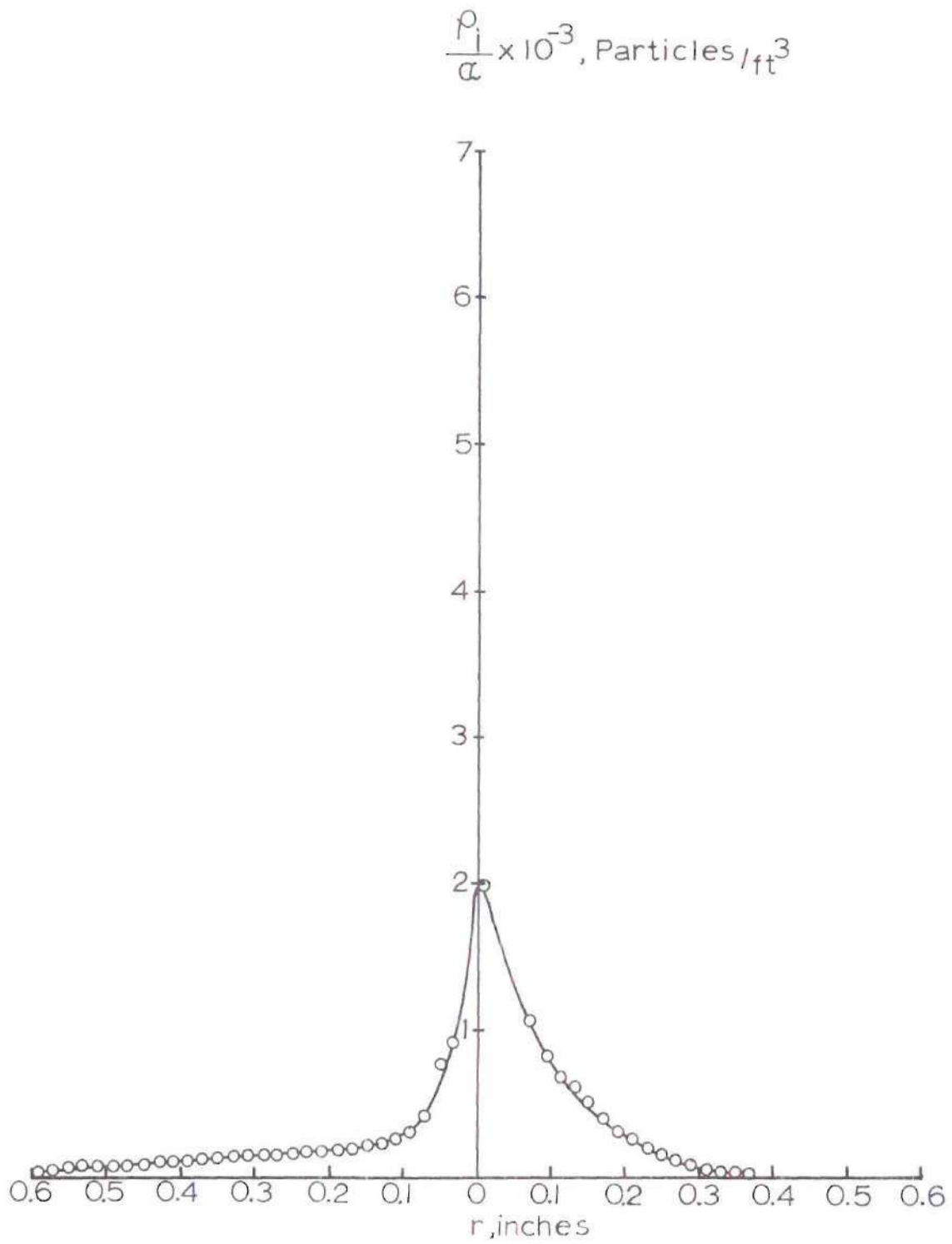
Figure 55.   Particle Density Distribution at h/d = 22 and Feeder Setting at Zero.

CHAPTER VI

ANALYSIS OF DATA AND DISCUSSION

Jet Mixing

The use of the measured data in the technique of fitting theo-
retical profiles is illustrated here by selecting $n = 2$ which corresponds
to Libby's theory (14) and using the transformed axial position variable,
ζ. In this way the general technique is illustrated and the measured
data compared with the theoretical treatment presented by Libby (14).
In addition, chemical equilibrium is assumed in the analysis so that the
calculated profiles have a reaction zone of finite thickness, that is,
a flame sheet model is not assumed.

The species concentrations were calculated for the turbulent
mixing problem using the equilibrium constant for the following reac-
tion:

$$H_2 + \tfrac{1}{2} O_2 \xrightleftharpoons{K_p} H_2O \qquad [G]$$
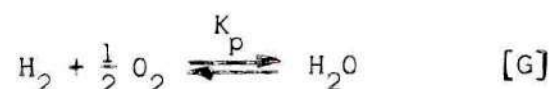
It was shown analytically that atomic hydrogen, the OH radical and
atomic oxygen were not present in significant amounts. Assuming the
gas to be a mixture of ideal gases the equilibrium constant may be
written in terms of mass fractions as

$$K_p = \frac{M_{H_2} M_{O_2}^{1/2}}{M_{H_2O}} \left[\frac{C_{H_2O}}{C_{H_2} C_{O_2}^{1/2}} \right] \qquad (6\text{-}1)$$

In terms of the non-dimensional parameter, $\tilde{\beta}$, the element mass fractions are expressed by

$$\bar{C}_H = 1 - \bar{\beta} \qquad (6\text{-}2)$$

$$\bar{C}_O = C_{O_{2_e}} \bar{\beta} \qquad (6\text{-}3)$$

$$\bar{C}_N = C_{N_{2_e}} \bar{\beta} \qquad (6\text{-}4)$$

The concentrations were determined for a given $\bar{\beta}$ by assuming a temperature, substituting for the element mass fraction corresponding expressions in terms of mass fractions and then solving equations (6-1), (6-2), (6-3) and (6-4) for the four concentrations. The enthalpy of the mixture was obtained using the following expression

$$h = \sum_i C_i h_i \qquad (6\text{-}5)$$

and compared with the enthalpy obtained from the relation

$$\bar{\beta} = \bar{H} = \frac{h - h_j}{h_e - h_j} \qquad (4\text{-}7)$$

This procedure was repeated for different temperatures until the assumed temperature gave the correct enthalpy. Using a range of values of $\bar{\beta}$ and selected values of $\frac{\zeta}{\psi_j}$ from the results presented by Masters (15), concentrations, enthalpies, and temperatures were determined for different non-dimensional axial positions in the flow.

It is pointed out that the physical axial location in the flow corresponding to these profiles has not been determined as yet. For the procedure presented here the measured species concentrations along the centerline were used to fit the theoretical curves and consequently, to fix the relationship between ζ and z. Once this was done the measured concentration profile at one value of ζ was used to determine the relation between ψ and r. Thus, the solution for the entire flow was determined by a match between concentration data along the centerline and theory, and a match between concentration data at various radial positions at one particular axial location and theory.

The centerline data match determined the h/d = 22 axial location to be at

$$\frac{\zeta}{\psi_j} = 1.074$$

The variation of $\bar{\beta}$ with ψ/ψ_j and the corresponding values of r/r_0 are given in Figure 56, page 141. The resulting relationship between ψ/ψ_j and r/r_0 is given in Figure 57, page 142, based on the measured concentrations and the theoretical profile corresponding to the value of ζ/ψ_j above. Calculated temperature profiles are given in Figures 58 through 62, pages 143 through 147 for different values of ζ/ψ_j. The required variation of $(\rho u/\rho_j u_j)$ to fit the radial concentration measurements and theory for the above value of ζ/ψ_j is given in Figure 63, page 148.

Figures 16 through 23, pages 71 through 78 show the experimentally determined temperature profiles. These should be compared to
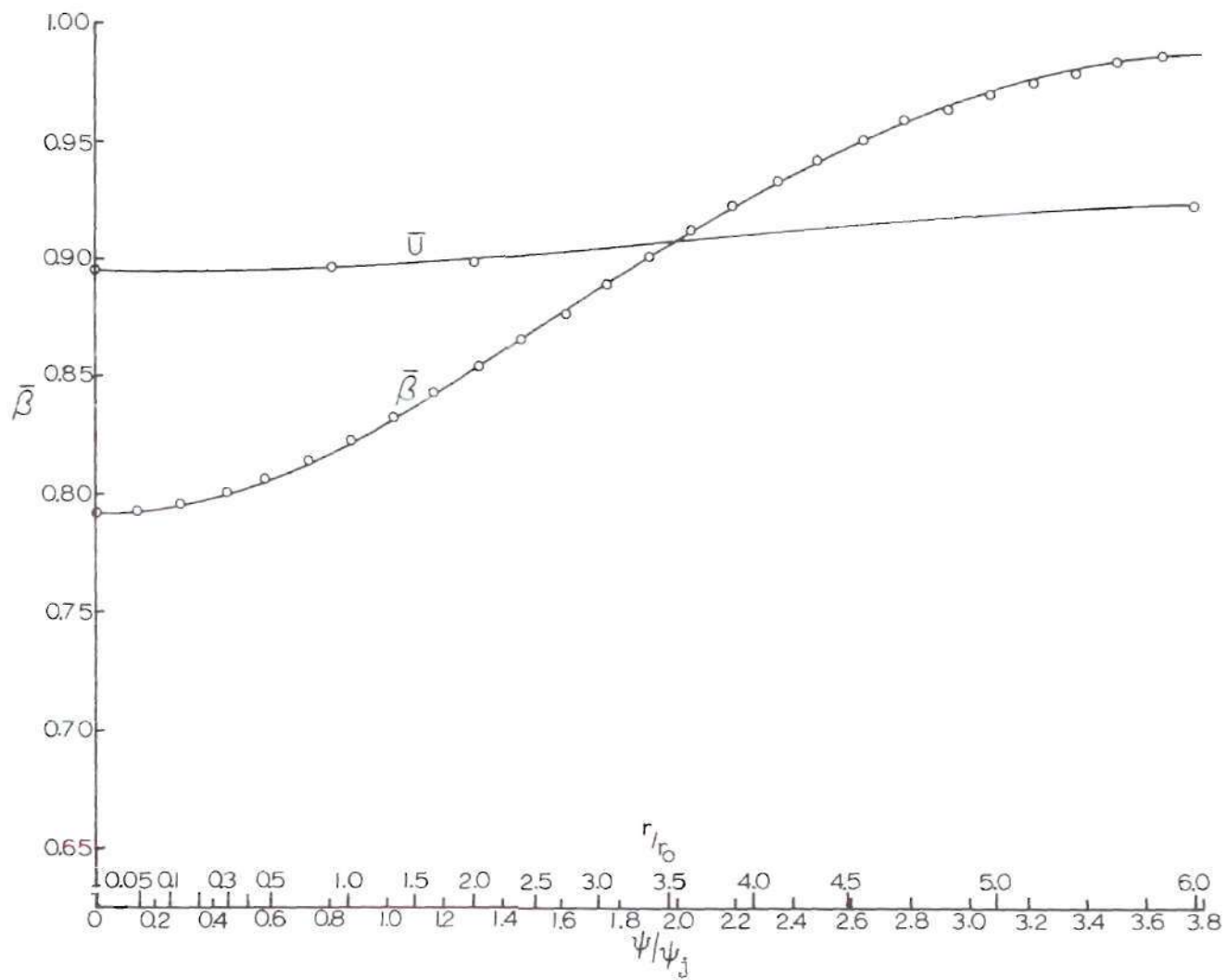
Figure 56. Radial Variation of $\bar{\beta}$ for $\zeta/\psi_j = 1.074$
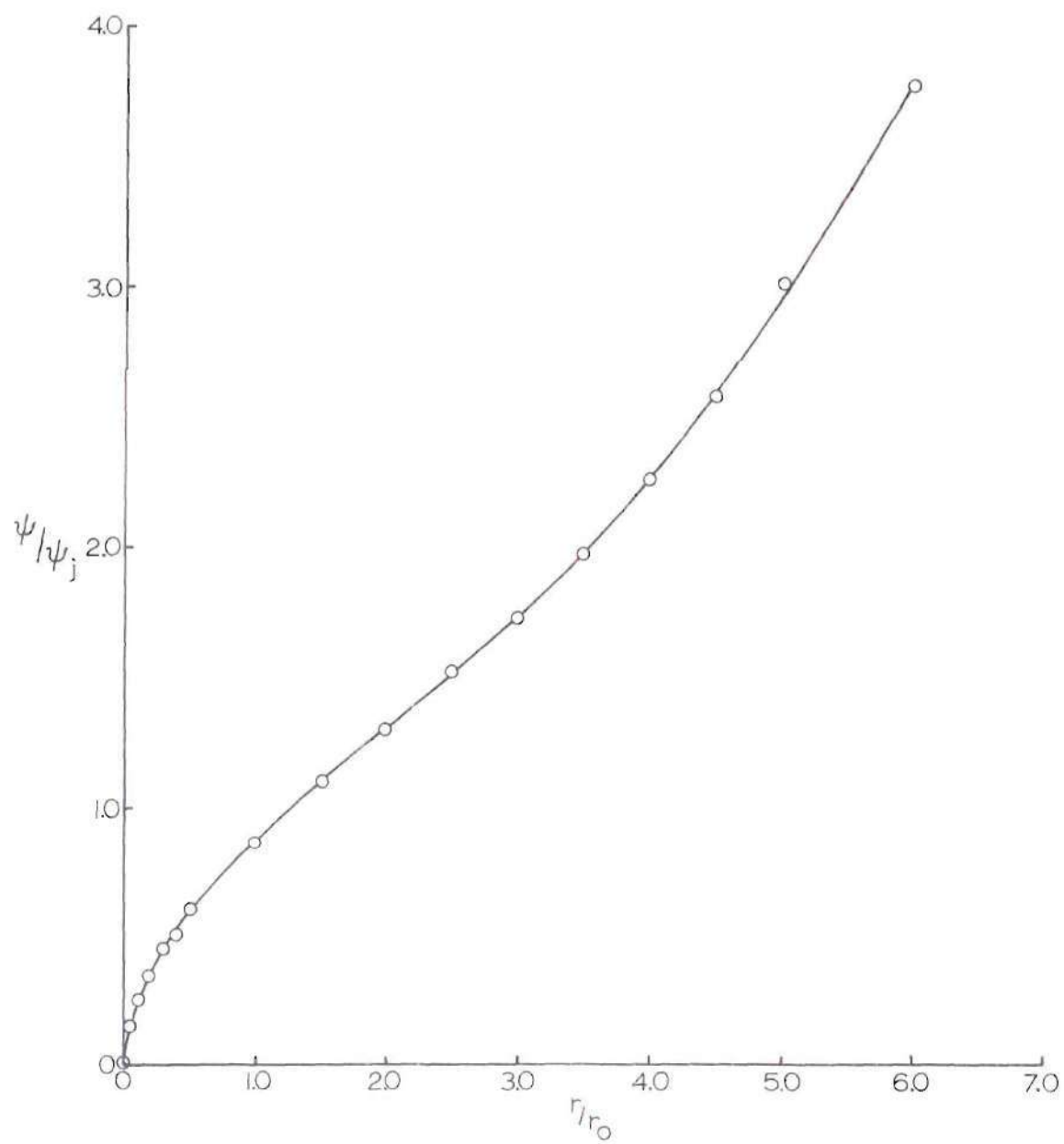
Figure 57. Relation Between ψ / ψ_j and r/r_o for $\zeta / \psi_j = 1.074$
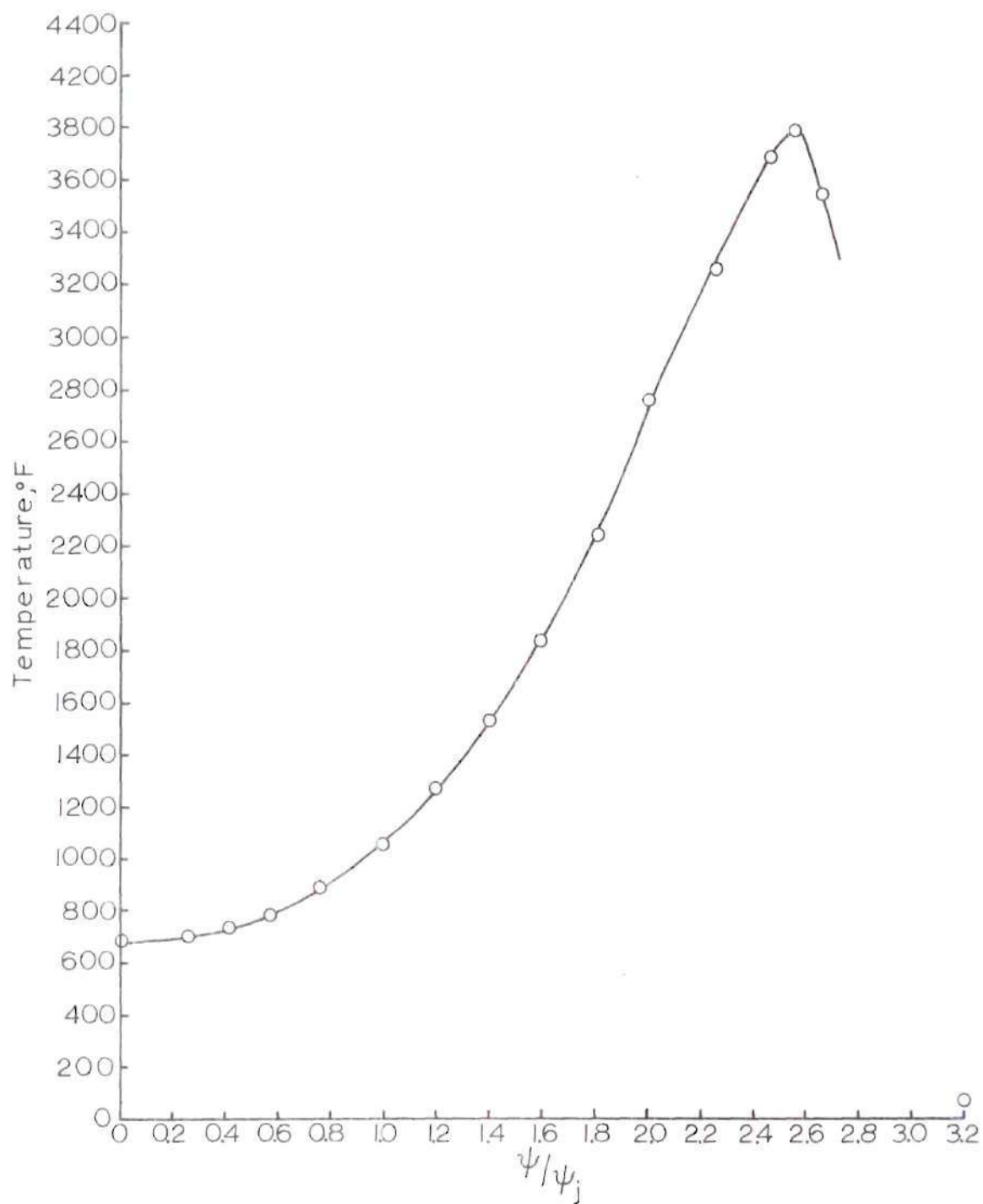
Figure 58. Calculated Temperature Profile for $\zeta/\psi_j = 0.5$
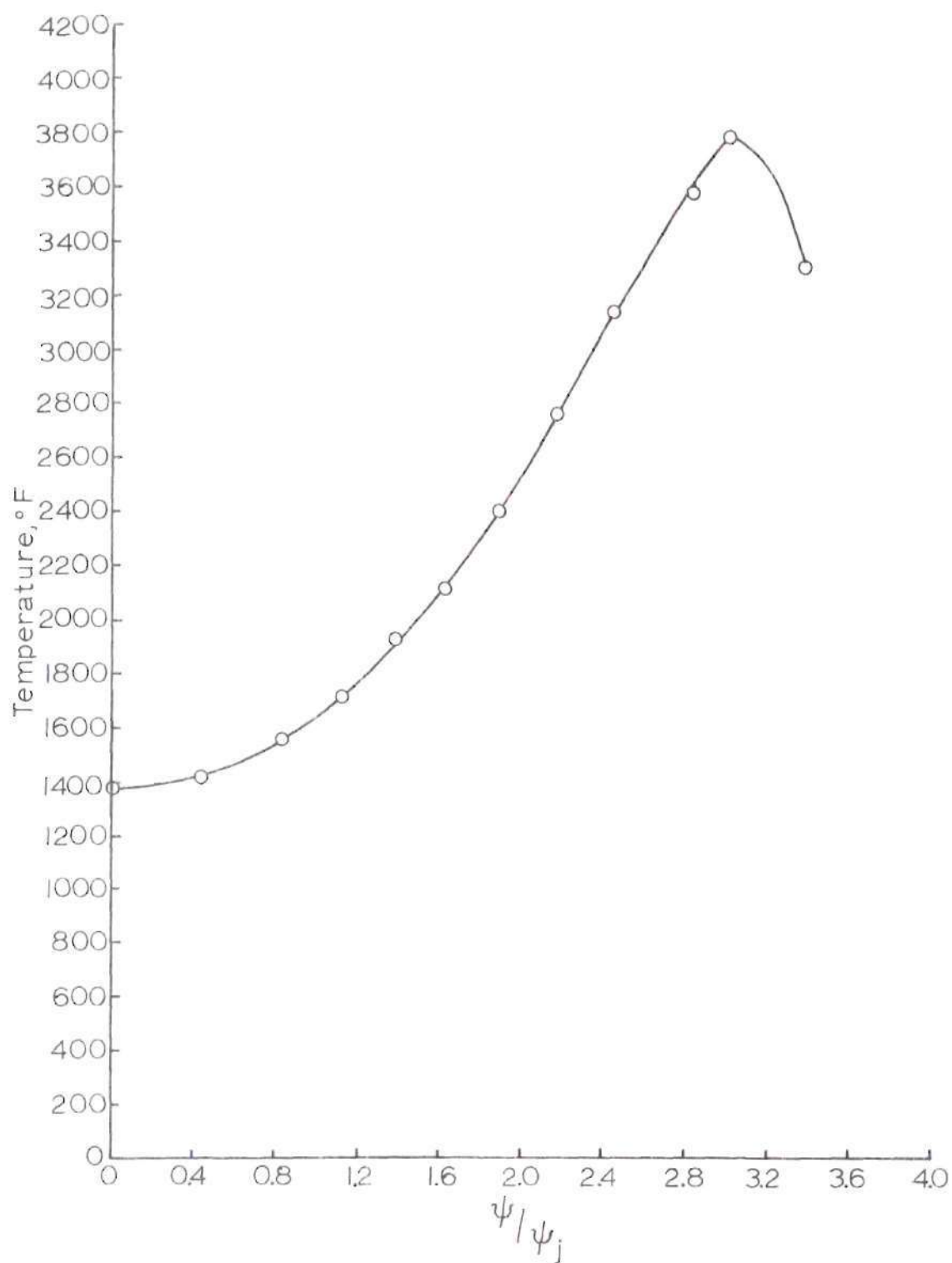
Figure 59. Calculated Temperature Profile for $\zeta/\psi_j = 1.074$
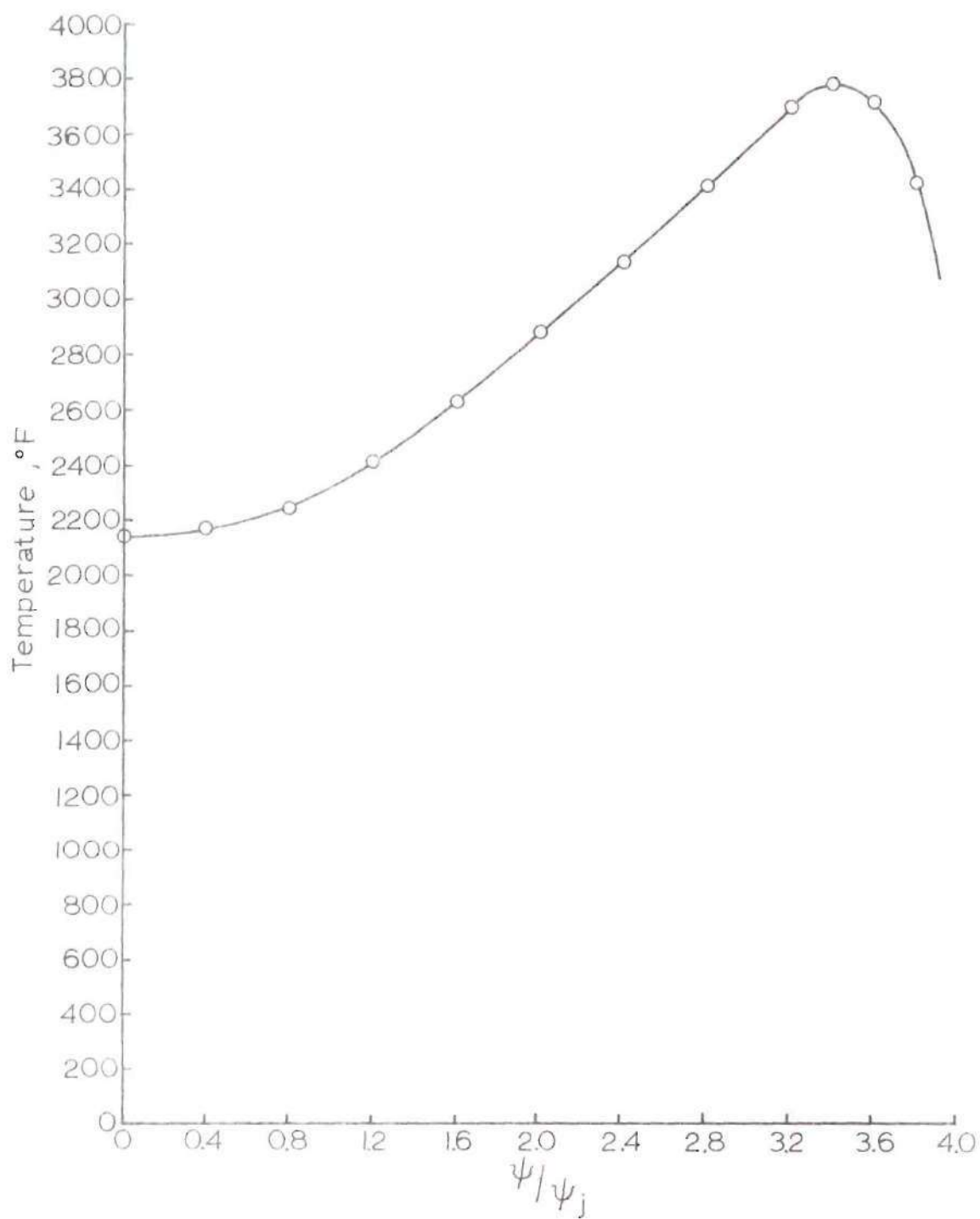
Figure 60.   Calculated Temperature Profile for $\zeta/\psi_j = 2.0$
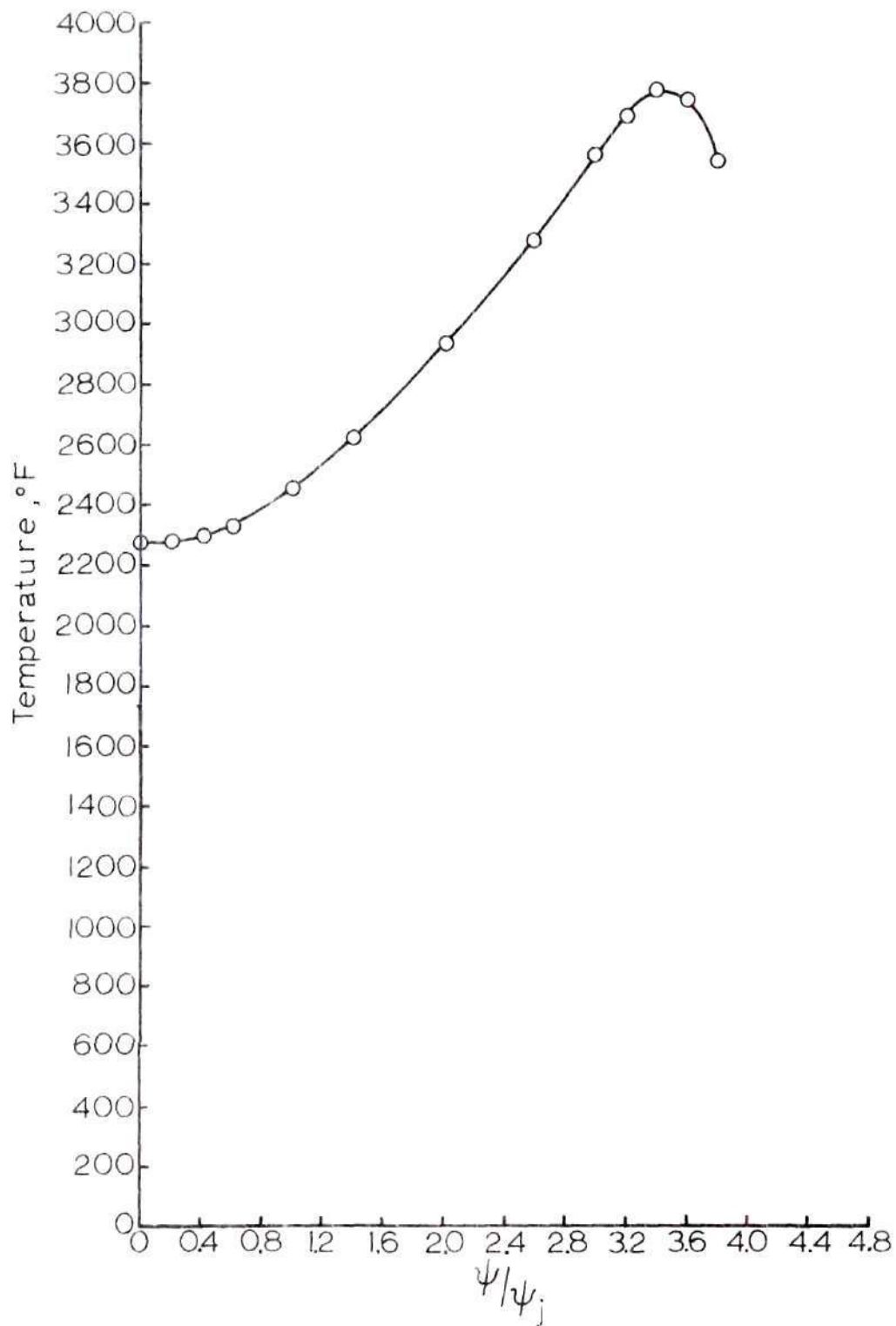
Figure 61. Calculated Temperature Profile for ζ / ψ_j = 2.2
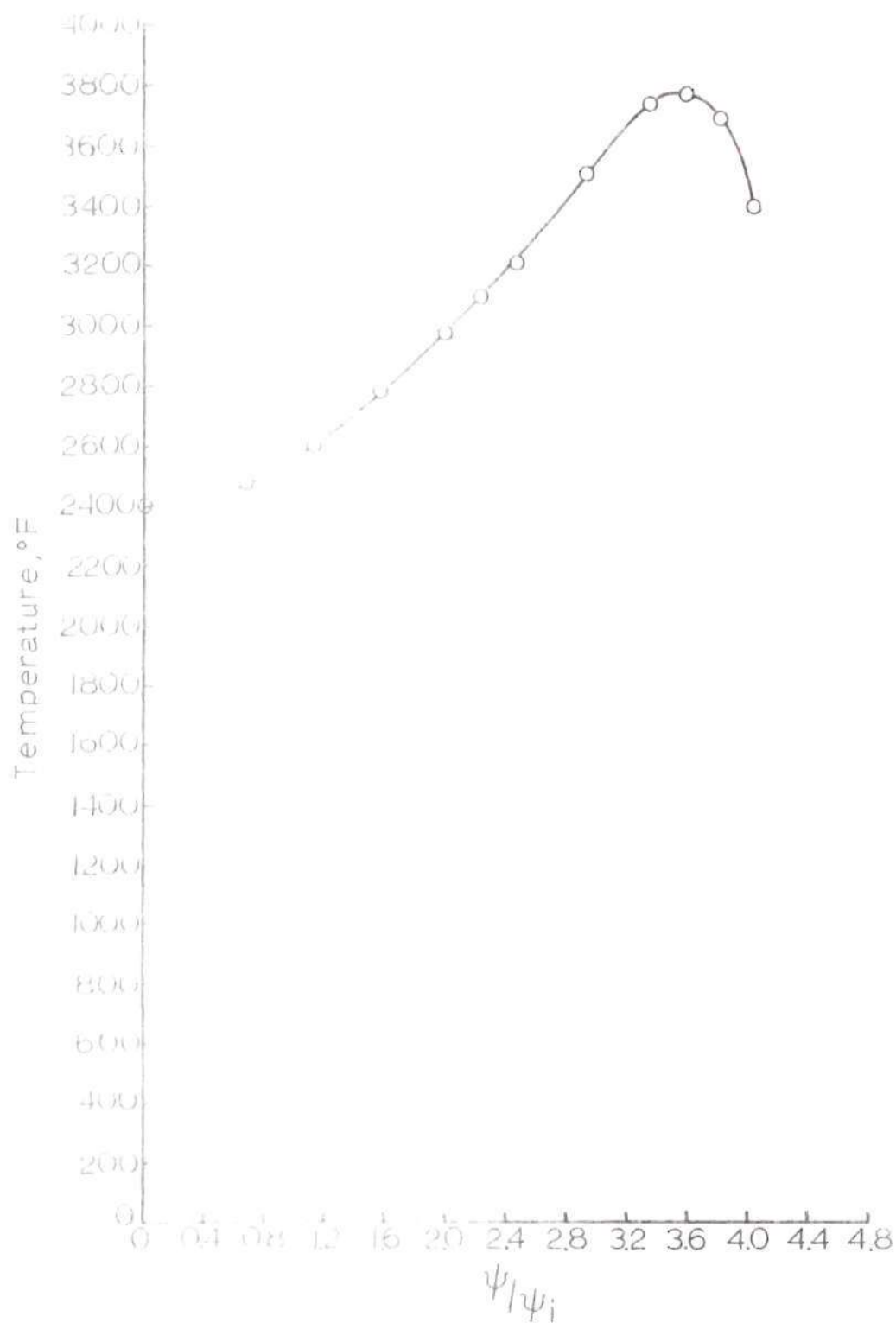
Figure 6. Calculated Temperature Profile for $\zeta/\psi_j = 2.5$
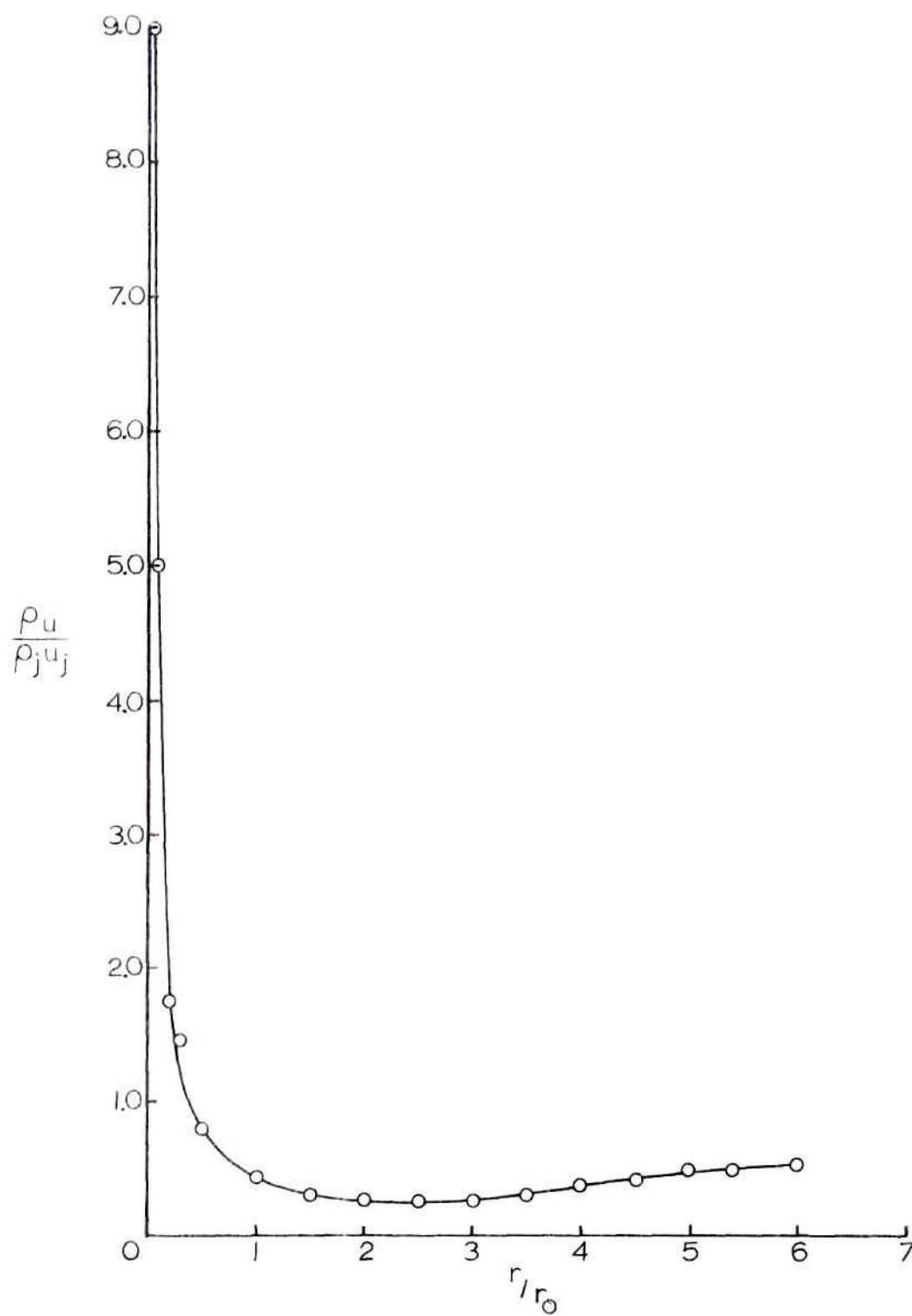
Figure 63. Radial Variation of $\rho u / \rho_j u_j$ for $\zeta / \psi_j = 1.074$

the theoretical profiles given in Figures 58 through 62, pages 143 through 147. Considering the fact that the theoretical curves were matched with concentration data one might expect a fairly good agreement with temperature comparisons. A significant difference exists, however, between the corrected experimental values and theoretical predictions. Generally the predicted centerline temperatures are low and the predicted reaction envelope temperature is high. This may imply that a significant quantity of energy is transferred from the reaction envelope region to the central core, lowering the temperature of the reacting region and raising the temperatures near the centerline. This is also supported by the observation that the measured reaction zone temperatures in the flame increased with increasing axial positions. In other words the energy transferred was higher at positions where the jet diameter was smaller and contained a larger fraction of hydrogen. This trend supports the data obtained in the hydrocarbon-air jet studies of Chervinsky and Manheimer-Timnat (24).

The velocity profile shown in Figure 15, page 69 was converted to values of $\bar{U}$ and plotted in Figure 56, page 141 with values of $\bar{\beta}$ determined from concentrations as previously discussed. The analysis implies that similar solutions exist for this flow, and thus $\bar{\beta}$ should equal $\bar{U}$. A comparison of these two parameters in Figure 56, page 141 shows a large difference.

In view of the differences noted in theory and experiment it appears that some other technique is needed for treating the turbulent mixing problem. It was pointed out in the earlier presentation of the theory that a free parameter, n, used as an exponent of the stream

function results in families of solutions and that the effect of changing the value of n was to make the profiles flatter or sharper. Tabulated solutions for values of n not equal to one, two or three are not available. These are needed to evaluate this approach. It is pointed out, however, that the addition of the free parameter, n, to the general technique insures a better match between theory and experiment.

Hydrogen-Air Flame with Entrained Particles

The turbulent mixing controlled, hydrogen-air flame was very long and slender. The flame without particles was essentially non-luminous and exhibited the usual characteristics associated with turbulent flames. The addition of combustible particles changed the flame to a very bright flame which was characteristic of aluminum combustion. Visual observations and high speed photographs showed that the particles ignite on crossing the flame envelope and burn brightly as they move upward with the flow. Viewed from the side the region of particle ignition was clearly visible appearing as a bright, nearly vertical line on either side of the jet. This can be seen in the photographs shown in Figure 1, page 3.

The most unusual aspect of the flame occurred with the higher particle flow rates. This can be seen in the photographs as the very bright region at the top of the flame. This region also represents an increase in the flame length over the length without particles. The region probably results from the ignition of particles at the flame tip region where the oxygen concentration may be quite low for some distance. In this case the particles burn in an environment which is low in oxygen. The particle burning times will be significantly

increased due to the effect of combustion of adjacent particles in insufficient oxygen (36). It is also possible that in this region the water vapor reacts with the aluminum. However, the aluminum wire combustion tests in water vapor-oxygen mixtures (49) gave essentially identical results with dry mixtures.

Particle Distribution

A technique for sampling particles entrained in the flow and determining from the collected sample the particle density was developed in this study. The method of determining the amount of aluminum on the collector, neutron activation analysis, avoided the difficulties resulting from the fact that some of the particles were burned or burning when they were collected. The results depend, however, on the assumption that all the particles which passed through the flame area blocked by the collector collided with and adhered to the collector strip.

The general technique appears not to have been used before in the study of metal combustion in gas streams and based on the results obtained in the study may prove to be a useful technique. It is further noted that the technique using very small, uniform particles might be used to measure gas-phase velocity distributions as well.

The aluminum distribution on the collector strip samples are shown in Figures 36, 37, 38, and 39 pages 113, 114, 115 and 116. The actual measurements are represented by the bar graphs and the distribution curve was drawn in to match the average values measured over the strip segments which were 0.1 inches wide. The peak was assumed to lie on the centerline of the jet. This probably represents the weakest part

of the technique. It is noted, however, that the collector strip could be divided into very small segments and the aluminum peak determined with better accuracy. Also, a device could be constructed which would position the collector strip in a predetermined position in the flow so that the centerline position was known precisely.

The aluminum mass flux distributions across the flame are presented in Figures 40, 41, 42 and 43, pages 119, 120, 121 and 122. A comparison of the first three of these curves shows that increasing the number of particles entrained in the flow has practically no effect on the aluminum flux distribution across the flame at least for the range of variables used in this study. The rate at which the particles spread, including any effects of particle combustion, may be obtained by comparing Figure 41 and 43, page 120 and 122. These curves are the aluminum flux distributions at $h/d = 22$ and $h/d = 72$ for a total particle mass flux of 5.55×10^{-5} lb/sec.

The data presented on mass flux do not assume a particle size distribution or a velocity distribution. To obtain an aluminum particle density distribution in the flame the particle-size distribution must be known. The aluminum particles used in this study had a size distribution such that the average particle was 50 microns in diameter. The particles were assumed to have a velocity profile corresponding to the measured gas velocities for the same gas flow rates. The particle densities shown in Figures 53, 54 and 55, pages 135, 136 and 137 were determined with the above assumptions. It was noted that the measured gas velocity profile changed very little over the region of particle flux so that the particle density determination at worst would change

by a constant factor. If desired the difference between the particle velocity and the gas velocity may be approximated by the method of reference (34). A particle velocity profile may be calculated from experimental data on the gas velocities and the calculated solid particle-gas velocity difference. In any case the particle velocities were between the hydrogen jet velocity at 550 ft/sec and the measured gas velocity of approximately 89 ft/sec at h/d = 22. Approximations of the particle velocities by the method of reference (34) indicated the particle velocities are closer to the hydrogen jet velocity. Assuming the particles did not slow down between h/d = 0 and h/d = 22 the particle densities would be given by multiplying all the points in the above three figures by a constant, 0.162.

Particle Combustion

The aluminum combustion model used in this study was based on the assumption that liquid Al_2O_3 forms as small particles at a distance from the particle surface. The analysis applies only to the vapor-phase, diffusion-controlled combustion of an aluminum particle. The maximum temperature of the flame structure of a particle burning in air was calculated to be 4180°F and the aluminum temperature to be 3500°F, well below the boiling point of aluminum. These values are in reasonable agreement with reported values (46, 47).

The primary gaseous species at the surface were determined to be N_2, Al_2O and Al. The concentrations of O, O_2 and AlO were very low at the surface. Figure 11, page 57 shows that the equilibrium composition shifts to Al_2O_2 at increasing distances from the surface and that

Al_2O_2 reaches a maximum at a position approximately twice the particle radius.

The criterion for the formation of liquid Al_2O_3 was applied to the calculated gas compositions and temperatures starting at the particle surface and proceeding outward. The first position at which the following relation was not satisfied

$$K_p < \frac{1}{p_{O_2}^{3/2} p_{Al}^2}$$

was located at

$$\frac{r_s}{r} = 0.929$$

Based on the assumptions made in formulating the combustion model it was not possible for liquid Al_2O_3 to form at positions closer to the surface than this value. It is pointed out, however, that if kinetics play a role the position of Al_2O_3 formation might be at a much greater distance from the surface.

CHAPTER VII

CONCLUSIONS AND RECOMMENDATIONS

Experimental and theoretical investigations of turbulent mixing of chemically reacting jets and the combustion of entrained aluminum particles has been made. The theoretical study treated the concentric jet geometry with a uniform fuel jet at the center issuing parallel into an infinite air stream at a uniform velocity. The analysis represents an extension of Libby's theoretical treatment of the problem. It was shown that a free parameter, n, may be used as an exponent on the stream function and still identically satisfy the continuity equation and transform the momentum equation and boundary conditions into a form which has families of solutions depending on the particular value of n. The treatment may be further sophisticated by assuming the term containing the eddy viscosity to be a constant or a function of axial position. The latter case with n = 2 corresponds to Libby's solution.

Experimental measurements were made on the hydrogen-air flame. Data on velocity, temperature and chemical species were obtained. This work appears to be one of the few studies which reports velocity, temperature and chemical species distribution for this type of flow.

Libby's theory was matched with concentration data along the centerline and in the radial direction at a height of h/d = 22. The predicted temperatures, concentrations and velocities were obtained and compared with the data. Generally, a poor agreement between theory and

experiment resulted. The comparison indicated that similarity, for n = 2, did not exist throughout the gaseous flow region. A criterion for the formation of liquid Al_2O_3 was presented and the position located within the flame structure where this criterion would predict the formation of Al_2O_3. The predicted flame and surface temperatures and burning rates are in reasonable agreement with experimental data. However, it is noted that order of magnitude variations of reported burning rates are not unusual.

A steady-state, heat flux ratio technique was developed during this study. For certain types of flows it offers some unusual advantages, the primary one being a measurement of temperature in a flowing, high temperature gas, which is independent of probe emissivity and Reynolds number so long as the boundary layer is laminar. The general approach may be easily extended to certain other geometries, such as a cylinder, and to other high temperature flows. The maximum temperature in the reacting region was measured with a pulsed thermocouple. The result was in reasonable agreement with the other measurements of temperature at this location.

Experimental studies were conducted on the distribution of particles entrained in the hydrogen jet. Visual observations and high speed photography were used to study the flame with burning particles. A new technique using neutron activation analysis was developed in this study for measuring the particle mass-flux distribution and the particle density distribution in the flame. This technique avoids the difficulties associated with burned or partially burned particles.

The results of the particle measurements showed that the particle

mass-flux distribution was not significantly affected by the total par-
ticle flux rate. The particle mass flux was observed to decrease along
the centerline between h/d = 22 and h/d = 72. At the higher position the
particles were distributed over a much larger area. The velocity profile
of the gases in the primary region of particle flow was practically flat.
Consequently, the particle velocity profile should be flat. The velocity
difference of the gases and particles may be large which would reduce
the values of the particle densities presented.

The following recommendations are made regarding further research
on turbulent mixing of reactive jets with entrained solid combustibles:

1. The theoretical treatment of concentric, reacting jets sug-
gested in this study should be studied further. Based on the experi-
mental data presented here more work is needed on turbulent, reacting
flows with the concentric jet geometry. Perhaps numerical solutions
should be obtained and tabulated for a range of values of n and compari-
sons made with existing data. The purpose of the work should be to
develop a more accurate and less tedious technique of correlating and
predicting turbulent flows.

2. The steady-state heat flux ratio technique should be further
investigated. This should be carried out in precisely controlled flows
with a spherical device at first and then with other shapes which appear
potentially useful. A thorough and accurate study could result in a
device which would be useful for many flow situations.

3. Efforts to obtain reaction kinetics data on the formation of
liquid Al_2O_3, particularly with varying oxygen environments, should be
made. With data of this type the combustion model might be altered to

include finite rate kinetics to some degree.

    4. The possibility of using the neutron activation analysis technique to determine gas velocity distributions using small tracer particles should be evaluated.

APPENDIX A

DYNAMIC PRESSURE DATA

The following tables give the dynamic pressure data obtained
with the water-cooled, stagnation probe. The ΔP data is the difference
between the local stagnation pressure and the chamber wall static pres-
sure.

Table 3. Dynamic Pressure Data

ΔP Data, Air Only, Without Duct Extension
and Screen

Height Above Nozzle Exit (inches)	ΔP, inches of H_2O radial position, inches								
	4	3	2	1	0	1	2	3	4*
0.0	0.003	0.262	0.247	0.231	**	0.225	0.237	0.233	0.193
2.75	0.043	0.233	0.242	0.225	0.160	0.225	0.245	0.211	0.115
5.75	0.078	0.217	0.242	0.212	0.180	0.226	0.234	0.166	0.097
8.75	0.091	0.204	0.235	0.199	0.189	0.226	0.218	0.134	0.083
11.75	0.101	0.202	0.225	0.194	0.196	0.218	0.189	0.101	0.083

*Tracking mechanism bottomed causing deflection of probe.

**Nozzle exit plane.

Table 4. Dynamic Pressure Data

ΔP Data, Air Only, Without Duct Extension
and Screen

Height Above H$_2$ Nozzle (inches)	ΔP, inches of H$_2$O radial position, inches									
	3.5	2.5	1.5	0.5	0	0.5	1.0	1.5	2.5	3.5
0.75	0.053	0.213	0.215	0.205	--**	0.125	0.205	0.214	0.213	0.210
2.75	0.060	0.214	0.202	0.200	0.196	0.165	0.198	0.210	0.209	0.205
5.75	0.065	0.211	0.205	0.202	0.194	0.183	0.197	0.210	0.212	0.204
8.75	0.078	0.202	0.203	0.199	--*	0.193	--*	0.209	0.210	0.205
11.75	0.092	0.194	0.201	0.200	--*	0.197	--*	0.207	0.210	0.204

*Measurements not made in these locations to conserve fuel and since this was a recheck of the flow with the modification indicated.

**Nozzle exit plane.

Table 5. Centerline Dynamic Pressure Data with H_2 Combustion

H_2 Injection Velocity ft/sec	ΔP, inches of H_2O axial position, inches														
	0.625	0.688	0.750	0.813	0.875	1.000	1.125	1.250	1.375	1.50	1.625	1.750	1.875	2.000	2.125
250	--*	0.680	0.630	0.560	0.490	0.370	0.300	0.350	0.230	0.210	0.200	--*	--*	--*	--*
326	--*	--*	1.046	0.900	0.780	0.550	0.450	0.380	0.320	0.290	0.270	--*	--*	--*	--*
406	1.830	1.660	1.460	1.220	1.030	0.760	0.590	0.498	0.405	0.348	0.303	0.263	0.236	0.211	0.193
550	--*	--*	2.320	2.000	1.550	1.020	0.830	0.600	0.530	0.480	0.400	0.360	0.300	0.300	0.280

*Measurements were not made at these positions to conserve fuel and avoid test interruption to change fuel cylinders.

APPENDIX B

CONCENTRATION DATA OF 1cc SAMPLES

Table 6. Centerline-Composition of 1cc Samples

Height Above H$_2$ Nozzle		H$_2$		N$_2$		O$_2$		Mass Fraction Ratio	$\bar{\beta}$
h/d	z, inches	lb x 10^7	cc	lb x 10^7	cc	lb x 10^7	cc	C_{N_2}/C_{H_2}	
0	0	1.839	1.0	0	0	0	0	0	0
22	2.75	1.442	0.786	4.790	0.187	0	0	3.3218	0.7926
40	5.0	1.062	0.579	9.770	0.382	0	0	9.1996	0.8988
56	7.0	0.815	0.444	12.980	0.506	0	0	15.9264	0.9285
72	9.0	0.602	0.328	16.710	0.654	0	0	27.7575	0.9467

Table 7. Composition of lcc Samples h/d = 22

r/r_0	Hydrogen		Nitrogen		Oxygen		Mass Fraction Ratio C_{N_2}/C_{H_2}	C_{N_2}/C_{O_2}
	wt. x 10^7 (lb)	cc	wt. x 10^7 (lb)	cc	wt. x 10^7 (lb)	cc	mass ratio	
48	0	--	20.17	0.788	6.20	0.212	--	3.253
16	0	--	19.90	0.778	6.06	0.207	--	3.284
8	0	--	19.81	0.774	5.86	0.200	--	3.381
6	0.044	0.024	20.76	0.811	3.55	0.121	471.82	5.848
4	0.872	0.475	13.47	0.526	0	--	15.45	--
2	1.301	0.708	6.96	0.272	0	--	5.350	--
0	1.442	0.785	4.79	0.187	0	--	3.322	--
2	1.360	0.740	5.54	0.216	0	--	4.074	--
4	1.133	0.616	8.69	0.339	0	--	7.670	--
6	0.310	0.168	16.70	0.654	1.28	0.044	53.87	13.05
8	trace	--	20.90	0.816	5.11	0.174	--	4.090
16	0	--	21.40	0.817	5.77	0.197	--	3.709
48	0	--	20.17	0.788	6.20	0.212	--	3.253

APPENDIX C

HEAT TRANSFER CORRELATION

The experimental heat transfer correlation of Cutting, et al.
(60) was used to calculate a heat-transfer coefficient to be used with
the pulsed thermocouple probe data. This correlation was determined
from measurements on small wire, heat transfer gauges with flowing,
dissociated combustion gases of $H_2 - O_2$ and $C_2H_2 - O_2$. The following
expression was used

$$\frac{Q}{l} = 2.27 \; Pr^{-0.6} \sqrt{\rho u \mu r} \; (\Delta h) \qquad (C-1)$$

where

Pr = Prandtl number of the mixture

ρ = density, lbm/ft^3

u = gas velocity, ft/sec

μ = viscosity, lbm/ft-sec

r = cylinder radius, ft

Δh = difference between stagnation enthalpy and enthalpy

at the wall, Btu/lbm

In order to obtain gas mixture properties data over a range of
temperatures a chemical equilibrium computer program (IBM 7094) was
used to calculate adiabatic flame temperatures and equilibrium concen-
trations for a range of mixture ratios of hydrogen and air. The results
of these computations are given in Table 8, page 168. The thermal

conductivity and viscosity of the gas mixture were calculated using the mixture rules as given by Mason and Saxena (61). The results of these computations in terms of a heat-transfer coefficient based on temperature difference are listed in Table 8, page 168.

Table 8. Chemical Equilibrium Composition

Hydrogen - Air Combustion

Mixture Ratio	25	30	34.186	38	40	45
Temperature, °F	2240	3140	4040	3500	3140	2240

Mole Fraction:						
H_2O	0.2620	0.2787	0.2634	0.2652	0.2537	0.2334
H_2	0.1025	0.0444	0.0221	0.0028	0.0006	---
H	---	0.0003	0.0037	0.0003	---	---
OH	---	0.0001	0.0082	0.0034	0.0015	0.0001
O_2	---	---	0.0052	0.0115	0.0181	0.0340
O	---	---	0.0011	0.0003	0.0001	---
NO	---	---	0.0035	0.0029	0.0022	0.0005
N_2	0.6354	0.6763	0.6928	0.7135	0.7201	0.7320
$h, \dfrac{Btu}{ft^2\text{-sec-}°R}$	0.03100	0.03169	0.03215	0.03094	0.03005	0.02729

APPENDIX D

NEUTRON ACTIVATION ANALYSIS

Neutron activation analysis techniques apparently have not been used previously in metal combustion studies. The use of a boron nitride collector strip was required due to the severe conditions existing in the flame with metal combustion. This material has a high cross section for thermal neutrons and in effect shields a sample being bombarded by neutrons from one direction. Also, gamma heating becomes a significant factor and the sensitivity of the technique is affected. These facts required modifications to be made in the usual neutron activation technique in order to apply the method to the particle samples. The following is a brief discussion of the general method and manner in which it was applied in this investigation. A detailed description of the technique and considerable information on its applicability to various problems are available in the literature.

This technique is a widely accepted method used for identification of unknown materials and for determination of element concentration. Detailed information on the general technique is available in the literature (62, 63). It has become known as one of the most sensitive techniques for either qualitative or quantitative elemental analysis. The application of this method can be used to identify some 70 of the naturally occurring elements. Most of the elements sensitive to neutron activation can be measured in quantities of less than a

microgram and some in quantities as low as 10^{-11} gram.

In neutron activation analysis, a sample is irradiated by exposure to a neutron flux. The irradiation causes some atoms to disintegrate with an accompanying emission of gamma rays, which are high-energy electromagnetic radiations. The emission of the gamma rays are counted and their gamma ray energies measured. Instrumentation for accomplishing this includes multichannel analyzers, liquid scintillation spectrometer system and special gamma ray detectors for ultra-high resolution spectroscopy. The gamma spectra obtained with this instrumentation can be used to identify elements which exhibit well known peaks at specific energy levels and by direct comparison with gamma spectra data of prepared standard samples produce data on the concentration of the element.

The neutron activation analyses performed in this study involved the measurement of the quantity of aluminum deposited on one side of a pyrolytic boron nitride collector strip. Aluminum is one of the elements which is readily activated with thermal neutrons, but the collector strip complicated the measurements to a degree since boron has an extremely high cross section for thermal neutrons. In effect the neutron flux was blocked from one side by the boron nitride strip. This required the preparation of standard samples on boron nitride strips so that the neutron flux for the test samples and the standard samples would be the same. This also required that all of the aluminum sample remain on the boron nitride strip during the irradiation or an extremely high aluminum concentration measurement would result. This is due to the higher neutron flux which would irradiate any of the aluminum sample not adhering to the boron nitride strip resulting in the production of many more

radioactive atoms. This caused no serious handicap in these measure-
ments, however, since the error produced is very large and easily
recognized.

The irradiating source used in these tests was the Georgia Tech
Research Reactor. It is a heterogeneous, heavy water cooled and moder-
ated reactor designed to produce 10^{14} n/cm^2-sec at a power level of 5
megawatts. The pneumatic tube system with a polyethylene "rabbit" was
used to transport the samples into and out of the reactor. The neutron
flux was 10^{13} n/cm^2-sec at the pneumatic tube section and with the boron
nitride strip required a limitation on the exposure time due to gamma
heating. A one minute time (clocktime) was selected with provision for
emergency shut-down at a total time of three minutes. This occurred
once during these tests as a result of a malfunction in the pneumatic
system causing the "rabbit" to remain in the reactor for three minutes.

The irradiation of the aluminum samples produce nuclear reactions
of a number of the aluminum atoms present resulting in the formation of
Al^{28} which has a half-life of 2.30 minutes. These reactions do not
depend on the presence of free aluminum. The activation occurs in both
the oxide form and in free aluminum. The product, Al^{28}, exhibits a peak
in the gamma spectrum at a relatively high energy level which is readily
distinguishable from other isotopes. The area under this curve when
corrected for the counting time and "cooling" time can be compared
with standard sample data to yield the quantity of aluminum present in
the sample. This measured quantity does not distinguish between alu-
minum in the oxide form and free aluminum.

The gamma spectrum data for a blank boron nitride strip and

four standard samples consisting of 10, 20, 50, and 200 micrograms of
aluminum on boron nitride strips are given in Table 9 of this appendix.
The data are given in counts per unit time for each channel of the analy-
zer for the Al^{28} peak of the gamma spectrum. The time of irradiation is
"clocktime" and as mentioned earlier, was set at one minute. The one
exception was the 20 microgram standard sample which was exposed for 70
seconds. The data was corrected to one minute before being used in the
calculations.

The standard samples were prepared by drying a carefully deter-
mined quantity of liquid containing a known amount of aluminum on one
side of a boron nitride strip. The solution was placed on the boron
nitride and dried by means of an infrared lamp before the sample was
moved. The samples were placed in a plastic container and inserted into
the reactor by means of a pneumatic tube, irradiated for one minute,
and removed. All samples were allowed to cool for 2.5 minutes before
counting.

The Live Counting Time is given in minutes in Table 9. It is a
number which is used to correct the peak area to account for the counting
time associated with this instrumentation. The value of the integral is
divided by this number to obtain the actual peak area for the sample.
The listing of counts per unit time for each channel, or energy level,
is by rows for each sample with increasing energy level, or channel num-
ber, from left to right. The vacancy in the second row for each sample
is a result of the technique used to print out the data and holds no
particular significance. The value of the integral is over the first
22 channels listed. The remaining channels permit the background noise

to be subtracted from the integral value in the calculation.

The blank boron nitride strip data show that less than a microgram of aluminum was present in the bare collector strip. For the accuracy required in these measurements this value was satisfactory. The "time out" of the reactor before counting is given with each sample. This value was 2.5 minutes for practically all cases. In the few instances in which this cooling time was greater, the data was corrected to 2.5 minutes before being used in the calculations.

Table 9. Al[28] Peak, Gamma Spectrum Standard Sample Data

(counts per unit time for each channel; integration over 22 channels; 2.5 minutes out)

Live Counting Time (minutes)	Counts Per Unit Time										Integral
	10 μ gm Al 1 minute clock time										
1.0	756	1193	1522	2028	2160	2260	1864	1594	1153	794	
	479	326	206	115	77	39	26		10	11	17644
	9	10	10	8	8	11	19	14	16	21	
	20 μ gm Al 70 sec clock time										
1.0	1845	2924	4004	5148	5621	5636	4939	4077	2976	1993	
	1295	829	485	290	185	94	60		28	19	44967
	24	25	25	14	29	28	34	42	37	39	
	50 μ gm Al 1 minute clock time										
0.70	4249	6145	7692	8634	8600	7801	6175	4578	3087		
	1983	1220	729	460	289	151	103		53	53	68101
	34	38	33	29	20	42	32	25	32	31	
	200 μ gm Al 1 minute clock time										
0.39	5653	8649	12277	15487	18020	18124	16429	13242	9826	6892	
	4354	2781	1730	1130	731	413	322		213	190	144167
	187	150	160	161	158	152	135	146	146	152	
	Blank BN Strip 1 minute clock time										
0.99	36	45	47	51	91	121	150	196	172	178	
	125	103	84	65	34	30	17		9	9	1706
	10	3	4	6	2	4	5	4	5	11	

Table 10. Gamma Spectrum Test Data

Counts per Unit Time for Each Channel; Integration over 22 Channels

Live Counting Time (minutes)	Counts Per Unit Time										Integral
	Sample No. 1A	2.5 minutes out									
0.92	513	822	1253	1664	1953	2031	1939	1539	1226	866	16063
	567	336	224	132	81	45	30		13	9	
	Sample No. 1B	2.5 minutes out									
0.89	221	357	547	691	835	884	827	690	507	359	6911
	224	138	96	66	45	25	9		6	11	
	1	4	4	4	6	7	6	10	9	13	
	Sample No. 1C	2.5 minutes out									
0.91	598	1045	1553	2041	2311	2581	2428	2066	1608	1116	20145
	750	461	310	162	111	51	23		7	13	
	11	8	5	3	5	11	4	7	7	15	
	Sample No. 1D	3.5 minutes out									
0.90	626	1039	1518	2009	2581	2659	2591	2220	1757	1200	21208
	812	531	326	174	113	61	40		13	7	
	7	11	3	3	4	4	6	12	14	22	

Table 10. Gamma Spectrum Test Data (Continued)

Counts per Unit Time for Each Channel; Integration over 22 Channels

Live Counting Time (minutes)	Counts Per Unit Time										Integral

Sample No. 1E   2.5 minutes out

0.83	1188	1914	2982	4100	4837	5057	4866	4147	3198	2230	
	1522	976	607	364	219	102	67		24	23	40015
	15	15	19	8	9	12	14				

Sample No. 1F   2.5 minutes out

0.86	1002	1621	2645	3406	4103	4424	4126	3433	2606	1854	
	1292	797	428	295	167	91	56		23	23	33785
	18	11	11								

Sample No. 1G   2.5 minutes out

0.78	1626	2709	3953	5506	6456	7130	6522	5765	4393	3087	
	2087	1295	800	456	288	167	75		56	31	54670
	27	18	12	16	19	18	16				

Sample No. 1H   2.5 minutes out

0.77	1472	2558	3835	5125	6171	6842	6232	5407	4201	3011	
	1938	1273	783	484	262	153	92		42	30	52046
	24	22	23	19	14	18	22	16	23	22	

Sample No. 1I   2.5 minutes out

0.82	1296	2138	3328	4367	5253	5540	5443	4496	3394	2517	
	1658	1037	646	380	216	116	58		33	19	43755
	22	18	13	14	12	13	17	20			

Table 10. Gamma Spectrum Test Data (Continued)

Counts per Unit Time for Each Channel; Integration over 22 Channels

Live Counting Time (minutes)	Counts Per Unit Time										Integral

Sample No. 1J   2.5 minutes out

	686	1058	1684	2258	2786	2990	2866	2356	1887	1348	
0.90	869	500	363	192	116	61	31		15	11	23024
	7	5	7								

Sample No. 1K   2.5 minutes out

	387	608	899	1167	1466	1624	1572	1330	1027	717	
0.94	489	346	206	104	58	45	15		10	11	12657
	4	2	3	3	6	8					

Sample No. 2A   2.5 minutes out

	1332	2130	3269	4358	5292	5801	5468	4648	3640	2642	
0.81	1752	1082	664	383	234	126	75		31	13	44765
	15	22	8	13							

Sample No. 2B   2.5 minutes out

	828	1352	2023	2717	3334	3559	3478	2923	2310	1591	
0.87	1072	662	453	256	146	79	37		12	11	27900
	8	7	8	10	7	12	11				

Sample No. 2C   2.5 minutes out

	1174	2012	2994	4080	5086	5561	5252	4481	3611	2515	
0.82	1710	1107	690	423	227	142	90		36	18	42921
	18										

Table 10. Gamma Spectrum Test Data (Continued)

Counts per Unit Time for Each Channel; Integration over 22 Channels

Live Counting Time (minutes)	Counts Per Unit Time										Integral

Sample No. 2D   2.5 minutes out

	1363	2255	3328	4673	5647	6296	6247	5391	4053	2952	
0.79	1943	1287	728	434	253	159	95		24	23	48982
	28	13	14								

Sample No. 2E   2.5 minutes out

	3800	6065	9074	12622	15574	16948	16714	14902	11646	8390	
0.43	5788	3746	2283	1425	906	554	383		190	143	136807
	147	148	135	117	138	114	128	124	94		

Sample No. 2F   2.5 minutes out

	1781	3092	4739	6536	8210	9264	8948	7717	6157	4264	
0.71	3004	1956	1162	740	396	248	148		67	39	71132
	34	35	20	32	27						

Sample No. 2G   2.5 minutes out

	489	839	1272	1749	2213	2338	2349	2172	1638	1277	
0.91	825	535	332	166	102	72	29		9	12	19117
	4	11	4	9	3	3	7	7	9	11	

Sample No. 3A   3 minutes out

	311	587	884	1157	1421	1581	1591	1383	1066	809	
0.91	568	342	211	134	79	53	25		12	6	12732

Table 10. Gamma Spectrum Test Data (Continued)

Counts per Unit Time for Each Channel; Integration over 22 Channels

Live Counting Time (minutes)	Counts Per Unit Time										Integral

Sample No. 3B   2.5 minutes out

0.96	208	279	463	692	754	846	840	735	587	447	
	298	202	126	98	59	42	24		16	16	7129
	6	9	6	17	12	12	27	20			

Sample No. 3C   2.5 minutes out

0.89	553	914	1315	1925	2501	2697	2643	2368	1825	1318	
	902	588	377	217	132	77	55		21	7	21261
	9	11									

Sample No. 3D   2.5 minutes out

0.76	1379	2248	3547	4918	6266	6862	6908	6044	4748	3550	
	2398	1639	949	612	329	194	99		43	32	54877
	32	22	28								

Sample No. 3E   2.5 minutes out

0.40	4031	6433	9646	13498	16870	18420	18499	16274	12968	9405	
	6556	4290	2712	1652	1055	641	448		250	213	150213
	178	196	179	171							

Sample No. 3F   5 minutes out

0.33	4086	6710	10033	14077	17474	19581	19404	17308	14197	10610	
	7065	4652	2967	1856	1152	724	516		336	246	159822
	227	201	214	235	214	189	164	187	161	201	

Table 10. Gamma Spectrum Test Data (Continued)

Counts per Unit Time for Each Channel; Integration over 22 Channels

Live Counting Time (minutes)	Counts Per Unit Time										Integral
	Sample No. 3G			2.5 minutes out							
	2080	3446	5736	8568	11727	14013	15079	14295	12375	9862	
0.51	6846	4700	2961	1818	1129	731	451		157	141	119964
	Sample No. 3H			2.5 minutes out							
	1758	2854	4803	7114	9921	11720	12585	11882	10160	7939	
0.59	5806	3812	2373	1546	917	534	330		141	95	99378
	74	73	61								
	Sample No. 4A			2.5 minutes out							
	917	1539	2534	3744	5192	6261	6479	6284	5257	4244	
0.78	2929	1994	1220	778	443	269	153		61	36	51953
	17	21	25								
	Sample No. 4B			2.5 minutes out							
	1350	2335	3944	5916	8096	9983	10795	10216	8883	6972	
0.60	5027	3399	2215	1359	823	489	264		122	61	84887
	50	55	45								
	Sample No. 4C			2.5 minutes out							
	2001	3386	5612	8169	11146	13741	14789	14215	12331	9782	
0.52	6934	4892	3109	1932	1146	704	447		188	128	118407
	95	96	98	93	88	78	66	80	83		

Table 10. Gamma Spectrum Test Data (Continued)

Counts per Unit Time for Each Channel; Integration over 22 Channels

Live Counting Time (minutes)	Counts Per Unit Time										Integral
				Sample No. 4D		2.5 minutes out					
0.14	5999 9058 636	8691 6107 627	12160 4222 612	16179 2750 630	19715 1950 579	21930 1403 571	22253 1011 564	20006 514	16538 769	12443 702	196221
				Sample No. 4E		8 minutes out					
0.31	2666 11442 314	3974 7928 293	6380 5256 246	9919 3521	13819 2265	17517 1453	19806 899	20259	18294 452	15081 375	167124
				Sample No. 4F		6 minutes out					
0.35	1904 11976 246	2971 8876 216	4801 5927 199	7578 3882 179	11074 2529 182	14700 1595	17234 1018	18751	17657 413	15334 324	153408
				Sample No. 4G		2.5 minutes out					
0.65	772 8402 107	1109 6537 72	1832 4589 51	3060 3014 44	5091 1962	7269 1168	9323 737	10784	10986 263	10217 159	89810
				Sample No. 4H		2.5 minutes out					
0.94	210 1718 22	254 1303 14	431 921	678 619	1081 386	1559 252	1931 133	2264	2246 47	2030 28	18688

REFERENCES

1. Tollmien, W., "Berechnung der turbulenten Ausbreitungsvorgange," Zeitschrift für angewandte Mathematik und Mechanik, 6, 468, (1926).

2. Abramovich, G. N., The Theory of Turbulent Jets, M.I.T. Press, Cambridge, Mass. (1963).

3. Pia, S. I., Fluid Dynamics of Jets, D. Van Nostrand, New York (1954).

4. Forstall, W., Jr., and Shapiro, A. H., "Momentum and Mass Transfer in Coaxial Jets," Journal of Applied Mechanics, 17, 399 (1950).

5. Kuethe, A. M., "Investigations of the Turbulent Mixing Regions Formed by Jets," Journal of Applied Mechanics, 2, A87. (1935).

6. Squire, H. B., and Trouncer, J., Round Jets in a General Stream, Aeronautical Research Committee R. and M. No. 1974 (1944).

7. Hinze, J. O., Turbulence, McGraw-Hill, New York (1959).

8. Pai, S. I., "Two-Dimensional Jet Mixing of a Compressible Fluid," Journal of Aerospace Science, 16, 463 (1949).

9. Pai, S. I., "Axially Symmetric Jet Mixing of a Compressible Fluid," Quarterly Applied Mathematics, 10, 141 (1952).

10. Schlichting, H., Boundary Layer Theory, 4th edition, McGraw-Hill, New York (1962).

11. Hawthorne, W. R., Weddell, D. S., and Hottell, H. C., "Mixing and Combustion in Turbulent Gas Jets," Third Symposium on Combustion, Flame and Explosive Phenomena, 266 (1948).

12. Alpinieri, L. J., An Experimental Investigation of the Turbulent Mixing on Non-Homogeneous Coaxial Jets, PIBAL Report No. 789, Polytechnic Institute of Brooklyn, August, 1963.

13. Ferri, A., Axially Symmetric Heterogeneous Mixing, PIBAL Report No. 787, Polytechnic Institute of Brooklyn, September, 1963.

14. Libby, P. A., "Theoretical Analysis of Turbulent Mixing of Reactive Gases with Application to Supersonic Combustion of Hydrogen," American Rocket Society Journal, 32, 388 (1962).

15. Masters, J. I., "Some Applications in Physics of the P Function," *Journal of Chemical Physics*, 23, 1965-1974, October (1955).

16. Donaldson, C. and Gray, K. E., Theoretical and Experimental Investigation of the Compressible Free Mixing of Two Dissimilar Gases, American Institute of Aeronautics and Astronautics Paper No. 65-822, December, 1965.

17. Kleinstein, G., On the Mixing of Laminar and Turbulent Axially Symmetric, Compressible Flows, PIBAL Report No. 756, Polytechnic Institute of Brooklyn (1963).

18. Kleinstein, G., "Mixing in Turbulent Axially Symmetric Free Jets," *Journal of Spacecraft and Rockets*, 1, 403 (1964).

19. Zakkay, V., Krause, E. and Woo, S. D. L., Turbulent Transport Properties for Axisymmetric Heterogeneous Mixing, Report 63-103 Polytechnic Institute of Brooklyn, New York (1964).

20. Zakkay, V., Krause, E., The Radial Variation of the Eddy Viscosity in Compressible, Turbulent Jet Flows, New York University, NYU-AA-64-4 (1964).

21. Zakkay, V., and Krause, E., Mixing Problems with Chemical Reactions. Aeronautical Research Laboratories Report No. 63-109, Polytechnic Institute of Brooklyn, New York (1963).

22. Grey, J., Williams, P. M., and Fradkin, D. B., Mixing and Heat Transfer of an Argon Arcjet with a Coaxial Flow of Cold Helium, Aeronautical Engineering Laboratory Report No. 710, Princeton University, Princeton, New Jersey (1964).

23. Forde, J. M., An Experimental Investigation of the Mixing of Supersonic, Turbulent Streams of Non-Similar Fluids, Mechanical Engineering Research Laboratories Report No. 63-3, McGill University, Montreal, Canada (1963).

24. Chervinsky, A., and Y. Manneimer-Timnat, "A Study of Axisymmetrical Turbulent Jet Diffusion Flames, Combustion and Flame," *Journal of the Combustion Institute*, 13, No. 2, 157 (1969).

25. Rosenweig, R. E., "Measurement and Characterization of Turbulent Mixing," D. Sc. Theses, Massachusetts Institute of Technology, June, 1959.

26. Daily, J. W., "Rigid Particle Suspensions in Turbulent Shear Flow," Hydrodynamics Laboratory Report No. 67, Massachusetts Institute of Technology, April, 1964.

27. Daily, J. W., and Roberts, C. P. R., "Rigid Particle Suspensions in Turbulent Shear Flow," Hydrodynamic Laboratory Report No. 69, Massachusetts Institute of Technology, June, 1964.

28. Marble, F. E., Dynamics of a Gas Containing Small Solid Particles, Fifth AGARD Colloquium Pergamon Press, London, 175-215 (1963).

29. Soo, S. L., "Gas Dynamic Processes Involving Suspended Solids," American Institute of Chemical Engineers Journal, 7, No. 3, 384-391 (1961).

30. Rudinger, G., Dynamics of Gas-Particle Mixtures with Finite Particle Volume, AIAA Paper No. 65-9, 2nd Aerospace Sciences Meeting, New York (1965).

31. Yu, K., and Klein, M. M., "Diffusion of Small Particles in a Non-Uniform Atmosphere, The Physics of Fluids, 7, No. 5, 651 (1964).

32. Kriebel, A. R., "Analysis of Normal Shock Waves in Particle Laden Gas," Journal of Basic Engineering, Trans. of ASME, 655, December (1964)

33. Hoglund, R. F., "Recent Advances in Gas-Particle Nozzle Flows," ARS Journal, 622, May (1962).

34. Gilbert, M., Davis, L., and Altman, D., "Velocity Lag of Particles in Linearly Accelerated Combustion Gases," Jet Propulsion, 26, January (1955).

35. Sargent, W. H., and Anderson, R., An Experimental and Analytical Study of Coaxial Jet Mixing, Technical Report AFRPL-TR-67-71, Air Force Rocket Propulsion Laboratories, Air Force Flight Test Center, March, 1967.

36. Nusselt, W., "Der Verbronnungsvorgang in der Kohlenstaubfeuerung," Verein Deutscher Ingenieure, 68, 124 (1924).

37. Essenhigh, R. H., "Predicted Burning Time of Solid Particles in an Idealized Dust Flame," Journal of the Institute of Fuel, XXXIV, No. 245, 239-244, June, 1961.

38. Essenhigh, R. H., "Burning Times of Coal Particles in a P. F. Furnace," Process of the 2nd Conference on Pulverized Fuel, London, 1957, Paper 2, page B1, Institute of Fuel, London, 1958.

39. Orning, A. A., "Combustion of Pulverized Fuel-Mechanism and Rate of Combustion of Low-Density Fractions of Certain Bituminous Coals," Transactions of the ASME, 497-508, July, 1942.

40. Grosse, A. V. and Conway, J. B., "Combustion of Metals in Oxygen," Industrial and Engineering Chemistry, 50, 663-672 (1958).

41. Glassman, I., "Metal Combustion Processes," ARS Preprint 938-959, November, 1959.

42. Markstein, G. H., "Combustion of Metals," AIAA Journal, 1, No. 3, 550-562, March, 1963.

43. Bartlett, R. W., Ong, J. N., Jr., Fassel, W. M., Jr., and Papp, C. A., "Estimating Aluminum Particle Combustion Kinetics, Combustion and Flame," Journal of Combustion Institute, 7, 1963.

44. Coffin, K. P., and Brokaw, R. S., "A General System for Calculating Burning Rates of Particles and Drops and Comparison of Calculated Rates for Carbon, Boron, Magnesium, and ISOOCTANE," NACA TN 3929, February, 1957.

45. Friedman, R., and Macek, A., "Ignition and Combustion of Aluminum Particles in Hot Ambient Gases," Combustion and Flame, Journal of Combustion Institute, 6, 9, March, 1962.

46. Macek, A., "Fundamentals of Combustion of Single Aluminum and Beryllium Particles," Heterogeneous Combustion, Progress in Aeronautics and Astronautics, XV, AIAA, 1964.

47. Kuehl, D. K., "Ignition and Combustion of Aluminum and Beryllium," AIAA Journal, 3, No. 3, 2239-2247, December, 1965.

48. Courtney, W. G., "Condensation During Heterogeneous Combustion," Eleventh Symposium (International) on Combustion, 237-244 (1966).

49. Brzustowski, T. A., "Vapor Phase Diffusion Flames in the Combustion of Magnesium and Aluminum," Ph.D. Thesis, Princeton University, 1963.

50. Sibulkin, M., "Heat Transfer Near the Forward Stagnation Point of a Body of Revolution," Journal of Aerospace Science, 19, No. 8, August, 1952, 570-571.

51. Lees, L., "Laminar Heat Transfer Over Blunt-Nosed Bodies at Hypersonic Flight Speeds," Jet Propulsion, 259-269, April, 1956.

52. Eckert, E. R. G. and Drake, R. M., Jr., Heat and Mass Transfer 2nd Ed. McGraw-Hill Book Co., Inc., New York, 1959.

53. Wormser, A. F. and Pfuntner, R. A., "Pulse Thermocouple Measures at 5700°F, Space/Aeronautics, 116-118, July 1963.

54. Carlslw, H. S. and Jaeger, J. C., Conduction of Heat in Solids, Oxford University Press, 2nd Ed., 54-55 (1959).

55. Marble, F. E., and Adamson, T. C., Jr., "Ignition and Combustion in a Laminar Mixing Zone," Jet Propulsion, 24, 85-94, March, 1958.

56. Corrsin, S and Uberoi, M. S., "Further Experiment on the Flow and Heat Transfer in a Heated Turbulent Air Jet," NACA TR 998, 1950.

57. Williams, F. A., *Combustion Theory*, Addison-Wesley Publishing Co., 1965.

58. McBride, B. J., Heimel, S., Ehlers, J. G. and Gordon, S., "Thermo-dynamic Properties to $6000^{\circ}K$ for 210 Substances Involving the First 18 Elements," NASA SP-3001, 1962.

59. Hooke, R. and Jeeves, T. A., "Direct Search Solution of Numerical and Statistical Problems," *Journal of Association for Computer Machinery*, 8, 212-229.

60. Cutting, J. C., Fay, J. A., Hogan, W. T., Moffatt, C. W., "Heat Transfer in Dissociated Combustion Gases," AFOSR-TR-59-78, Office of Scientific Research, USAF, July, 1959.

61. Mason, E. A. and Saxena, S. C., "Approximate Formula for the Thermal Conductivity of Gas Mixtures," *The Physics of Fluids*, 1, no. 5, 1958.

62. Koch, R. C., *Activation Analysis Handbook*, Academic Press, New York, 1960.

63. Mopper, D., *Methods in Geochemistry*, Interscience Publishers, New York, 1960.

VITA

Mack Donald Bowen was born in LaGrange, Georgia on October 6, 1930. He graduated from LaGrange High School in 1950 and served in the United States Air Force until December, 1954. He entered the Georgia Institute of Technology in January, 1955, and completed his degree requirements in Mechanical Engineering in September, 1957. He continued his studies in graduate school while employed by the Engineering Experiment Station and received a Master of Science in Mechanical Engineering in June of 1959. He continued his employment with the Engineering Experiment Station until June of 1960 at which time he accepted a position in the aerospace industry. He returned to the Georgia Institute of Technology in September of 1964 to resume his graduate studies on a part-time basis while employed by the Research Center, Lockheed-Georgia Company. He accepted a position as a Special Lecturer in the School of Mechanical Engineering in January of 1968 and a position of Senior Research Engineer at the Engineering Experiment Station in July of 1968.

He is a member of Pi Tau Sigma and the Society of Sigma Xi.

Mr. Bowen is married to the former Betty Ruth Jones. They have three children, Susan, Kelby and Mark.